Study on high field side injection of X-mode for EBW conversion in QUEST

ハテム, オマ, アミン, モスタファ, エルセラフィ

https://doi.org/10.15017/2534468

出版情報：Kyushu University, 2019, 博士（理学）, 課程博士
バージョン：
権利関係：

Doctoral Thesis

Study on high field side injection of X-mode for EBW conversion in QUEST

ASEM, IGSES, Kyushu University

Hatem Elserafy

Acknowledgement

First and foremost, I would like to attribute this work to Prof. Kazuaki Hanada as he not only had an essential role in the completion of said work, but he also had the patience and resilience to teach and pass on his indispensable knowledge to myself as well as my colleagues. Prof. Hanada's instructions and innovative teaching techniques have never failed to inspire me. Conducting experiments alongside Prof. Hanada, watching him in action while listening to him giving me technical advice on how to deal with plasma physics has been a major highlight in my career. In addition, his support was not only limited to my doctoral studies but also to my career after graduation, to my mental and physical wellbeing, and to my life outside of the lab. Not to mention, he was very open to my pursuit of extracurricular activities alongside studying and he encouraged me to have a healthy balanced life. Not to mention, his hilarious sense of humor was very much enjoyed during parties and celebrations. Despite this man's name speaking for itself, I cannot help but acknowledge his greatness in this modest thesis.

To Prof Kiichi Hamamoto, I would like to thank you for the support that you have given me throughout the five years of masters and doctoral studies. The gratitude I have for the amount of knowledge you have taught me is far more than words can describe. You have provided me with different opportunities to engage with the scientific and the industrial fields and most of all, you have always respected and encouraged me. I am forever grateful to what you have given me.

I am particularly grateful to Dr. Takumi Onchi, Prof. Hiroshi Idei, Prof. Masayuki Ono, Prof. Makoto Hasegawa, Prof. Kazuo Nakamura, Dr. Nicola Bertelli, Dr. Ryuya Ikezoe, Dr. Kengoh Kuroda and Dr. Arsieny Kuzmin. Without their expertise in the field and their tremendous support, this work would not have been successful. I am honored to have shared the same facilities with such giants and for borrowing their time and wisdom ever so frequently.

Further gratitude is directed towards my colleagues, Dr. Ryota Yoneda, Mr. Shinichiro Kojima, Mr. Takahiro Murakami, Mr. Masaharu Fukuyama and Ms. Miu Yunoki. Their academic support as well as their shared memories outside the lab are unforgettable. Special thanks are due towards Dr. Yoneda and Mr. Kojima for their constant support outside of the lab to help me deal with my everyday problems and for being excellent life-coaches to me.

In addition, I would like to thank the administrative staff in general. Special thanks to Mrs. Kaori Yamaguchi for her bureaucratic support and to Mrs. Azusa Kawamura for bridging my language gap and helping me with my job hunting.

In addition, I would like to thank every member of QUEST team. It was an honor to share QUEST with you all and to collaborate with you.

Last but by no means least, to my family, I would like to gift them my doctoral thesis in hopes to make them feel proud. To my father, Omar Elserafy, my mother, Hanan Eissa, and my sister, Dina Elserafy, I am forever indebted to you for every single accomplishment I make in my life. My world is so much easier than it should be, just because I have my family as my backbone to protect me and help me move forward.

Abstract

Electron Bernstein Wave (EBW) is a candidate for overcoming the density limit for RF induced plasmas in the electron cyclotron range of frequency, although EBW, an electrostatic wave, can only be created inside of the plasma via mode conversion. Several mode conversion scenarios exist including Ordinary-Extraordinary-Bernstein (O-X-B) wave conversion from low field side (LFS), direct X-B conversion from LFS, and X-B conversion from high field side (HFS). LFS launch has been conducted in QUEST with low efficiency and inability to surpass the cutoff limit using 8.2 GHz RF injection. HFS injection of X-mode to EBW mode is expected to have higher conversion efficiency, so it was the target of this work.

In the Section 1, introduction and necessity of nuclear fusion development are described. It is clearly indicated that to satisfy both electric power production to progress mankind and mitigation of climate change, new technologies such as nuclear fusion are indispensable. Tokamak is the most promising way to realize a fusion power plant on the earth and several kinds of alternative ways are introduced. Spherical tokamak (ST) has a possibility to achieve cost-effective fusion power plant, but development of non-inductive way to produce plasma current that needs to make a plasma equilibrium in tokamak type of magnetic fusion devices is the most crucial issue. RF current drive has been developed for overcoming the issue and the remaining is to produce higher density plasma with only RF. After that, other techniques such as neutral beam injection and so on are available.

In the Section 2, basic physics for wave propagation and absorption in plasma are described. Several scenarios to excite electron Bernstein wave (EBW) are specifically introduced. The merit and demerit are compared and the reason why the X mode injection from high field side (HFS) should be selected is clarified in the view of theoretical basis consideration.

In the section 3, two important codes for quantitative estimation of wave absorption and driving plasma current are introduced. EFIT was used to analyze the magnetic surface in QUEST, then calculate the magnetic reconstruction as an input for GENRAY ray tracing code that can estimate wave absorption and driven current. According to GENRAY's simulations, inputting further density than $1.5\times10^{18}\mathrm{m}^{-3}$ would lead to ω_{pe} (plasma cut-off) layer development enough to bend the X-mode ray out of UHR's access. GENRAY also provided output that the injected ray has to be tilted above or below the mid-plane if EBWCD was of interest, such that above the mid-plane would create a counterclockwise Ip and below the mid-plane would create a clockwise Ip in the condition of present magnetic surface in QUEST. In conclusion, HFS injection of X-mode with an injection tilt angle is expected to drive EBWCD, therefore a tilt or a shift is to be considered in injection system design, which is to be discussed in the next section.

In the Section 4, the HFS injection system design is discussed. a waveguide-based RF transmission line from LFS to HFS for 8.2 GHz which is equipped in QUEST is proposed. This system has the advantage of working in any frequency range as well as not suffering any reflective losses from reflecting mirrors that were used in the other devices. The transmitted RF should be emitted by a simple open-ended waveguide. The dispersion and non-desired RF absorption were accounted for, showing no more than 7% losses in the plasma of 50eV electron temperature. To summarize, the HFS injection system could be designed, based on optimizing wave transmission and minimizing undesired RF absorption in the present specification of QUEST.

In the section 5, the experimental results are denoted. The experiment has been executed by using only toroidal magnetic field to simply investigate the EBW mode conversion. The electron temperature using Langmuir probe in the HFS case was at an average of 4 eV, while in the LFS case it was about 2 eV. Moreover, the brightness of the fast camera images in the case of HFS launch is significantly higher than those in LFS launch. An interferometer was used to measure line-averaged density and it finds that the position of UHR estimated by the measured density corresponds to the brightest position in the fast camera images. This clearly indicates that EBW could be excited in the plasma and deposited via collisional damping as predicted by GENRAY calculation. Higher density and temperature in HFS launch suggests having better mode

conversion efficiency than that in LFS launch. In fact, the leakage RF which monitors non-absorbed RF power was significantly small in HFS launch.

The experiments with poloidal field which provides a tokamak equilibrium were also executed to improve plasma current and investigate EBWCD. The results of the experiment showed that HFS plasma current peaked at 1.5 kA while in LFS it only peaked at 0.4 kA. In addition, the sideband at 8.1 GHz was measured and the signal is a proof of EBW's parametric decay instability (PDI) and the presence of lower hybrid wave which is excited during EBW mode conversion, although the frequency of 80 MHz is slightly lower than the expected value. These observations indicate that the HFS launch makes a much better conversion to EBW and it is expected in prediction of basic wave physics and GENRAY. While the LFS density peaked at $8\times10^{17}m^{-3}$. Another target was the excitation of EBWCD, which was tested by applying a poloidal field, and measuring the plasma current, then reversing the polarity of the poloidal field and checking how different the plasma current would be. However, plasma current did not show any signs of significant change, and therefore the excitation of EBWCD was not confirmed. The driven plasma current is assumed to be pressure-driven as QUEST has an experience of having pressure-driven current of up to 2kA. The lack of EBWCD can be attributed to the fact that there was no closed flux surface. Nonetheless, the highlight of this work was the density, where in the case of HFS, plasma density peaked at $1.4\times10^{18}m^{-3}$, almost twice that of the cutoff density, which corresponds to the density limit predicted by GENRAY as described above.

In conclusion, EBW excitation of X-mode from the HFS injection using waveguides is possible. To confirm EBW excitation from HFS using waveguides, EBW's PDI was detected. Not to mention, HFS injection has higher EBW conversion efficiency than that of the LFS. This was confirmed by comparing HFS injection to that of LFS injection, showing that HFS injection has brighter plasma (from camera image), higher plasma current, higher temperature, lower leakage and higher density, compared to LFS injection. Moreover, the primary target of this work, which is to drive plasma density higher than the cutoff limit, was achieved by HFS injection.

Contents

List of figures

1. Introduction

Cumulative greenhouse gas emissions are a direct contributor to the global rise in temperature [1]–[3]. The united nations agreed that there is an average rise of 2ºC in the global temperature [4]. A significant reduction in fossil fuel consumption is required to regulate the temperature rise. Less than half of the gas reserves, less than two thirds of oil reserves and only 20 percent of coal reserves is to be consumed to avoid surpassing the 2ºC rise in temperature, and this rate should be maintained until 2050 [5]. The aggressive consumption of fossil fuels is a strong indicator of the huge energy demand, as reported by U.S Energy Information Administration (EIA), which presents a difficulty to meet the conditions required for suppressing the average temperature rise. Fossil fuel consumption constitutes more than 50% of the global energy market, as reported by BP global in 2016 (see Fig. 1).

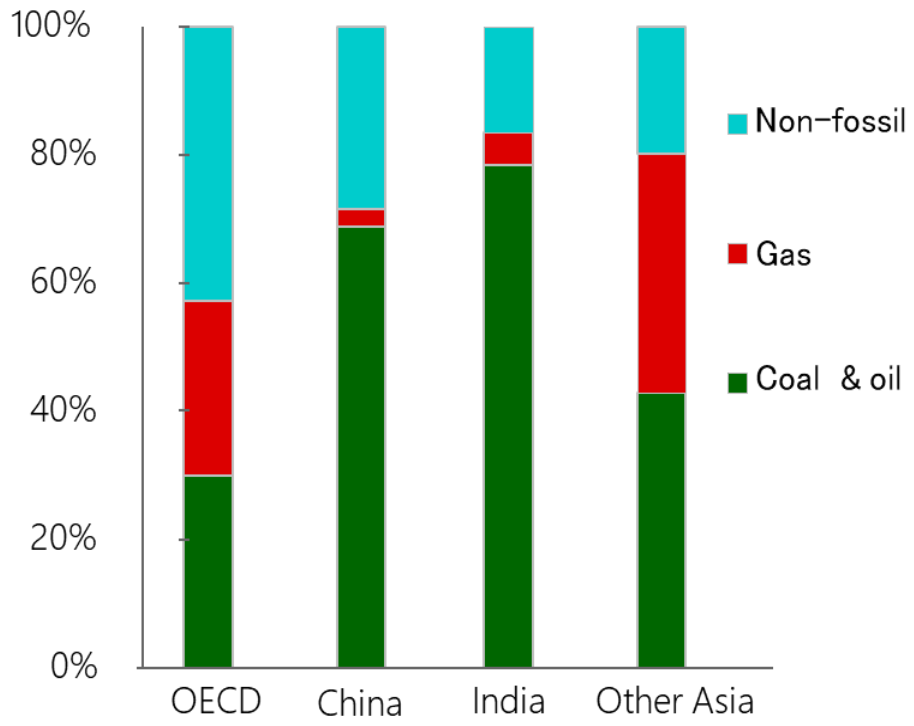

Fig. 1 Different fuel types consumed for certain geographic areas as reported by BP global 2016

Solar, wind, tidal, geothermal, and thermonuclear fusion constitute a clean and environmentally friendly renewable sources of energy that can be used as an alternative to fossil fuels. Combustibles, renewables, hydro and nuclear energy plants show their annual market in Fig. 2 as reported by BP global [6].

More than a century ago, nuclear physicists understood that nuclear reactions can be controlled to generate a significant amount of energy. To put things into perspective, annually, about 109,136 TWh of energy are estimated to be consumed worldwide (as of 2015), while the sun, fueled by nuclear reactions, generates about 1.06×10^{11} TWh per second, which is more than the entire energy consumption in the history of the planet. Aside from the capability of putting this much energy into military applications, resulting in hundreds of thousands of deaths from the Hiroshima and Nagasaki fission bombs, which progressed even further by the construction of Hydrogen fusion bombs that are potentially a thousand fold more powerful, the peaceful application of

harnessing this energy for improving the lifestyle of civilians is also in tremendous progress. Nuclear fission energy was controlled for the production of commercial energy in the mid-19th century. The progress within harnessing fission energy led to the idea that fission energy would be safe and available within the advancement of technology, however, that has not been the case

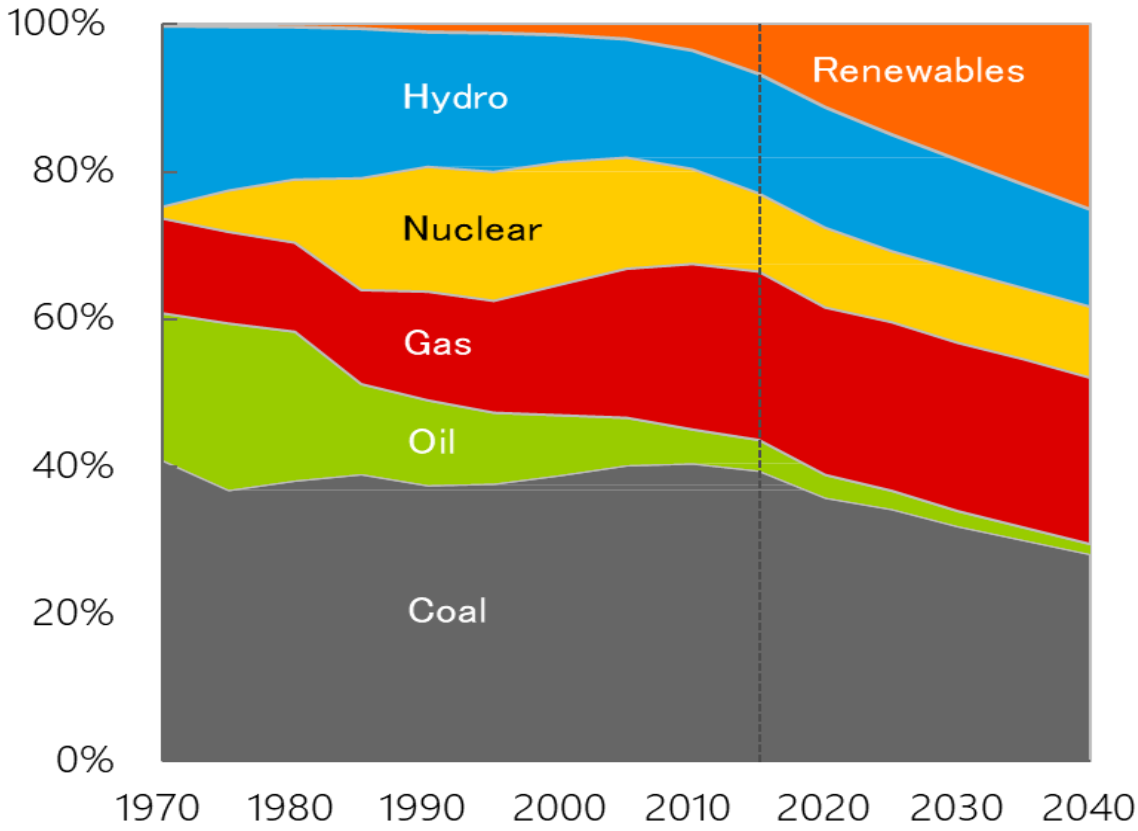

Fig. 2 Annual production of various types of energies over time, as reported by BP Global

as the fission production not only stagnated in developing its technology, but also languished in the past decade from 18% to about 14% in terms of total world energy consumption [6]. On the other hand, thermonuclear fusion energy yield has been widely known to be unparalleled since the 1950s [1], not to mention its virtually nonexistent carbon footprint [2].

Moreover, fusion technology gained a lot of credibility after revealing how operationally safe it is in terms of explosions and dealing with radioactive materials [3]. However, fusion energy has been researched for more than 60 years and still has several milestones to surpass before realizing commercialization, yet it is still thought of as a promising source of energy that is to be deployed [4], [7]. Aside from fusion skeptics claiming that integrating fusion energy in the grid is an absolute impossibility, the fact of the matter is that there are plenty of unsolved problems that are being tackled one at a time, but that is a strong indicator that there is no profound knowledge about how to properly build a reactor. However, it can be said with a high degree of confidence that fusion, if realized, will be expensive in comparison to its competitors. For that reason, plenty of innovative research is conducted with the motive to reduce the reactor cost by making the reactor design more compact, by changing the materials used to constructing it, or by changing the plasma heating methods. A detailed review about different reactor designs is to be presented

in section 1.2. Furthermore, different plasma heating technologies are to be explored in attempt to improve the results of the economic reactors. This work will focus on economically heating and driving plasma current in the case of compact reactors.

1.1 Fusion Theory

This section will discuss the basic theory of nuclear fusion and how the fusion equations can be put to use to create a nuclear reactor and generate power.

1.1.1 Thermonuclear fusion reaction

Thermonuclear fusion reaction, based on Einstein's famous E=mc¬2 equation, goes as follows:

$$^{1}D_2 + {}^{1}T_3 \rightarrow {}^{2}He_4 \ (3.5 \ MeV) + {}^{0}n_1 \ (14.1 \ MeV) \quad 1.1.1$$

$$D_2 + D_2 \rightarrow He_3 + n_1 + 3.27 \ MeV \quad 1.1.2$$

$$D_2 + He_3 \rightarrow He + H_1 + 18.3MeV \quad 1.1.3$$

where D (deuterium) and T (tritium) are Hydrogen isotopes, n is neutron. The primary difficulty with achieving this reaction is that to overcome the coulomb forces repelling the nuclei, a temperature in the order of 10^6 °C is required which can be considered as an external catalyzing factor to the reaction. It can be seen that several versions exist based on the Hydrogen isotope input, making D-He the most attractive as it has the largest energy yield. However, considering the cross-section between nuclei as a function in energy is essential since the catalyzing factor is difficult to achieve. The cross-section is defined as

$$\sigma = \frac{S(E)}{E} * \exp\left(-\frac{BG}{\sqrt{E}}\right) \quad 1.1.4$$

where σ is the cross-section, S is the astrophysical S-function, and BG is the Gamov constant. The Gamov constant is defined as

$$BG = \pi\alpha Z_1 Z_2 \sqrt{2mrc^2} \quad 1.1.5$$

where Z1 and Z2 are the atomic numbers of the two nuclei to be fused. The cross-section calculations, based on [7] are as shown in Fig. 3.Based on Fig. 3, despite D-He dominating in terms of energy yield, it can be seen that D-T has higher sigma as energy decreases, making its fusion condition achievable at comparatively lower temperature. Correspondingly, D-T fusion is to be the focus of this work, where the bioavailability and cost of both is to be considered.

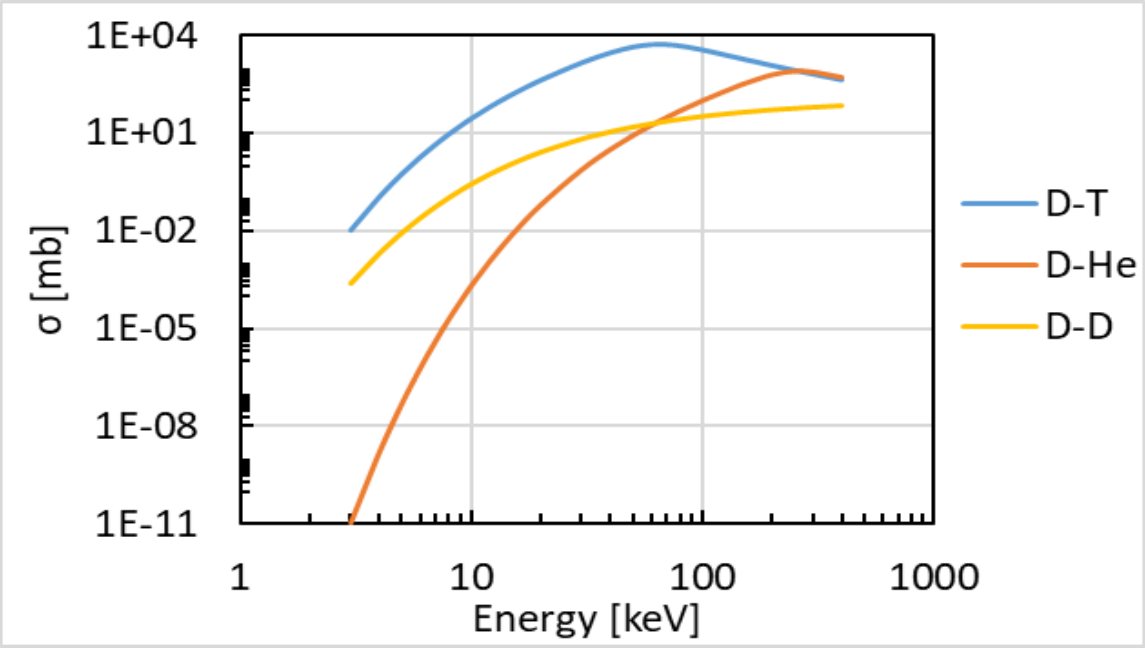

Fig. 3 Cross section as a function in energy for fusion reactions of different H isotopes

1.1.2 Thermonuclear fusion ignition

Thermonuclear fusion is particularly attractive in the field of renewable energies because once a certain condition is achieved (ignition), the plasma will reach a state where it can internally self-sustain its temperature against the energy losses. Ignition would in turn allow for the removal of the applied heating, significantly reducing the input power. This sustained condition is due to the emission of the He4 particle (alpha particle [8]) in the D-T reaction such that

$$P_H + P_\alpha = P_L \tag{1.1.6}$$

where P_H is the heating power, P_α is the power generated by the alpha particle, and P_L is the power loss. Achieving ignition condition depends on several factors including the size and structure of the reactor, plasma temperature, plasma density and the magnetic field strength. However, a reliable indicator of how well a particular reactor is performing is the Lawson criterion (also known as the triple product)

$$nT\tau \geq 3 \times 10^{21} keV \frac{s}{m^3} \tag{1.1.7}$$

where T is ion temperature in eV, τ is plasma confinement time, and n is ion density [9]. This critical criterion not only indicates the threshold for self-sustained fusion, but also indicates the possibility to trade off different parameters. This is particularly useful as each reactor has its unique structure and specifications mastering one or two of the triple-product parameters. Noteworthy is to say that not a single reactor was yet able to produce plasma with satisfying values to all three key parameters simultaneously.

1.2 Thermonuclear fusion reactors

Given that no solid material can endure the extreme particle and heat loads produced by high temperature and density of fusion plasmas, plasma confinement is a necessity. Fusion devices are majorly divided into Magnetic Confinement Fusion (MCF) plants and Inertial Confinement Fusion (ICF) plants. Examples of ICF devices are such as (laser-driven [10] or Z-pinch [11]). However, MCF devices have proven to have a higher Lawson criterion than ICF ones [12], [13] and therefore MCFs are the focus of this work. Furthermore, toroidal machines are to be focused on rather than open-field machines [14]. Not to mention, toroidal machines vary in shape and structure giving several standard reactor types like tokamaks [15], stellarators [16], [17], reversed field pinch [18], spheromaks [19] and others [20].

1.2.1 Tokamaks

Tokamak is a Russian term which translates to 'toroidal magnetic container'. Credit goes to Soviet physicists I. Y. Tamm and A. Sakharov (who were inspired by an original idea of O. Lavrentyev [21]) to create the Tokamak concept. Historically, ever since the T-3 tokamak belonging to Kurchatov Institute – Russia obtained a plasma temperature of 1 keV [22], tokamak research was the focus of many nuclear fusion research institutes [23]–[26]. Tokamaks-based D-T reactions were able to supply an output power of the order of MW [15], [27]. Furthermore, ITER, the world's largest nuclear fusion reactor that is to be the first to achieve output power 10 fold that of the input power, is in fact a tokamak [28].

Essentially, tokamaks contain the superposition of both toroidal and poloidal fields (TF and PF respectively). The toroidal flow of plasma (plasma current) creates a PF which contributes to the net PF profile. Applying TFs solely is incapable of confining plasmas as it has a gradient (the center of the tokamak being of strongest magnetic field B), which would cause ions and electrons to drift vertically in opposite directions due to the ∇B drift. This charge separation would create a vertical electric field, which would then interact with B causing the plasma to drift radially outwards towards the tokamak walls (this is known as the $E \times B$ drift. To counter this phenomenon, driving plasma current toroidally would a plasma PF that would nullify the effect of the $E \times B$ drift, and would in turn create spiraling magnetic lines. In addition, plasma in this situation would drift outwards with hoop force, which is why the installation of toroidal coils to create PFs is necessary. Conventionally, tokamaks have a solenoid located at its center, which is responsible to drive plasma current, referred to as the center solenoid (CS) or center stack. Another function that the CS serves is the initiation of plasma breakdown, which is referred to as inductive (Ohmic) breakdown. However, a limitation of primarily depending on CS for heating and plasma current drive is that its coil current cannot be changed indefinitely. Another limitation for Ohmic heating and current drive (Goldston, 1984) is that plasma particle friction decreases as the temperature increases. This limitation dictates the use of other heating methods, referred to as non-inductive heating methods (van Houtte, et al., 2004). The primary non-inductive heating methods in the market are: (a) Neutral Beam Injection (NBI), which is used to inject neutral particles that are immune to the magnetic field restrictions and hence can roam freely inside the plasma, colliding with the charged particles and then heating up plasma, and (b) Radio frequency

(RF) wave injection, which injects RF waves of high power that are to be absorbed by the plasma at certain resonance conditions, which would heat up the plasma.

1.2.2 Spherical tokamaks

The primary issues with conventional tokamaks is that they are unstable in high β as well as expensive, hence the introduction of spherical tokamaks. Spherical tokamaks (STs) are defined as tokamaks with low aspect ratio. Aspect ratio in this context is $A = R_0/a$, where R_0 and a are the major and minor radii of the tokamak respectively. A tokamak is considered spherical when $A < 1.5$, such that its cross-sectional view is D-shaped. STs are stable as they are of high β [29]. β is defined as the ratio between plasma pressure and magnetic pressure. Another fundamental advantage of STs is that high-β plasmas share similar characteristics to low-β plasmas but at significantly lower magnetic fields, hence reducing the overall cost of the reactor. In addition, the low aspect ratio gives little room for a CS, which would create Ohmic heating and current drive issues [30]. This pushes the incentive to heat high-β plasmas using purely non-inductive methods. Not to mention, if ST operation could be conducted CS-free, that would further improve its economic value. A list of all the famous tokamaks are listed and compared in [31].

1.2.4 QUEST spherical tokamak

QUEST (Q-shu University Experiment with Steady State Spherical Tokamak) is a medium-sized ST with a purpose of studying steady-state operation issues, plasma-wall interaction phenomena in steady state which is of critical importance for realizing a volume neutron source full scale fusion plant [32]–[34]. Another theme for QUEST is non-inductive heating and current drive [29], [35].

The device parameters are: major radius $R_0 = 0.68m$, minor radius $a = 0.40m$ and toroidal magnetic field of $B_T = 0.25T$ in steady state (and $0.5T$ for up to 1s at a radius of $R = 0.64m$). The radius of the outer surface of the CS and the radius of the inner surface of the wall are 0.22m and 1.4m respectively. Flat diverter plates that are tungsten-coated for high heat load endurance) are located at a vertical displacement of $Z = 1m$ (where the mid-plane is located at $Z = 0$m). QUEST has a total of 16 toroidal coils such that the spacing between pairs is 45°. QUEST has 11 PF coils and a pair as shown in Fig. 4. QUEST is equipped with RF sources of 2.45 GHz klystron of 50 kW, 8.2 GHz klystron of 55 kW and 28 GHz gyrotron of 250 kW.

For controlled 8.2 GHz launching in QUEST, a launching antenna is used (see Fig. 5). For launching polarization control, mixing two orthogonal electric field components with different phase is crucial. This orthogonal electric field mixing is done through a device called orthomode transducer. The previous Kyushu University tokamak (called TRIAM-1M) adopted its Lower Hybrid Current Drive (LHCD) system to QUEST. This system is to be used for Electron Bernstein Wave Heating / Current Drive (EBWH/CD) in QUEST at an operating frequency of 8.2 GHz (details are to be discussed in a later section). A number of rectangular waveguides (16 in total), called WR-137, were used for the power transmission of $200\ kW$ to the LHCD system. The attenuators and phase shifters found in the transmission line were used to control the output polarization state at the orthomode transducer. The orthomode transducer conceptual design part was illustrated in Fig. 5, where two field components with different intensity and phase at the rectangular waveguide input were mixed at the orthomode transducer, and were driven to the antenna given an arbitrary elliptical polarization state.

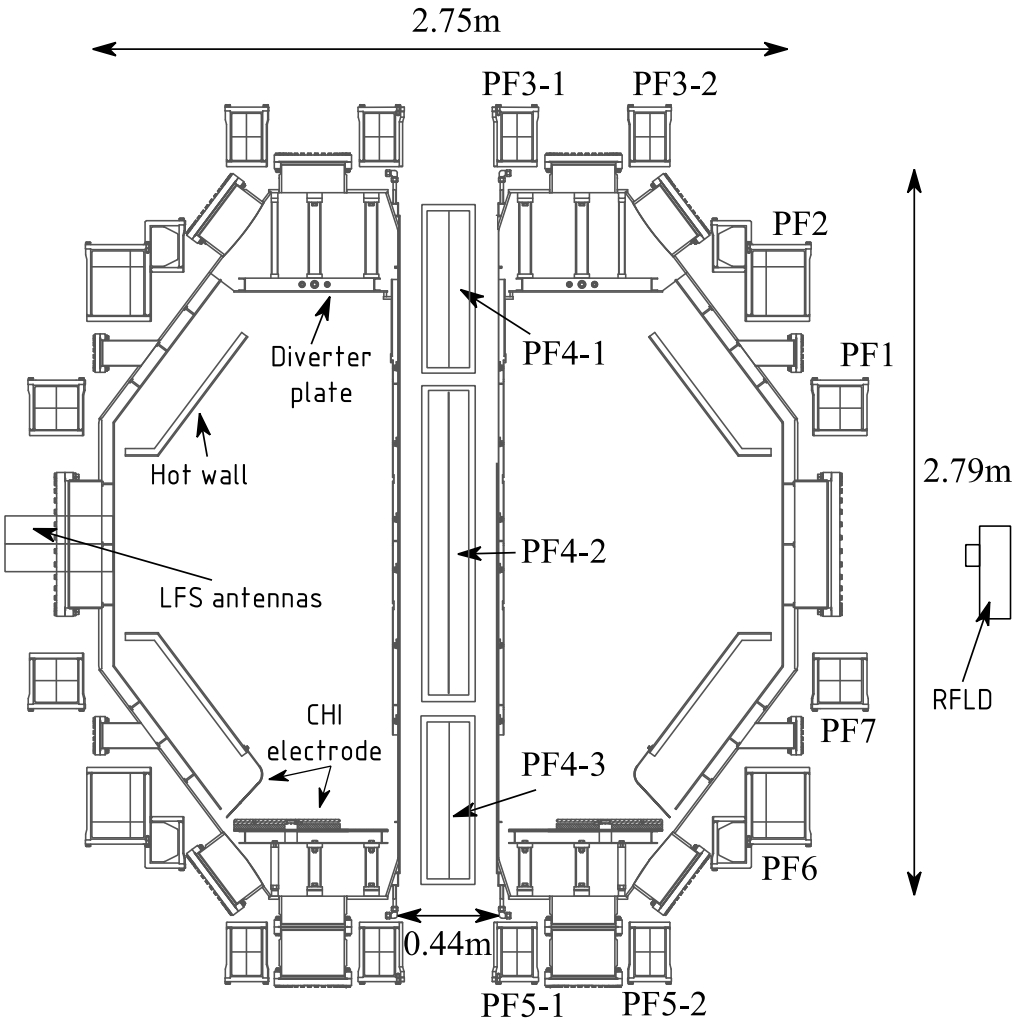

Fig. 4 QUEST's cross sectional view showing different poloidal field coils and other in-vessel components

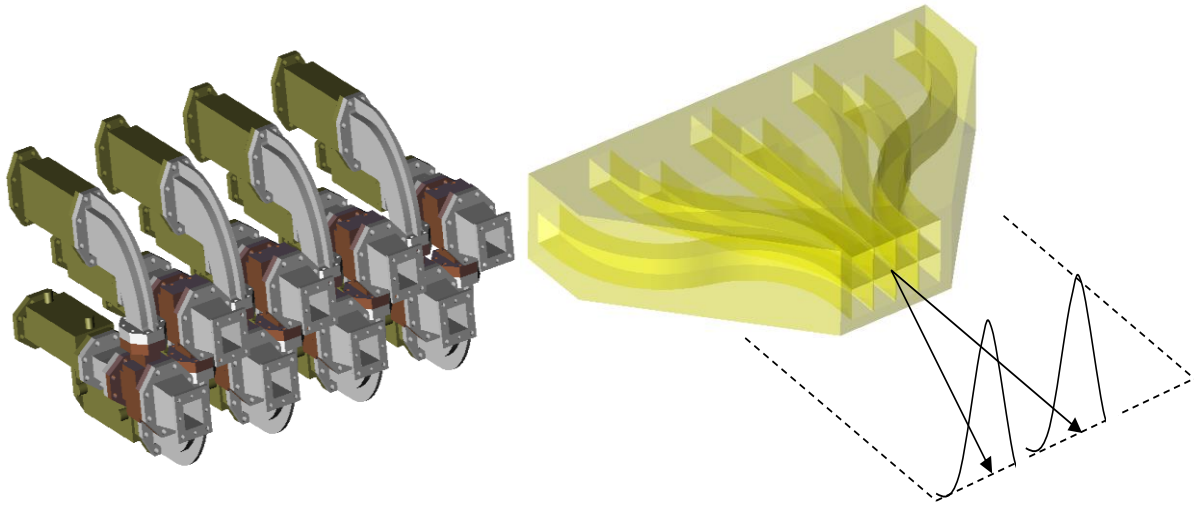

Fig. 5 Low field side phased array launcher of Klystron (8.2 GHz) [36]

1.3 Motivation

Several complications can arise from inductive heating [37] since in STs, Ohmic heating is suitable only for startup because as temperature increases, resistance decreases, and the Ohmic heating becomes less effective, which is why ohmic heating can be available to control plasma current and its profile, rather than plasma start-up. As a consequence, there were over 100 non-sustained breakdown shots on JET experiments in 2009 [37], which is why non-inductive heating is prevailing. One non-inductive heating method is known as Neutral Beam Injection (NBI), which was proven effective in terms of global energy confinement scaling [38] as well as local transport scaling [39] since the 80s. A primary drawback for NBI which was known since 1987, however, is that if the plasma density was not above a certain threshold ($n_e \sim 10^{19} m^{-3}$), NBI heating will be rendered ineffective [40]. Another non-inductive heating method is the injection of radio frequency RF electromagnetic waves (EMW) into the plasma, where if certain conditions were met, resonance between EMWs and plasma particles occur (LHW can interact with electrons via Landau damping), driving the plasma particles to collide with each other and therefore elevate the plasma temperature as a result (where the electron can directly absorb the RF heat). This method of heating is primarily divided into: Landau damping [41], transit-time magnetic pumping, ECRH heating (Electron Cyclotron Resonance Heating) [42], and ICRH (Ion Cyclotron Resonance Heating) [43] and IIHH (Ion-Ion Hybrid Resonances) [44], where ECRH is the most famous among all three techniques, given that electron mass is much smaller than ion mass, and therefore building the resonance layer is easier. The primary advantage of RF heating is that it requires no minimum density threshold to operate, which seems to be an attractive feature compared to NBI heating. On the other hand, RF heating has an upper density limit where if surpassed, a reflection layer will be created, preventing EMWs to reach the plasma resonance layer, and therefore rendering the whole technique ineffective. Since both heating techniques (NBI and RF) have opposite problems, where one suffers from low density (NBI), and the other suffers from high density (RF), it comes as no surprise to have a hybrid heating system consisting of both RF and NBI. The scheme is as follows: Plasma in a ST is to be heated using ECRH for density to develop until reaching a certain threshold where the reflection layer prevents ECRH from continuing, during which, a shift to NBI is to be done. Another issue that arises from that hybrid is that the upper density limit for ECRH is sometimes lower than the lower density limit for NBI, depending on the operating frequency of the RF source. In order to tackle this issue, different modes of operation for the EMWs of ECRH are to be thoroughly discussed where the upper density limit can be manipulated and in some optimal cases completely removed. The focus of this work will be to manipulate the different modes of EMWs targeting higher plasma density during the ECRH phase in attempt to overcome the plasma density cutoff limit. Moreover, the concept of Electron Bernstein Wave is to be discussed in details as it plays a key role in achieving higher plasma densities during the RF wave injection phase. Highly efficient excitation of electron Bernstein wave is the primary goal with heating and current drive as the targets.

2. Plasma's RF modes of propagation

There are various modes of propagation of RF waves inside a plasma depending on the polarization, injection position with respect to the magnetic field, injection angle, etc. Some of those modes are to be discussed in detail in this section as the mode selection process significantly depends on the properties of those modes.

2.1 Conventional O-mode heating and current drive

Ordinary O-mode, basically known as electron cyclotron resonance heating (ECRH), operates by polarizing the wave in a transverse electric magnetic (TEM) form such that the wave electric field is linearly polarized along B_0.

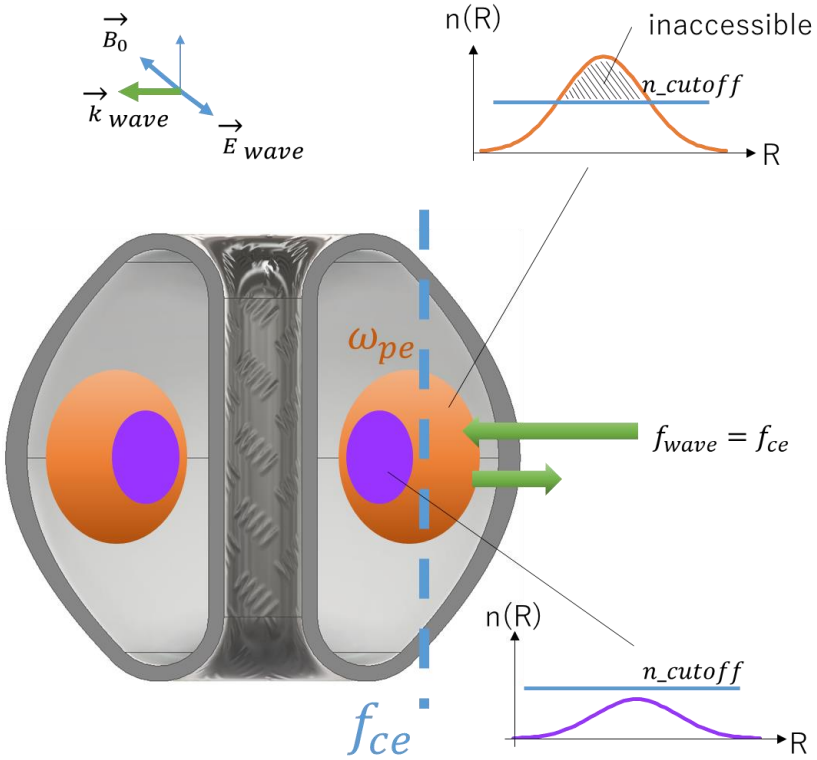

Fig. 6 O-mode injection from low field side, with purple as low density plasma and orange as high density plasma. It can be seen that at low density, resonance layer (f_{ce}) is attainable, but at high density, reflection occurs

The dispersion relation of O-mode, as shown in Fig. 7, is simply expressed as

$$\omega^2 = {\omega_{pe}}^2 + c^2k^2 \qquad 8$$

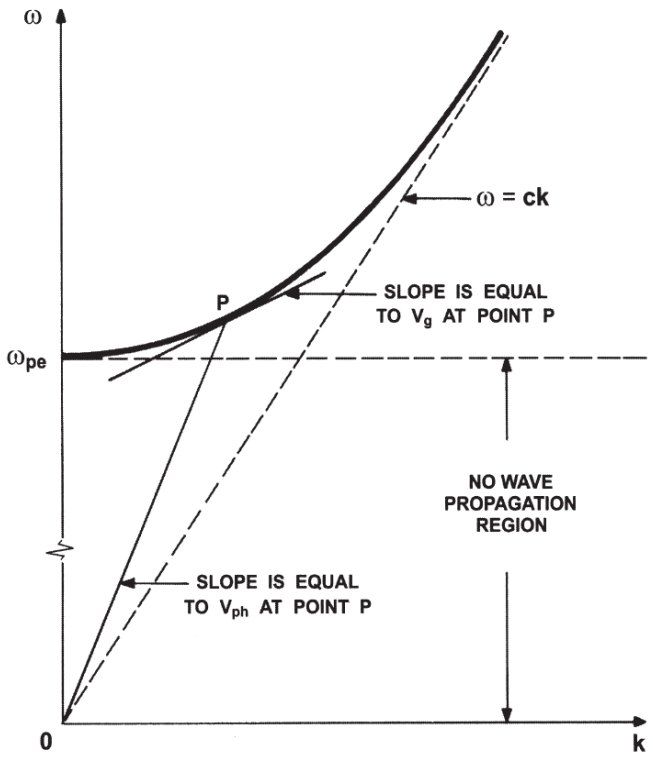

Fig. 7 Dispersion relation for the ordinary O mode propagating perpendicular to magnetic field (from ref. [30]*, where v_g is group velocity and v_{ph} is phase velocity)*

In general, O-mode is simple and effective, but a major drawback is that as density starts to build up, plasma acts as a reflector and RF wave loses access to ECR layer. Therefore, a different mode is required if the target is high density.

This non-inductive plasma heating method have been actively performed in different tokamaks such as MAST [45], TST-2 [46], LATE [47], and QUEST [48], [49]. In [50], a plasma current of 8 kA was reported using 8.2 GHz klystron with power of 70 kW in QUEST.

2.2 Conventional way -X-mode heating and CD

X-mode operates by polarizing the wave in a way such that electric field E_t has a longitudinal component (along k) and a transverse component (perpendicular to k), making this wave partially longitudinal and partially transverse. This is widely known as elliptical polarization. The dispersion relation of X-mode, as shown in Fig. 8, is simply expressed as

$$\frac{c^2\boldsymbol{k}^2}{\omega^2} = 1 - \frac{{\omega_{pe}}^2}{\omega^2}\frac{\omega^2 - {\omega_{pe}}^2}{\omega^2 - {\omega_{UH}}^2} \qquad 2.2.1$$

where ${\omega_{UH}}^2 \equiv {\omega_{ce}}^2 - {\omega_{pe}}^2$ such that ω_{ce} is the electron cyclotron frequency.

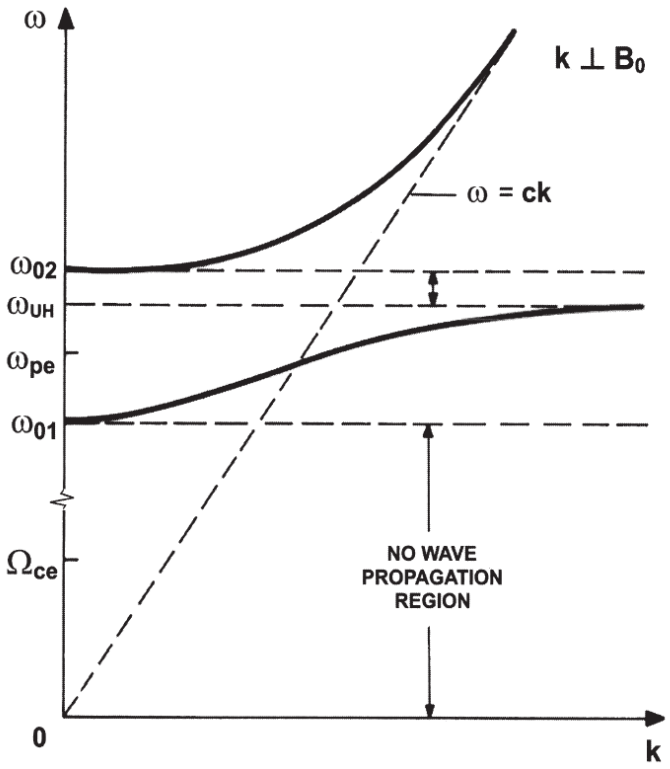

Fig. 8 Dispersion relation for the extraordinary X mode propagating perpendicular to the magnetic field (from ref. [30]*, where* Ω_{ce} *is the ion cyclotron frequency)*

X-mode has a special feature of accessing a layer called the Upper Hybrid Resonance Layer (UHRL), where $\boldsymbol{k} \to \infty$.

For X-modes, increasing the frequency of the source gives access to higher harmonics and thereby nullifying the effect of reflection at high densities. Graphically, this is done by pushing the inaccessible part of the plasma to the left, while creating another resonance layer at a higher harmonic (see Fig. 9).

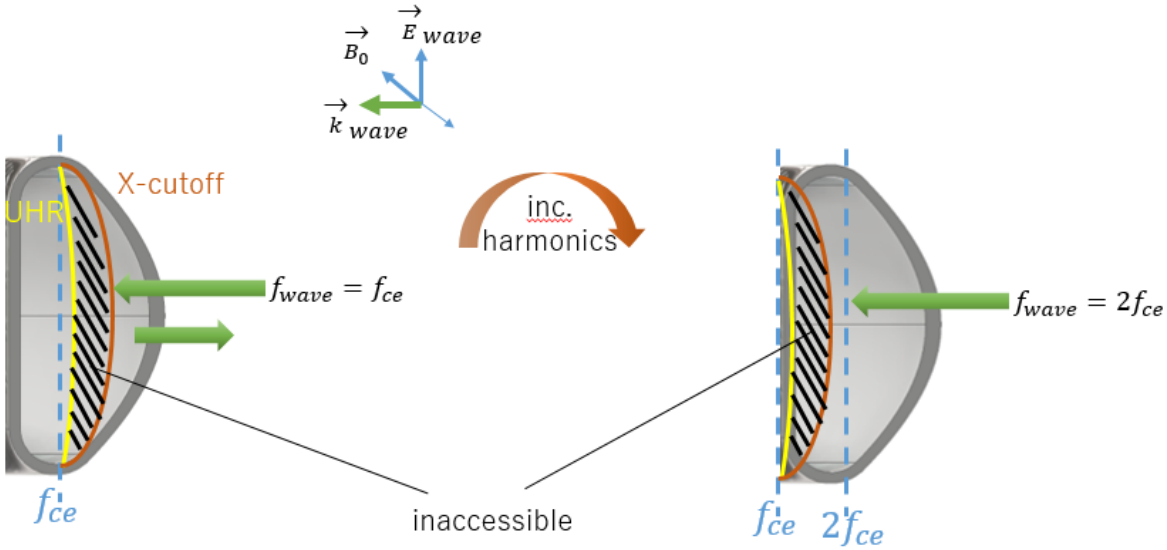

Fig. 9 X-mode launch from low field side such that increasing the wave frequency to the 2nd harmonic would provide access to the second harmonic resonance layer.

In X-mode, increasing the frequency seems like an appealing solution whereas resonance layer is accessible, and this process can be repeated at the 3rd harmonic layer and so on for improved results. However, the drawback of this process is that increasing the source frequency reduces the absorption efficiency, which thereby reduces plasma heat and density. Another problem that arises from the same approach of increasing the frequency is that it is technically difficult to engineer a device with high frequency and high power at the same time therefore a different approach is still required.

Given that those two modes are not the only solutions of the dispersion relation, there is a third mode, however, that is conveniently separated from both modes because of polarization orientation difference.

In general, both X-mode and O-mode have the same issue of the inaccessibility of reaching the cyclotron resonance layer once the plasma density is developed due to the cutoff layer, however, X-mode has an attractive feature of conditionally reaching the UHRL, where resonance would occur, and an electrostatic wave called the Bernstein wave will be developed that propagates along the magnetic axis. This electrostatic wave has the merit of being a longitudinal wave and therefore has the immunity of not suffering any cutoff layers, which is why this mode is the target of this work.

2.3 Merit for using Electron Bernstein Wave

Electron Bernstein Wave (or EBW) was first studied by Ira B. Bernstein theoretically in 1958 [51] and experimentally in 1964 [52]. EBWs are electrostatic waves in a magnetized hot plasma. To derive the EBW dispersion relation, it is necessary to understand the profile of the hot plasma dielectric tensor, expressed from [53] as

$$\epsilon = \boldsymbol{I} + \frac{{\omega_{pe}}^2}{\omega^2}\zeta_0 \sum_{n=-\infty}^{\infty} \begin{bmatrix} \frac{n^2}{\mu}\widetilde{I_n}Z_n & in\widetilde{I'_n}Z_n & -n\sqrt{\frac{2}{\mu}}\widetilde{I_n}(1+\zeta_n Z_n) \\ -in\widetilde{I'_n}Z_n & \left(\frac{n^2}{\mu}\widetilde{I_n} - 2\mu\widetilde{I'_n}\right)Z_n & i\sqrt{2\mu}\widetilde{I'_n}(1+\zeta_n Z_n) \\ -n\sqrt{\frac{2}{\mu}}\widetilde{I_n}(1+\zeta_n Z_n) & -i\sqrt{2\mu}\widetilde{I'_n}(1+\zeta_n Z_n) & 2\zeta_n\widetilde{I_n}(1+\zeta_n Z_n) \end{bmatrix} \quad 2.3.1$$

where

$$\zeta_n = (\omega + n\omega_{ce})/(|k_{|\ |}|{v_T}^2) \quad 2.3.2$$

is the frequency distance from the n^{th} cyclotron harmonic resonance,

$$\mu = {k_\perp}^2 {v_T}^2/2\omega_{ce} \quad 2.3.3$$

, plasma dispersion function is

$$Z_n = Z(\zeta_n) = \frac{1}{\sqrt{\pi}} \int_{-\infty}^{\infty} \frac{e^{-s^2}}{s - \zeta_n} ds \qquad 2.3.4$$

, $Im(\zeta_n) > 0$ and $\widetilde{I_n} = e^{-\mu} I_n(\mu)$ and I_n is the n^{th} order modified Bessel function. The hot dielectric tensor ϵ is not only function in ω_{ce} and ω_{pe}, but also in the wave vector $\boldsymbol{k}$ and the temperature v_T, which leads to the electrostatic modes, a different dispersion relation solution. The rise of the Bessel term in ϵ presents a lot of different roots, the Bernstein waves (or B-modes), for a given harmonic, as well as a different root (the X-mode). Given short wavelengths (large gyro radii), the X-mode and the B-mode decouple, hence the mode conversion to B-mode, where the dispersion relation is expressed as

$$\mu = \frac{{\omega_p}^2}{\omega^2} \sum_{l=-\infty}^{\infty} \frac{l^2 \widetilde{I_l}(\mu)}{1 + l\left(\frac{\omega_c}{\omega}\right)} \qquad 2.3.5$$

where the approximations are: the electrostatic approximation where $\boldsymbol{E} \parallel \boldsymbol{n}$ and $Z_n \cong -1/\xi_n$. EBWs are waves generated from the coherent motion of electrons around their guiding centers, which makes them longitudinal waves. The electrons gyrate around perpendicular magnetic field lines such that the Larmor radii are $\rho = \frac{cm_e v_T}{eB}$ where it is assumed that all the electrons gyrate with the same Larmor radius for simplicity. Periodic charge accumulation is in the same direction as the wave vector $\boldsymbol{k}$.

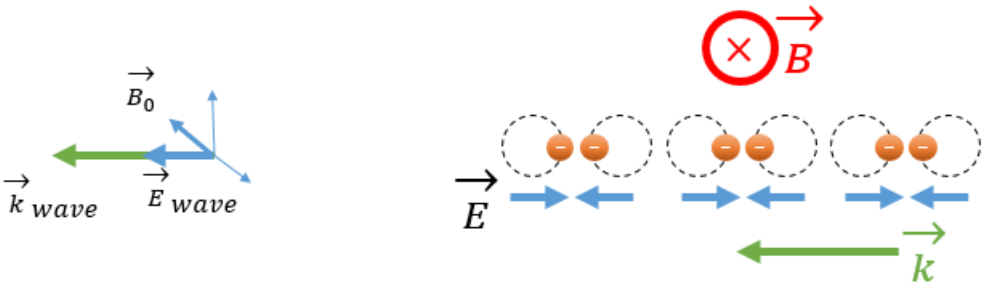

Fig. 10 The orientation of the electrostatic electron Bernstein wave (EBW)

A unique feature of EBW is that EBW wavelength is $4\times$ that of the electron Larmor radius, which would practically eliminate $E \times B$ drift given that $\omega > \omega_c$ [54]. To understand the concept of EBW, a comparison between non-magnetized plasma and magnetized plasma during electric field presence is useful. Non-magnetized plasmas obey Langmuir dispersion

$$\omega^2 = {\omega_p}^2 + 3\boldsymbol{k}^2 {v_T}^2 \qquad 2.3.6$$

However, magnetizing the plasmas would convert electron orbits from back-forth motion to elliptical. These interactions between static magnetic fields and electric fields, distorting the electron orbit, is known as upper hybrid resonance (UHR) such that

$$\omega = \omega_{UHR} = \sqrt{{\omega_p}^2 + {\omega_c}^2} \qquad 2.3.7$$

Increasing the magnetic field causes Lorentz force to overpower the electrostatic force, thus turning the electron orbit to a fully circular form. In such case, EBW can propagate even in over-dense plasmas ($\omega < \omega_p$) as long as ($\omega \leq \omega_c$), which is a key feature for improving plasma density. The reason why such condition exists is because at $\omega_c < \omega_p$, the electrons' orbits are of radius larger than that of the Debye length, exporting the charge disturbance from the inside of the Debye sphere to the external space-charge.

2.3.1 EBW's parametric decay instabilities

The process of exciting EBW produces stimulated electromagnetic emission (SEE) caused by the parametric decay process as the Bernstein waves become parametric instability pumps upon reaching a large enough amplitude [55]. Stubbe and Kopka suggested that EBW's nonlinear scattering of the lower hybrid waves (LHW) might lead to their observed broad symmetric structure [56]. As electrons have significantly lighter masses as compared to the seemingly motionless ions, if electrons oscillate at ω_0 and ions fluctuate at low frequency ω_1, these may beat with oscillating electrons to form $\omega_0 \pm \omega_1$ and $\omega_0 = \omega_1 + \omega_2$, which is the usual resonant mode-mode coupling process as shown in Fig. 11. The spectrum is then shown in Fig. 12

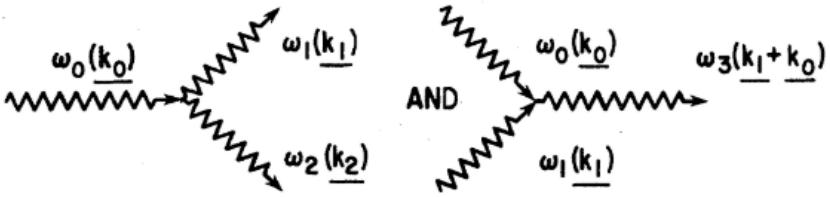

Fig. 11 The formation of LHW ω_1 and two sidebands ω_2 and ω_3 at the EBW mode conversion point such that ω_0 is the pump wave (from ref. [57]*).*

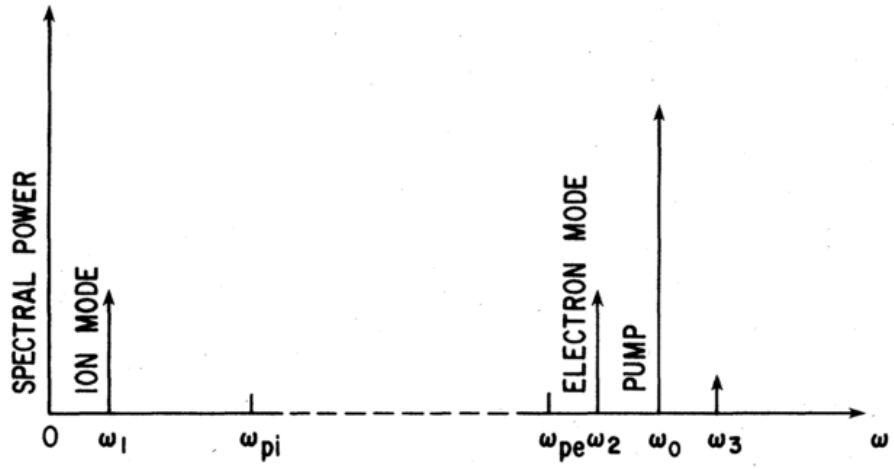

Fig. 12 The PDI spectrum showing the LHW wave at frequency ω_1, and sidebands at frequencies ω_2 and ω_3 where ω_0 is the pump wave.

For confirming EBW mode conversion, EBW's parametric decay instability (PDI) is to be measured. That is, when the injected X-mode wave reaches the UHR layer, scattering occurs during EBW conversion, which causes a sideband to rise next to the central RF frequency [57]–[63] (8.2 GHz in this work), which is to be measured.

2.4 Mode Conversion for EBW

Given that EBWs, by nature, are space charge waves, this means that they require magnetized plasma for propagation, making their excitation only possible inside of the plasma and not from an external source. Electrostatic radiating antennae exist but their inclusion inside of the vessel is obligatory, which is undesirable since millimeter waves are required for high temperature plasma, making the antenna size less than 0.1 mm (same order as that of the electron gyro radius). High temperature plasma, however, has the potential to destroy such antennae, which makes mode conversion into EBW from a different mode, excited externally, the only option for EBW excitation in fusion plasmas. In this section, mode conversion is to be analyzed.

2.4.1 O-X-B mode conversion

For EBW to be excited, a slow X-wave propagating towards the UHR layer is required, which, for the 1st harmonic EBWs, is limited to low densities since for higher harmonics, the UHR will be completely enclosed by the R-cutoff for X-waves. A two mode conversion scheme was first proposed by Preinhaelter [64] where an O-wave is launched from outside of the vessel, with an oblique angle of incidence or a non-vanishing parallel refractive index $n_{||}$. The parallel refractive index $n_{||}$ determines the wave behavior, however, for simplicity, consider the perpendicular refractive index $n_{\perp}$ component along the wave propagation inside of the plasma. It was already established that at $n_{\perp} = 0$, $X = {\omega_{pe}}^2/\omega^2$ and $Y = \omega_{ce}/\omega$, L-mode cutoff corresponds to

$$X = \left(1 - n_{|\ \ |}^2\right)(1 - Y) \tag{2.4.1}$$

, R-mode cutoff corresponds to

$$X = \left(1 - n_{|\ \ |}^2\right)(1 + Y) \tag{2.4.2}$$

and O-mode cutoff corresponds to

$$P = 0 \tag{2.4.3}$$

which, according to the above equations, O-mode cutoff is independent on $n_{||}$. Given that the cutoff position is the limit beyond which the wave cannot propagate, X-waves are to be reflected back from first L-mode cutoff whereas the O-mode will be reflected back from $X = 1$. However, to make use of EBW's feature of propagating in over-dense plasmas, O-modes are to be converted to X-modes at the O-mode cutoff position, which means that R-cutoff has to coincide with O-mode cutoff. The modified equation promoting O-X conversion would then be

$$X = \left(1 - n_{|\ \ |}^2\right)(1 + Y) = 1 \tag{2.4.4}$$

which would in turn make the optimum parallel refractive index

$$n_{||,opt} = \sqrt{Y/1+Y} \qquad 2.4.5$$

the optimal condition for O-X conversion where $\omega_p = \omega$ [65].
The wave converts from O-mode to X-mode without losing energy optimally, but for non-the optimal case, the O-mode partially penetrates through the evanescent layer and partially reflects back, with a transmission coefficient

$$T_{OX} = \frac{P_{X-mode}}{P_{O-mode}} = exp\left\{-\frac{\pi}{8}\sqrt{\frac{2}{Y}}\frac{\omega}{c}\kappa^{-1}\left(\left(\frac{Y+1}{Y}\right)^2\left(\frac{Y}{Y+1} - n_{|\ \ |}{}^2\right)^2 + 2Yn_y{}^2\right)\right\} \qquad 2.4.6$$

first proposed by Preinhaelter in 1975 (Preinhaelter, Penetration of an ordinary wave into a weakly inhomogeneous magnetoplasma at oblique incidence, 1975) where $\kappa = d.\ln n/dx$ is the characteristic length of the density inhomogeneity. The expression of the transmission coefficient in its analytical form was later provided by Weitzner and Batchelor (Weitzner & Batchelor, 1979), Zharov (Zharov & Kotov, 1984) and Mjølhus (Mjølhus, 1983). Hansen then compared all four formulae of the previously mentioned literature (Hansen, Lynov, Maroli, & Petrillo, 1988) where he found out that Mjølhus's formula is best agrees with reality

$$T_{OX}\left(n_{|\ \ |}, n_y\right) = exp\left[-\pi k_0 L_{n,co}\sqrt{\frac{Y}{2}}\left(2(Y+1)\left(n_{||,opt} - n_{|\ \ |}\right)^2 + n_y{}^2\right)\right] \qquad 2.4.7$$

ere $L_{n,co} \equiv n_p/\left(\partial n_p/\partial x\right)$ is the density gradient scale length at the O-mode cutoff point and $k_0 = 2\pi/\lambda_0$ such that the analytical estimation is accurate in the case of $k_0 L_n \leq 10$.
After the X-wave generation, propagation towards UHR is expected, during which, cold plasma approximation is suitable (neglecting thermal motion of electrons). The wavelength decreases at the UHR such that electron gyro radius is achieved during which hot plasma approximation has to be considered (at which the X-mode coincides with EBW). Linearly, X-waves are converted to EBW (X-B conversion), however, the entire O-X-B conversion scheme can only be achieved if the plasma density is above the O-wave cutoff density [66]. The OXB heating scheme in high density high confinement was successfully demonstrated for the first time in the stellarator W7-AS [67] with detailed description of W7-AS and its 70 GHz gyrotron system found in [68].

2.4.1.1 O-X-B conversion from low field side

Injecting RF simply from the low field side (LFS) of the vessel is the conventional method for including ECRH in tokamaks. Conventionally, ordinary O-mode is the non-polarized non-modulated output of the RF source, which is convenient to just inject it into the plasma from the LFS. However, in order to aim for O-X-B conversion, full penetration of the vessel cross section is required, and at the center stack, a grooved mirror polarizer is required to convert O-mode to X-mode, which would then hit the upper hybrid resonance (UHR) layer and convert to B-mode, thus building up plasma density.

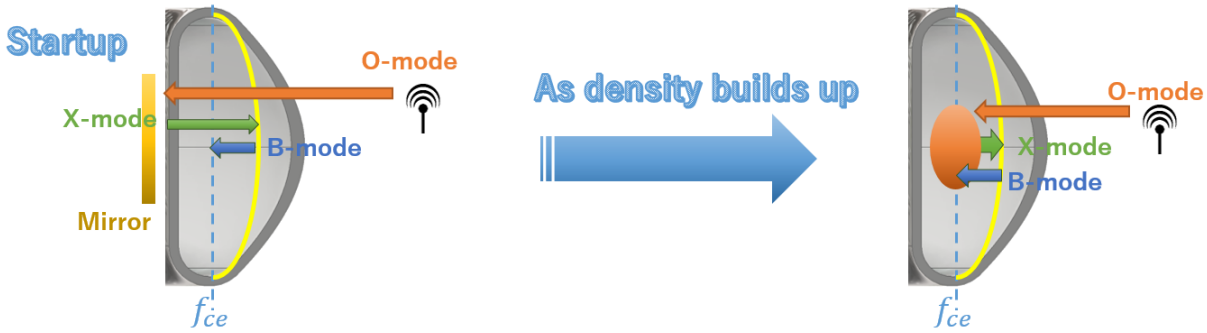

Fig. 13 Time evolution of plasma building up density from O-X-B conversion from LFS where the figure to the left shows the ray path during under-dense plasma for a reflective mirror polarizer at the HFS, and as the density builds up, the ray path changes to be as the right figure represents.

However, as shown in Fig. 13, as plasma density builds up, the reflection path gets shorter rendering the mirror polarizer pointless. Nonetheless, full access to O-X-B conversion is still available as with density higher than O-cutoff, plasma itself acts as the grooved mirror polarizer, converting O-mode waves into X-mode, which would hit the UHR layer from the inner part, effectively converting to B-mode. This scheme is effective in all stages of plasma density as access to UHR layer is always available, which means B-mode is attainable and therefore virtually limitless plasma density is possible to build during this stage. A major drawback with this scheme, however, is that it is extremely difficult to control. Basically, not only does the O-mode wave have to travel for a long distance (from the LFS all the way to HFS), penetrate the ECRH layer which would make it lose some power, but it also needs to be incident at precisely the right angle to hit the grooved mirror polarizer with the right angle to reflect into X-mode with proper angle of incidence for UHR layer access. As simple as this method seems, it is rather difficult to control given that all the action occurs inside of the vessel and away from the engineering reach. It is noteworthy to mention that this scenario at high density is comparatively much easier than at lower density, where the wave does not have to travel for extended distances.

2.4.2 X-B mode conversion

X-B mode conversion can be divided into two scenarios: high field side (HFS) X-B mode injection and low field side (LFS) X-B mode injection. Both systems are to be discussed in details in this section.

2.4.2.1 X-B mode conversion with HFS injection

This launching scenario is only possible with first harmonic X-wave. The UHR layer can be accessed by crossing the ECR layer from HFS instead of increasing the harmonics of X-mode since it is not screened by the R-cutoff completely. The slow X-waves approach UHR as is shown in Fig. 14

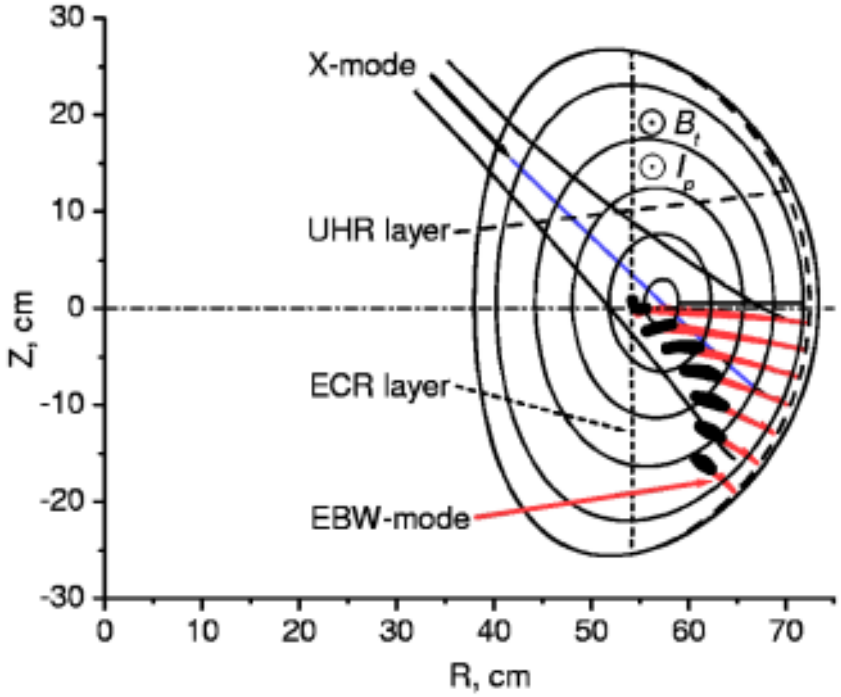

Fig. 14 Poloidal projection of EBW ray-tracing results for the X-mode launched form HFS perpendicular to magnetic field (from ref. [69]*).*

This scheme is particularly attractive for plasma startup and EBW current drive (EBWCD) since plasma has to be transparent for X-waves. No X-wave propagation is possible once the plasma density exceeds L-cutoff, limiting this scheme to not operate in over-dense plasma condition. HFS X-mode injection experiments have been reported by several authors such as the direct injection of SX-mode in Large Helical Device (LHD) [66]. In this scenario, two existing antennae installed in a lower port of the vacuum vessel can be used without a central stack mirror [70]. This method is useful for local heating and current drive given the flexibility of the wave propagation angle, allowing the wave to be launched obliquely to external magnetic field, allowing access to ECR as well as UHR layers. Fundamental X-mode perpendicular propagation experiences much weaker absorption compared to oblique propagation [71]. Given that the electron density was less than the cutoff density, absorption during both phases (X-mode and EBW) can occur [72]. Various other experiments are listed as follows: McDermott et al. at the Versator 2 Tokamak [60] as well as Willhelm et al. at the Wendelstein 7-A stellarator [73], and finally, the Doppler-shifted power deposition was measured in the LATE tokamak [74]. Different modifications were however reported [45] with a system consisting of O-mode injected from LFS, converted into X-mode after reflecting from a grooved mirror polarizer incorporated with a graphite tile on the central rod. The polarizer converts the O-mode into an X-mode that propagates back into the plasma, passing through the ECR layer and converting once more to EBW near the UHR, which is then absorbed before reaching the ECR due to Doppler-shifted resonance as is shown in Fig. 9. The model shows that $< 2\%$ of the injected power is absorbed during the O- and X-modes conversions.

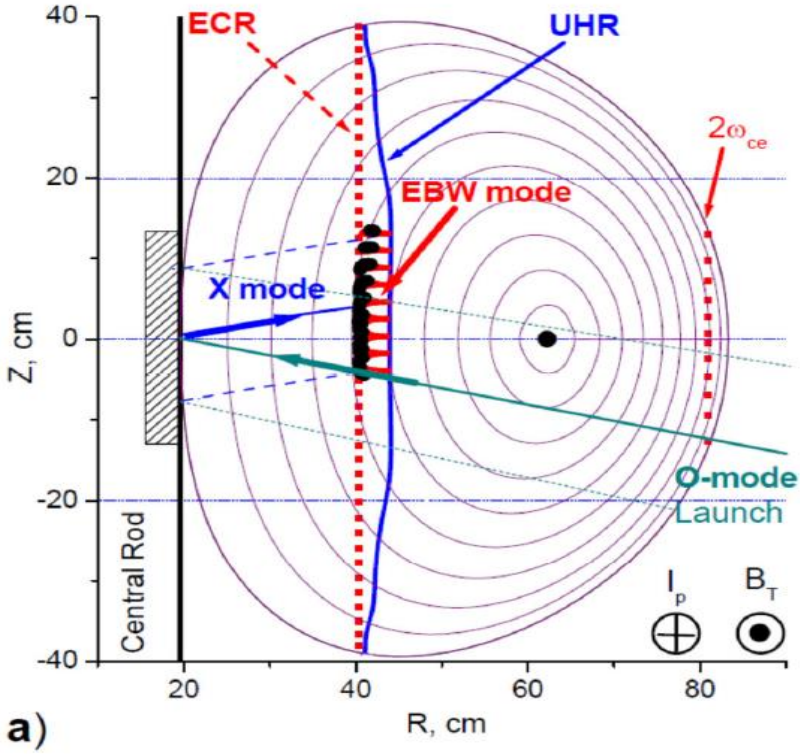

Fig. 15 EBW assisted plasma current startup schematic. Poloidal projection of EBW ray-tracing based on the plasma equilibrium reconstructed from experimental data (from ref. [45]*) using 28 GHz gyrotron and 100 kW RF power.*

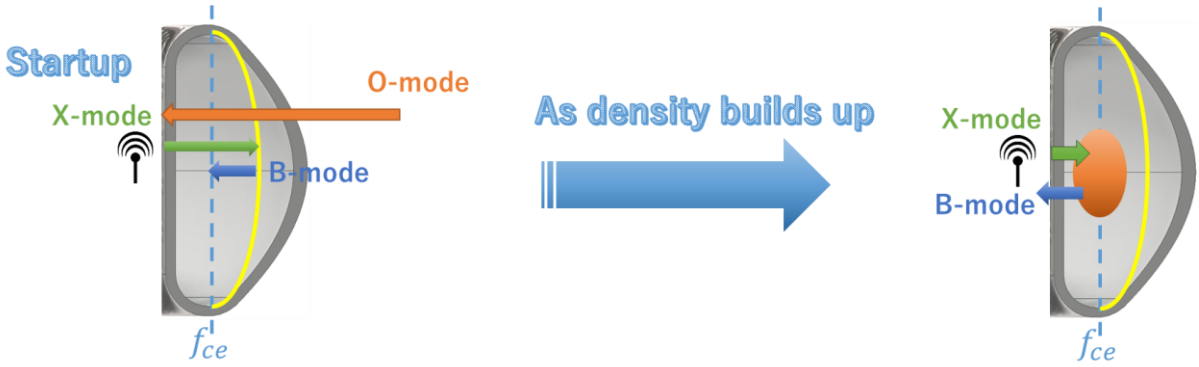

Fig. 16 Time evolution of plasma building up density from X-B conversion from HFS

As shown in Fig. 8, as plasma density builds up, X-mode waves reflect back before reaching the UHR layer, giving no chance for B-mode to be excited inside of the plasma. The major advantage of this scheme is that achieving B-mode in startup is easy to control. However, one disadvantage is that after plasma density builds up, reflection is bound to occur rendering this scheme ineffective at higher densities. The primary limitation of this technique however, lies within the difficulty to implement. Including a waveguide in the center stack means removing the center solenoid completely as well as the injection should occur at an angle normal to that of the tokamak surface (horizontal angle) to ensure proper X-mode propagation inside of the plasma.

3. Modelling of HFS injection in QUEST

Various modelling tools exist to serve the purpose of simulating the effect of RF propagation and absorption in QUEST. To first assess the RF behavior inside of the plasmas, the magnetic profile is to be investigated. Afterwards, ray tracing or full wave simulations can be used to compute the behavior of the RF wave after inputting the magnetic profile.

3.1 EFIT

In 1985, L. Lao, et al. developed a Magneto hydrodynamics (MHD)-based equilibrium fitting code called EFIT [75]. It was developed to analyze the Doublet III tokamak magnetic topology. Later on, a National Fusion facility called DIII–D based in San Diego, USA, as well as other tokamaks around the world adopted it. EFIT is a FORTRAN-based code that processes diagnostic measurements as inputs (magnetic probes, magnetic coils, flux loops and Motional Stark Effect), and outputs the magnetic reconstruction profile (magnetic geometry), stored energy and plasma current profile.

In QUEST, 67 poloidal flux loops are placed around the vessel's cross section for picking up flux information as shown in Fig. 17.

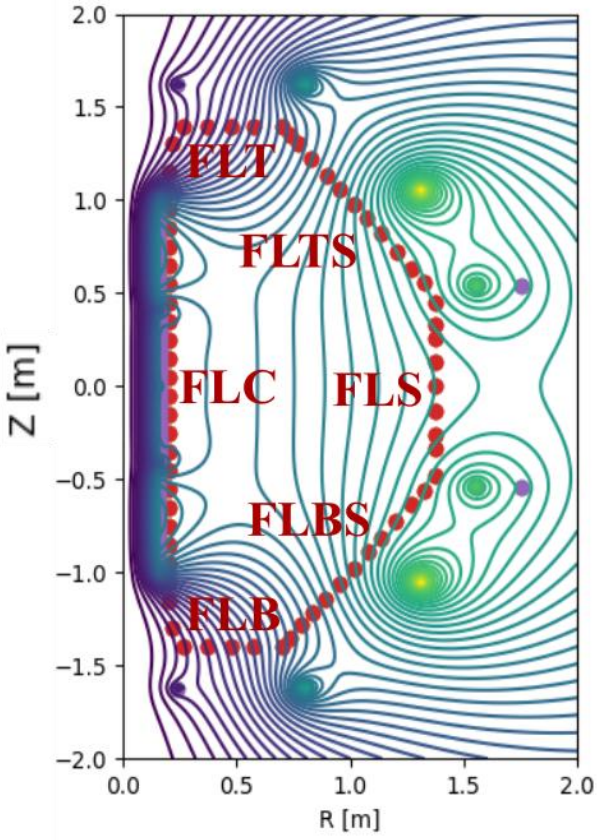

Fig. 17 QUEST poloidal field profile is shown with dark red representing flux loop positions such that FLT is flux loops top, FLC is flux loops center, FLB is flux loops bottom, FLS is flux loops side, FLTS is flux loops top-side and FLBS is flux loops bottom-side.

Flux profile is measured without plasma (vacuum shot), and with plasma (plasma shot), and both information sources are inputted to EFIT to determine the last closed flux surface (LCFS) which is essential for understanding plasma behavior. At first, the green table is to be preconfigured by

logging all the PF coil specifications as well as the power supply specifications. Afterwards, EFUND should be calculated and updated in the green table (this process should happen once before each campaign at least). Essentially, EFUND is the calculation of the mutual inductance such that

$$\frac{A_\varphi}{I} = \frac{\mu a}{\pi} \int_0^{\pi/2} \frac{(2sin^2\theta - 1)d\theta}{[(a+R)^2 + z^2 - 4aRsin^2\theta]^{\frac{1}{2}}} \quad 3.1.1$$

where A_φ is the mutual flux, μ is the permeability, I is the coil current, a is the radial location of the coil, R is the radial axis, z is the vertical axis, and θ is the elevation angle. A_φ can be expressed as follows:

$$\frac{A_\varphi}{I} = \frac{\mu}{\pi k}\left(\frac{a}{R}\right)^{\frac{1}{2}}\left[\left(1 - \frac{1}{2}k^2\right)K - E\right] \quad 3.1.2$$

where k is

$$k^2 = 4aR[(a+R)^2 + z^2]^{-1} \quad 3.1.3$$

such that K and E are the elliptic integrations of k. The mutual inductance can then be calculated as

$$M = 2\pi R\frac{A_\varphi}{I} \quad 3.1.4$$

This information should be inputted in the green table. The contents of green table are:

- $M_{PF-grid}$
- $M_{grid-grid}$
- $M_{flux-grid}$
- $M_{flux-PF}$

where M is predetermined since the PF coil and flux loop positions are stationary, and grid is essentially the resolution of the 2D output.

EFIT reads two inputs: (a) green table, and (b) QUEST's diagnostics data and generates one output: g-file. QUEST's diagnostics data include:

- Magnetic data (from flux loops)
- PF coil currents
- Plasma current, Ip

EFIT uses the time evolution of all its inputs to calculate a time-varying reconstruction of the magnetic profile. A sample is shown in Fig. 18.

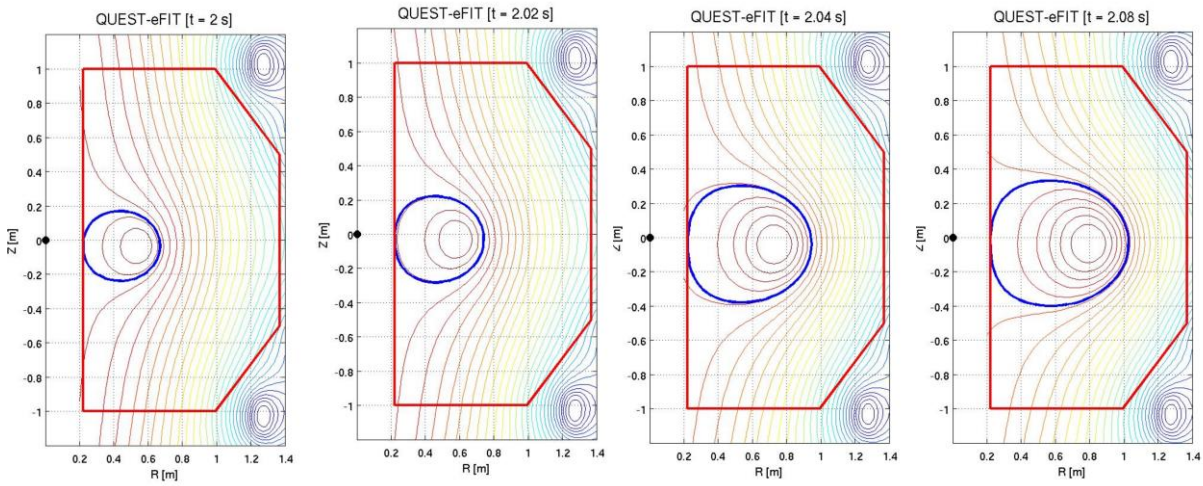

Fig. 18 Different time snaps of a magnetic reconstruction output from EFIT to demonstrate the time evolution of the last closed flux surface (LCFS) where the blue line represents the last closed flux surface and the red lines represent the layout of the QUEST vessel

Flux loop inspection is sometimes required as hardware failure occurs on occasion. A matlab code was developed to acquire and investigate flux loop data and compare it to the theoretically calculated flux at the flux loop positions. It should be noted that this technique can only be used in the vacuum shots. First, the raw signal is to be acquired, then passed through an integrator, then passed through a drift removal system. Flux (for vacuum shots) is analytically calculated as follows:

$$flux = M * I_{PF} \qquad 3.1.5$$

A sample result of the flux loop measurement as compared to the theoretical calculation is shown in Fig. 19.

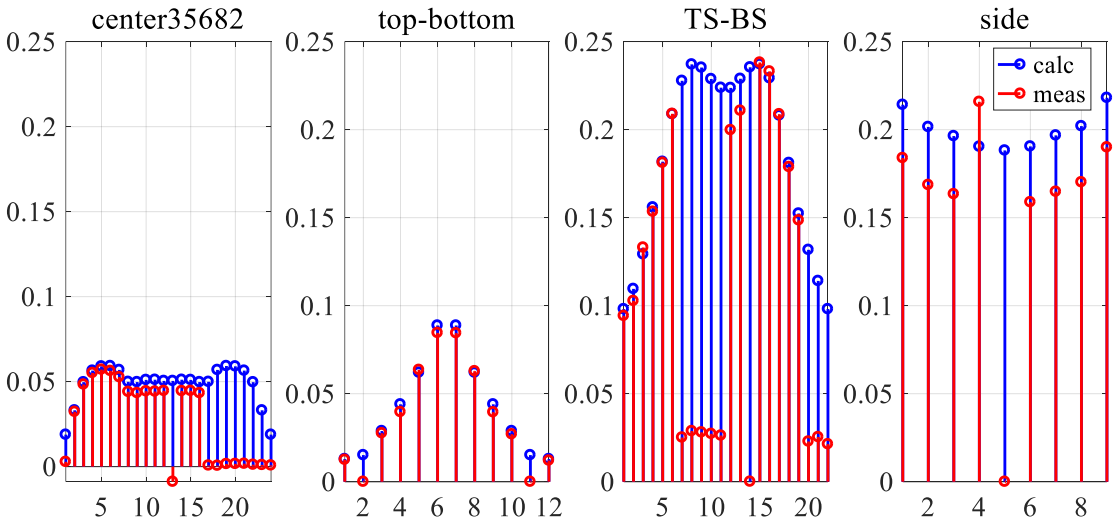

Fig. 19 Flux loop peaks such as (left) center flux loops (FLC), (left-middle) top (FLT) and bottom (FLB) flux loop peaks, (middle-right) Top side bad bottom side flux loop peaks (FLTS and FLBS), and (right) is side flux loop peaks (FLS) such that red is the measured signals after integration and drift removal, and blue is the calculated mutual flux that matches this shot at the flux loop

positions. The x-axis in those figures resembles the flux loop numbers, while the y-axis resembles the flux value.

In Fig. 19, it can be seen that the non-matching flux loops are faulty, so they should be ascribed a lower weight in EFIT, as compared to the matching flux loops. After the weights are properly ascribed, the input data paths are pointed to using matlab, then the FORTRAN code is compiled. An output error indicator x^2 is calculated as a metric for the fitting quality such that:

$$x^2 = \frac{\sum(flux_{measured} - flux_{calculated})^2}{\sigma^2} \tag{3.1.6}$$

such that

$$flux_{calculated} = M * I_{PF} + M \int Ip \tag{3.1.7}$$

where I_{PF} is PF coil current and σ^2 is the threshold for quality fitting. In general, x^2 should be less than 100 and for the flux loop positions where x^2 is more, either the flux loop should be turned off (by ascribing 0 weight), or adjusting σ^2 in case all flux loops are higher and flux loop inspection did not result in having faulty hardware, but this method will put the accuracy of the reconstruction into question.

3.2 GENRAY

GENRAY is a configurable RF ray tracing code originally written by A. P. Smirnov and R. W. Harvey in 1995 [76], which uses geometrical optics approximation to trace the trajectory of RF waves. This code can be applied for a variety of frequencies (electron cyclotron, EBW, lower hybrid and fast wave).
GENRAY's general ray tracing equations are as follows:

$$\frac{d\boldsymbol{r}}{dt} = \frac{\partial\omega}{\partial\boldsymbol{k}} \left(= -\frac{\partial D/\partial\boldsymbol{k}}{\partial D/\partial\omega} = \boldsymbol{v_g} \right) \tag{3.2.1}$$

where

$$\frac{d\boldsymbol{k}}{dt} = -\frac{\partial\omega}{\partial\boldsymbol{r}} \tag{3.2.2}$$

such that $D(\boldsymbol{r}, \boldsymbol{k}, \omega, t) = 0$ is the dispersion function.

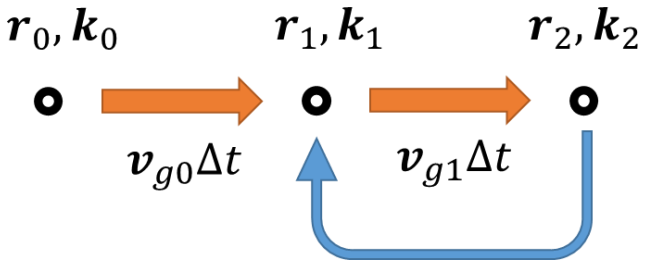

Fig. 20 The iterative feedback process of the GENRAY's tracing calculation

As GENRAY is highly configurable, dispersion relations are to be configured along with mode conversion scenarios.
GENRAY's inputs are:

- Magnetic equilibrium output file of EFIT (g-file)
- Configurable input name list: dispersion, absorption, launch mode, launch position, launch angle, plasma density, plasma temperature, etc.

Afterwards, GENRAY outputs ray trajectory and power deposition.

GENRAY ray tracing simulation of HFS injection of X-mode for EBW conversion in QUEST was previously conducted by R. Yoneda et al. [77], showing accessibility of X-mode to reach UHR for various values of plasma density.

Further analysis was conducted to match QUEST's current specifications and to investigate the current drive. As plasma start-up and EBW current drive is targetted, up-down shift of the mode converstion point is a necessity to drive plasma current as the current direction depends on the up-down shift of mode conversion point. Since GENRAY assumes a perfect ray, it will not take into account the undesired ECR absorption due to diffraction from open-ended waveguide. To compensate for this assumption, we assume that the power intercepted by the UHR (40 kW) is the injection power at the HFS (based on calculations to be shown in the next section).
Two injection angles of $\pm 10^{\circ}$ are proposed at plasma density of $5 \times 10^{17} m^{-3}$ and temperature of $50eV$ driving plasma current of approximately 10 kA. In the ideal case where the injected power is 50 kW, driven plasma current is approximately 13 kA. Fig. 21 shows the poloidal view of QUEST with the X-mode injected from HFS penetrating the fundamental ECR layer (dashed magenta line), reaching the UHR layer and reflecting back a little. The dark orange line represents the $+10^{\circ}$ injection angle and the turquoise line represents the -10° injection angle. It should be noted that the EFIT magnetic reconstruction was used to calculate and the center of up-down symmetry was shifted by 2 cm. Fig. 21 (right) shows the toroidal (top) view of QUEST, where the $+10^{\circ}$ injection angle is converted to EBW and is propagating along the toroidal magnetic field in the clockwise direction, while the -10° injection angle is converted to EBW but is propagating in the counter clockwise direction. Collisional damping is the dominant damping mechanism in this scenario (but this depends on plasma temperature). In Fig. 22, the maximum value of the average current density of both injection angles is about $385A.cm^{-2}$.

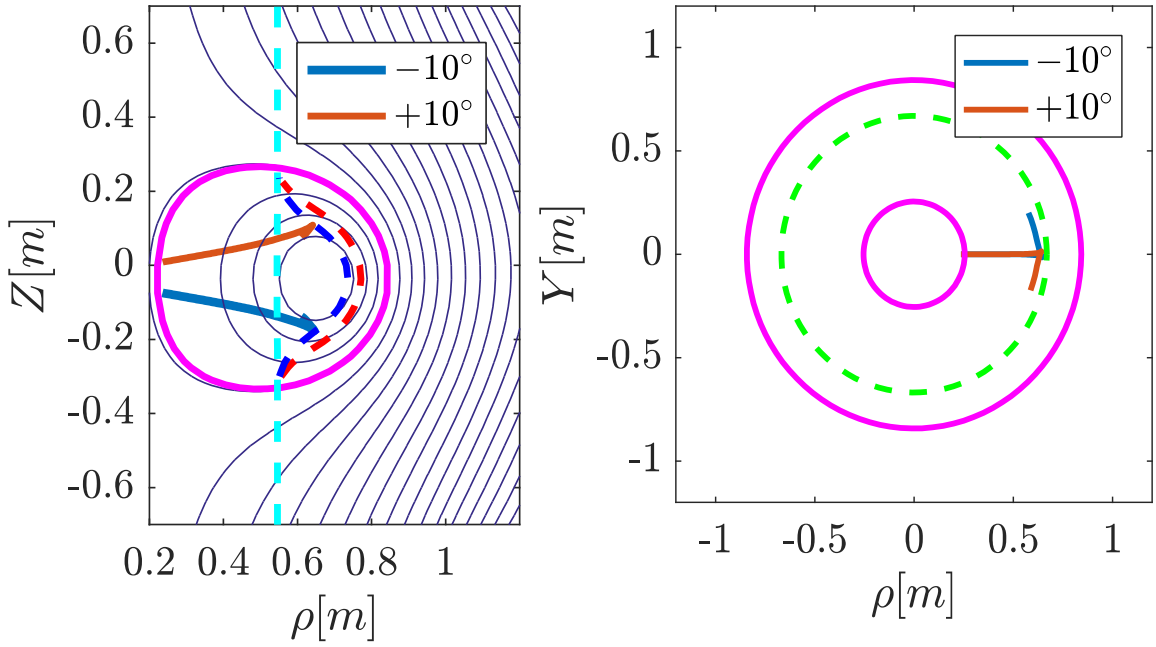

Fig. 21 (Right) Poloidal cross section of the HFS injected ray such that the dashed magenta line represents the fundamental ECR layer, the dashed blue line represents the UHR layer and the dashed red line represents the X-cutoff layer. (Left) Toroidal cross section

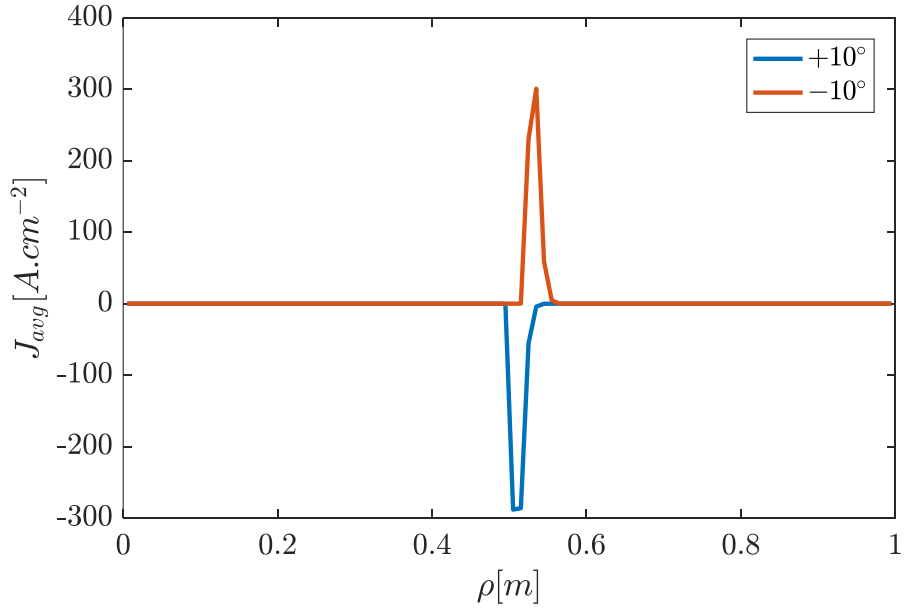

Fig. 22 Average current density as a function in major radius ρ for two injection angles at plasma density of ne=5×1017m-3 and plasma temperature of 50eV. The sign of J_{avg} indicates the direction of propagation (+ve is clockwise and -ve is counter clockwise)

As our primary target is density buildup, we incremented the density value and GENRAY's ray trace and ouput plasma current. The results are shown in Fig. 23.

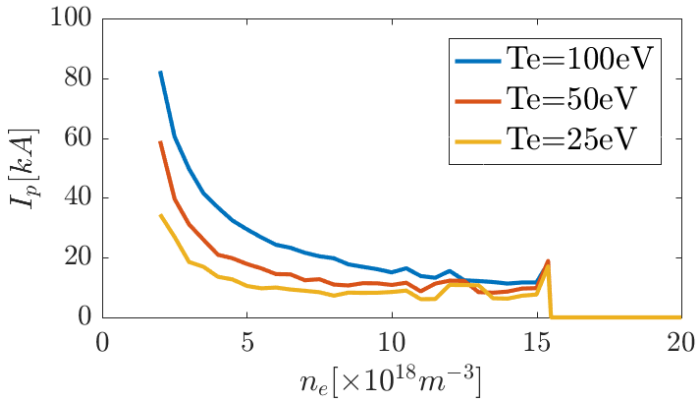

Fig. 23 Plasma current as a function in density, where n_e is the peak value of the density's assumed Gaussian profile.

Fig. 23 shows that the density buildup can reach up to $1.54 \times 10^{18} m^{-3}$ before the ω_{pe} starts building up that would bend the ray, preventing its access to UHR, which is visualized in Fig. 24. In that case, to further increase the density, one can either increase injection direction by increasing the tilt angle of the incident X-mode or its launch position, or another method as propsed in [77] is to switch to LFS O-mode. In case of switching to O-mode, mode conversion to X-mode can occur easily at the O-mode cutoff layer, which can then intercept the UHR mode to convert to EBW.

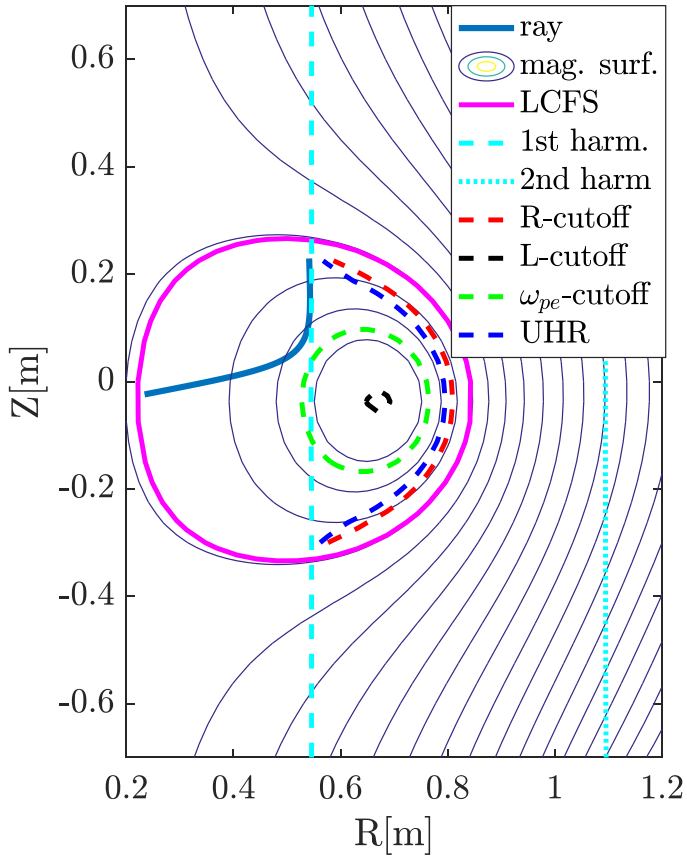

Fig. 24 Poloidal view of ray not accessing UHR due to density build-up such that; mag. surf. is the magnetic surface calculated by GENRAY, LCFS is the last closed flux surface, 1st harm. and 2nd harm are the fundamental and 2nd ECR harmonic layers

4. System design of HFS injection

QUEST has a target of non-inductively driving plasma current, primarily through RF heating and current drive. In 2011, QUEST successfully executed a fully non-inductive startup achieving a plasma current of 15 kA for 1 s using 8.2 GHz klystron without depending on the injection angle or mode of propagation, suggesting that EBW did not contribute to the startup [32]. During this experimental campaign, plasma density of $3 \times 10^{17} m^{-3}$ was achieved.

The use of mirror polarizers for converting the LFS O-mode to HFS X-mode has natural limitations. One limitation is the requirement for plasma to be transparent enough for the O-mode to propagate through the plasma without a large degree of diffraction that deflects the RF wave, preventing it from accessing the mirror polarizer. To ensure proper transparency, the plasma density must be fairly low such that the plasma frequency ω_{pe} is much smaller than the RF frequency ω_{RF}. This phenomenon still exists in the case of HFS injection using waveguide as the ray will be bent in higher density, preventing well-controlled power deposition. However, EBW excitation causes plasma density to build up to a point where X-mode cutoff (X-cutoff) precedes UHR, preventing X-mode to convert to EBW [78]. This upper density limit is undesirable as the primary purpose of EBW excitation in QUEST is density build-up.

The other limitation for using a mirror polarizer is its size requirements and its dependency on RF frequency of operation, which in turn depends on the toroidal field strength as well as the overall structure of the tokamak.

In order to achieve better EBW excitation, RF power delivery from LFS to HFS via waveguides is proposed as shown in Fig. 25. This will, in turn, omit the need for a mirror polarizer, hence any range of RF frequency can be used. In this setup, atmospheric RG-50 waveguides made of Aluminum and Copper are used to connect the klystrons K1 and K2 to the vessel, while vacuum waveguides made of Copper are inserted in the vessel, connecting LFS and HFS. Several waveguides can be installed, creating an array of antennas at the HFS, allowing for beam steering using phase controllers (PC) at the atmospheric side, however, due to engineering complexity and limited space, only two waveguides are to be installed which would make beam steering effectively impossible. A major issue with this setup is that the waveguide must traverse the ECRL, inducing breakdown inside of the waveguide [79]. This will render the setup moot as no power will be delivered to HFS, dictating the necessity of investigating the breakdown effect of the magnetic field inside the waveguide. Proposed is to fill the waveguide with SF_6 to prevent breakdown from occurring in the ECR layer, then a vacuum window is to be positioned past the ECR layer to preserve the vessel vacuum condition. Another issue that arises within this setup is the diffraction of the X-mode wave upon exiting the waveguide antenna. This diffraction will cause non-perpendicular X-mode wave propagation from HFS, causing undesired absorption in ECRL, reducing the amount of power that reaches UHRL which would decrease the efficiency of EBW excitation. Moreover, placing a directive antenna to focus the injected wave onto the UHR layer by reducing the beamwidth would increase the system efficiency, however, placing the antenna can create geometric limitations as the antenna size is significant enough to cause arcing as it intercepts the plasma core (and correspondingly the ECR layer).

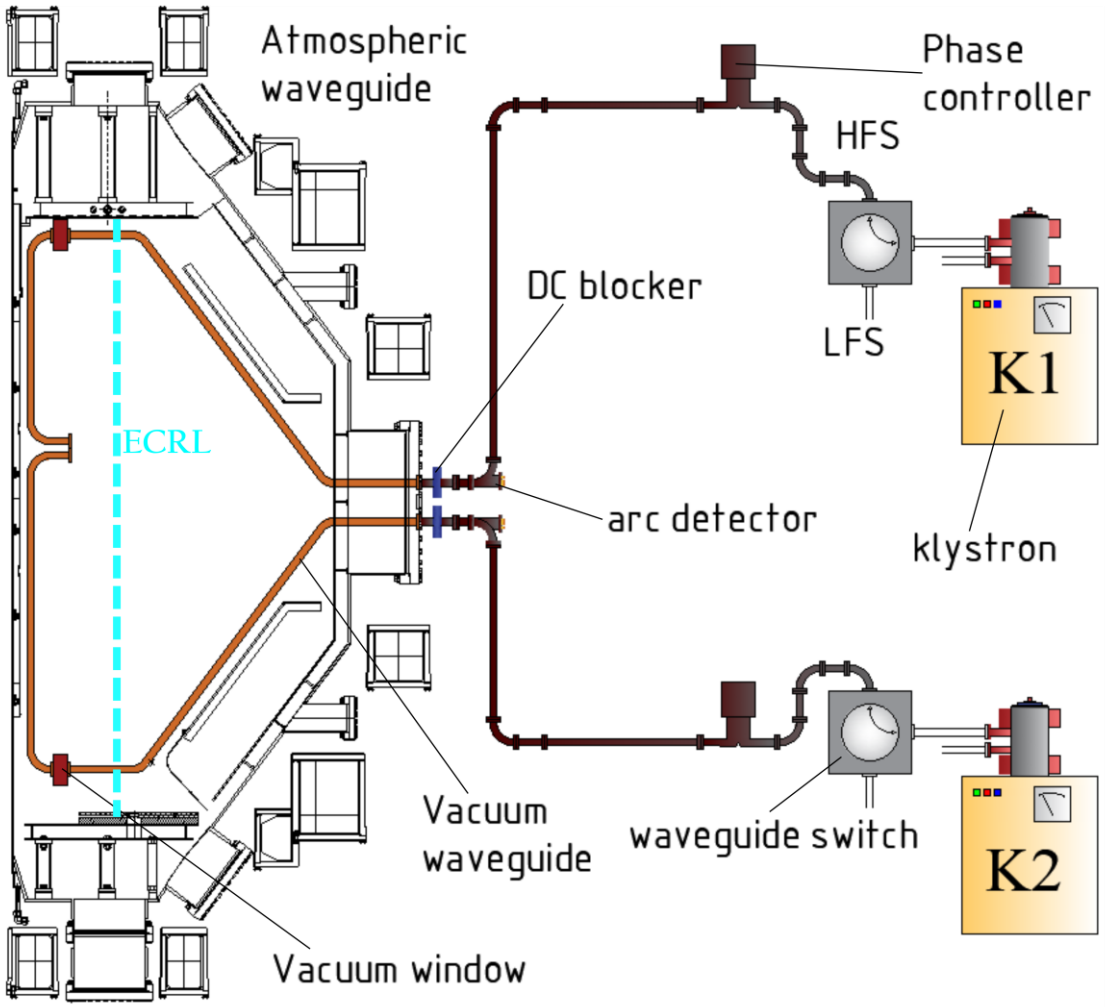

Fig. 25 Setup for power delivery from LFS to HFS in QUEST showing the two klystrons labelled K1 and K2, a waveguide switch to switch between LFS and HFS, an arc detector connected to an interlock system for safety, a DC blocker, and the antennas with the ECRL position shown in perspective.

4.1 Toroidal directivity investigation

TToroidal directivity should be as high as possible to avoid undesired ECR absorption on the beam's pathway towards UHR layer. Typically, for minimal toroidal beam width, a horn antenna is to be used. However, in order to use a horn antenna, its dimensions will force the antenna to intercept ECRL causing arcing to occur within the antenna. The magnetic configuration of choice will make ECRL at $R \approx 0.5m$, which requires an antenna length of no more than $10cm$ that would in turn make the directivity effect of the antenna negligible. Due to limitations in space and to avoid direct contact between antenna and plasma, an open-ended waveguide is to be used. COMSOL was used to calculate the radiation pattern of the RG-50 open-ended waveguide and its losses were estimated for the UHRL power delivery efficiency.

To calculate how much absorption occurs in ECRL from HFS, optical depth Γ is to be calculated. A basic expression of Γ is as follows [78]

$$\Gamma(X,O) = \int 2k_0\chi(X,O)dx \qquad 4.1.1$$

where k_0 is the fundamental wave number and χ is the absorption coefficient such that

$$\chi(X,O) = \frac{\beta_e \cos(\phi)}{4\pi q}(2 + q(1-q)^2) f(\zeta) \quad 4.1.2$$

In equation 4.1.3, q is defined as the plasma to electron cyclotron frequency ratio $q = \omega_{pe}^2/\omega_{ce}^2$, ϕ is defined as the azimuthal angle and $\beta_e = v_t/c$. $f(\zeta)$ is defined as the doppler effect absorption profile such that

$$f(\zeta) = exp(-\zeta^2)/|W(\zeta)|^2 \quad 4.1.3$$

where ζ is the plasma dispersion function defined as $\zeta = (\omega - \omega_{ce})/k_z v_t$ and $W(\zeta)$ is the wave to particle interaction ratio defined as $W(\zeta) = Z(\zeta)/i\sqrt{(\pi)}$ such that $Z(\zeta)$ is the plasma dispersion function. To calculate $k_z = kcos(\phi)$, the cold dispersion relation was used with $\nu = 0$ approximation such that

$$\frac{kc}{\omega} = 1 + \frac{\omega_{pe}^2}{\omega_{ce}^2} + \frac{\omega_{pe}^4}{\omega^2(\omega_{pe}^2 + \omega_{ce}^2)} \quad 4.1.4$$

Moreover, $W(\zeta)$ is evaluated as

$$W(\zeta) = \left(1 + \frac{i2}{\sqrt{(\pi)}}\int_0^{\zeta} exp(y^2)dy\right) exp(-\zeta^2) \quad 4.1.5$$

Substituting in equation 1, Γ can be expressed as

$$\Gamma(X,O) \approx \frac{\pi^2}{2}{\beta_e}^2 cos^2\theta \frac{(2 + q(1-q))^2\sqrt{(2-q)}}{q}\frac{R_0}{\lambda_0} \quad 4.1.6$$

After calculating Γ, the absorbed power in ECRL can be calculated as

$$\frac{P_{abs}}{P_{inc}} = 1 - exp(-\Gamma) \quad 4.1.6$$

where P_{abs} is the absorbed power at the ECRL and P_{inc} is the input (incident) power.

As an open-ended waveguide has much wider beamwidth compared to a horn antenna, the amount of ECR absorption is to be calculated to determine whether this method is feasible or not.

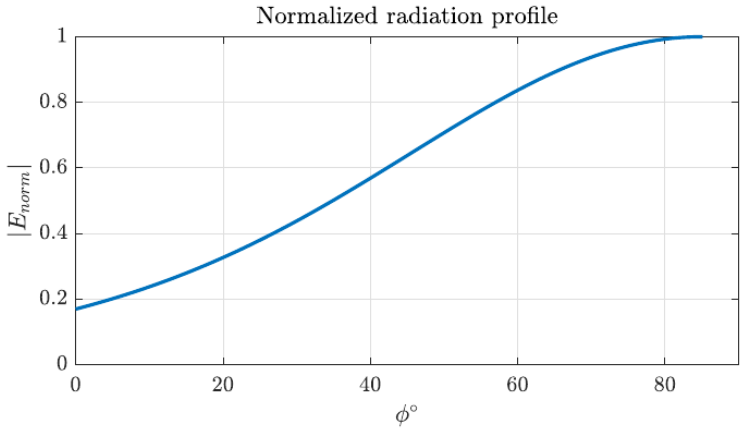

Fig. 26 Normalized open-ended waveguide radiation profile as a function in ϕ

$$L_{abs}(\phi, T_e) = |E_{norm}|^2 \frac{P_{abs}}{P_{inc}} \tag{4.1.7}$$

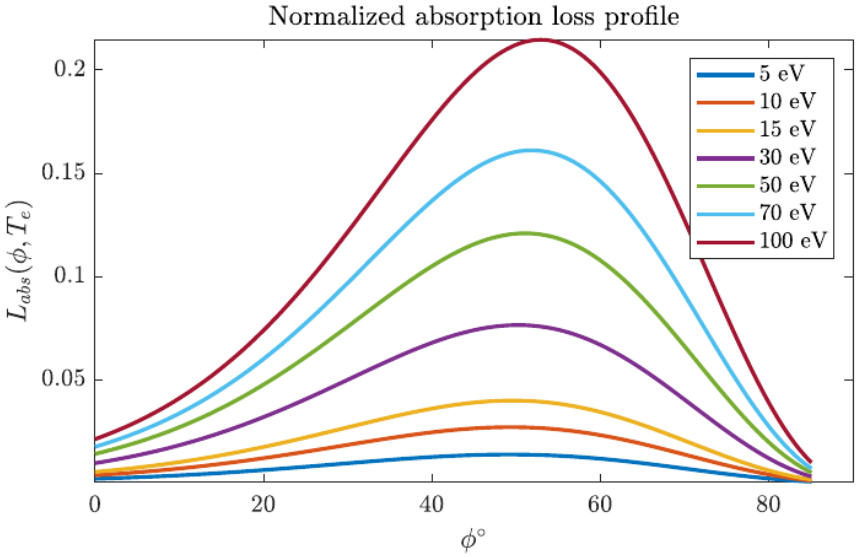

Fig. 27 Normalized absorbed power as a function in ϕ

$$L_{abs}(T_e) = \int_{\phi=0}^{90^\circ} L_{abs}(\phi, T_e) d\phi \tag{4.1.8}$$

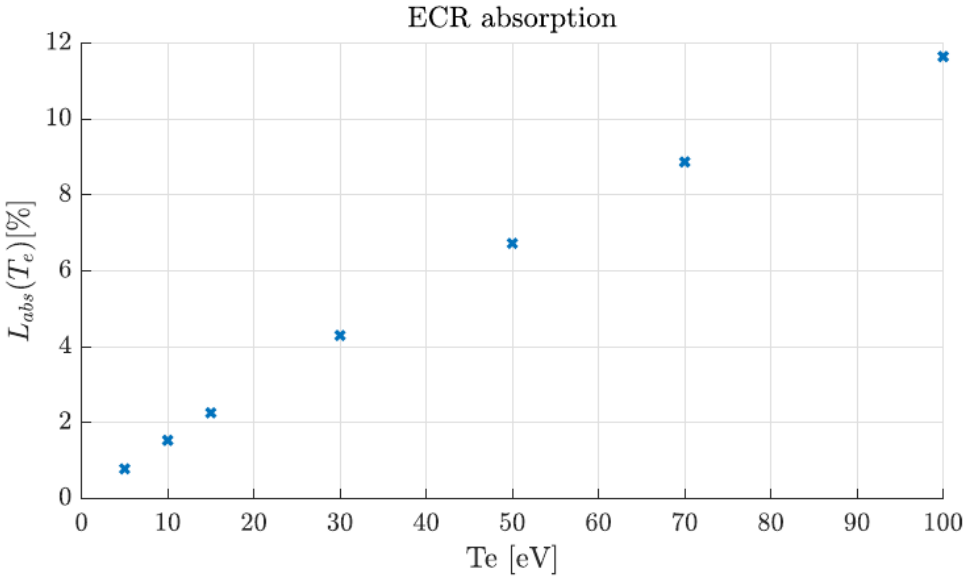

Fig. 28 ECR absorption as a function in electron temperature

Using the open-ended waveguide normalized radiation profile as calculated by COMSOL (Fig. 27), one can calculate the normalized absorption loss profile (Fig. 28) by following the L_{abs} equation. After integrating the absorption loss profile, it can be seen from Fig. 28 that ECRL absorption is no more than 7% of the input power at 50 eV. In the proposed design, two waveguides are to be used, giving a total power of $20 \times 0.93 \times 2 = 37.2$ kW to be intercepted by the UHR layer, where the klystrons are assumed to operate at 80% of their total power.

4.2 HFS system setup in QUEST

The antennae of both waveguides were placed 195 mm above the center line of QUEST to emulate the tilting angle demonstrated by GENRAY, as shown in Fig. 25Fig. 30. The two waveguides are connected to sapphire vacuum windows to prevent SF_6 gas from contaminating the vessel vacuum condition. The assembly has no water cooling channels installed so the shot pulse duration is limited to 100 ms to avoid window cracking or breaking due to RF depositted heat load on the window,

As the windows and waveguides are relatively heavy, a support holding the waveguides to the diverter plate was used. Moreover, a waveguide guard made of stainless steel was used to protect the waveguides from plasma impact. The final assembly in QUEST is shown in Fig. 29. In addition, a tungsten protector at the antenna port was installed. Moreover, the real estate at the stainless steel guard was taken advantage of by installing 2 Langmuir probes at the mid-plane and at the antenna launch position. The included tungsten plate as well as the Langmuir probes are shown in Fig. 30.

In order to compare between HFS injection and LFS injection, several limitations to this setup exist, including the fact that the HFS antennae is displaced 195 mm vertically above the mid-plane while the LFS antennae is placed 120 mm below the mid-plane. Another limitation is regarding the radial locations of the HFS and LFS antennae. The HFS antennae are radially much closer to the ECRL than the LFS antennae allowing for more dispersion in the case of LFS

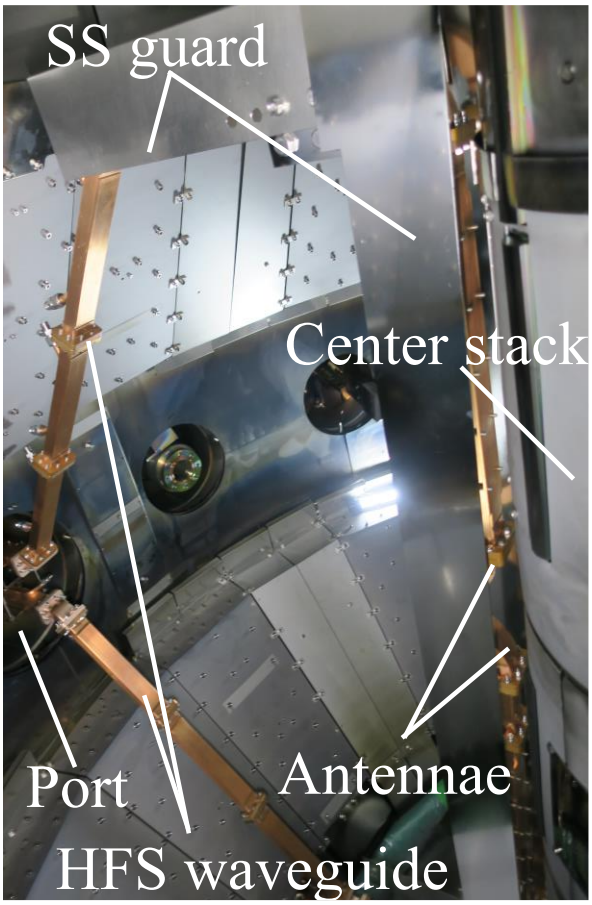

Fig. 29 HFS waveguide assembly in QUEST such that SS guard is the stainless steel guard, Port is where the flange connecting vacuum side and atmospheric side is, and Antennae are where the open-ended waveguide locations are (behind the SS guard).

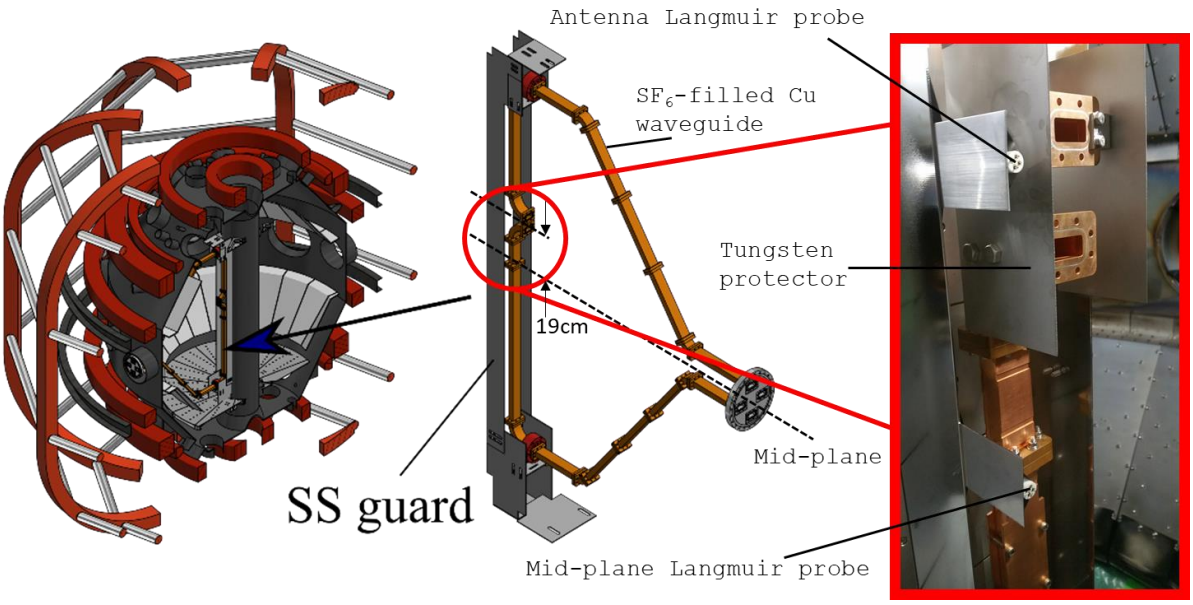

Fig. 30 Design of the waveguide antenna with the tungsten plate protector installed and two Langmuir probes installed (one at the antenna's vertical position and the other at the mid-plane's vertical position)

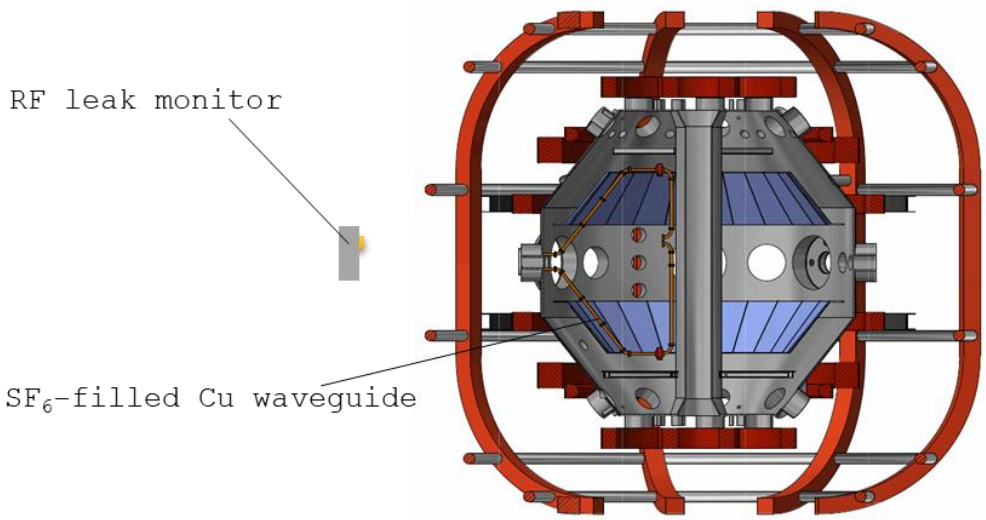

Fig. 31 HFS waveguide design in QUEST showing the location of the RF leak monitor outside of the vessel.

However, in previous LFS experiments in QUEST, the highest plasma currents were achieved at ECRL positions as far as R = 0.22 m and at closer ECRL radial locations (R = 0.4 m) lower plasma currents were experienced. This radial position, as a matter of fact, cannot be conducted within this experimental setup as the minimum allowable ECRL location is set at R = 0.35 m to avoid traversing the HFS antenna and cause breakdown. The third limitation to this setup is that given the short pulse duration, it is difficult to develop a large-enough plasma current to create a magnetic closed flux surface. Therefore, comparing the results of this setup to GENRAY's results is difficult as GENRAY only operates on closed flux surface results.

Moreover, to maximize the input power, an aging klystron (A2) was included in the RF injection system. A2 klystron can only inject LFS, however, it can be of use to test the hybrid system of both LFS and HFS even though A2 klystron does not have as much power as A4 and B1 klystrons. In addition, more PF coils were to be included in attempt to drive plasma current to higher than that of 2 kA. Another target was to try and investigate why plasma current starts dropping down after 3ms. In addition, the introduction of PF4, even though is counterintuitive as our target is non-inductive CD, would be useful to form a CFS to observe plasma behavior during.

4.2.1 RF leakage monitor measurement setup

To calculate how much the absorption percentage is for both LFS and HFS cases, a power dependency scan of the leakage was conducted. The calculation of the absorption can be conducted by following the equation

$$Leakage = P_{losses} * S \tag{4.2.1}$$

where $P_{losses} = P_{in} - P_{abs}$ is the lost power measured in watts, P_{in} is the input power measured in watts, P_{abs} is the absorbed power measured in watts, and S is the sensitivity of the sensor measured in V/W. It should be noted that the value of P_{losses} is assumed to contain the losses from the path loss from the RF source to the detector, wall absorption as the wall lies between the transmitter and detector, the line losses that connect the detector and the analog to digital converter, and the insertion loss from the device, such that the relation between the losses and the leakage is linear. To verify this assumption, a best fit line is shown in Fig. 32 that seems to lie within the error bar range. This is an inherent feature in the detector, which is why it can be

used as a RF power absorption monitor. In order to evaluate S, vacuum shots before plasma breakdown were considered as 100% lost power ($P_{losses} = P_{in}$). The sensitivity was then taken to be the slope of the best fit line as shown in Fig. 32 such that

$$S = 0.07 \pm 0.01 \left[\frac{V}{W}\right] \quad 4.2.2$$

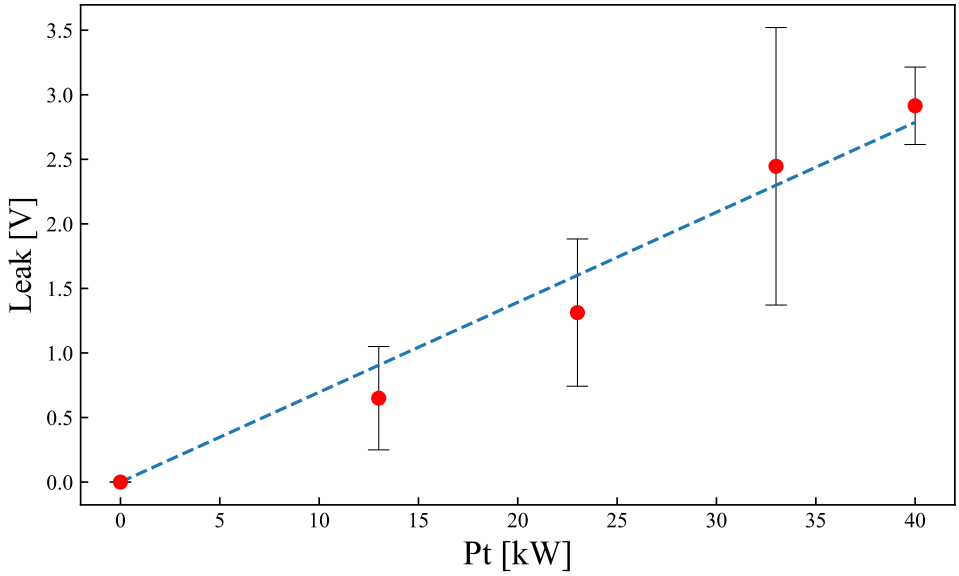

Fig. 32 Leakage vs total input power for different vacuum shots with different input powers

This would then give a leakage representation as follows

$$Leakage = mP_{in} \quad 4.2.3$$

where m is the slope of the leakage calculated in V/W. The percentage absorption is then to be calculated as follows

$$\%abs = \left(1 - \frac{m}{s}\right) * 100 \quad 4.2.4$$

4.2.2 Langmuir probe measurement setup

Langmuir probes have a variety of applications in the field of plasma measurements [80]. It can essentially acquire electron temperature and density measurements. The current-potential characteristics of the probe (shown in Fig. 33) allow for the measurement of the temperature and density where the temperature can be expressed as

$$T_e = \frac{e}{k}\left(\frac{d\left(ln(J_p + J_i)\right)}{d\varphi}\right)^{-1} \quad 4.2.5$$

where the current density of the probe J can be written as in the range of $\varphi < 0$ such that

$$J_p = J_{e0} exp\left(\frac{\varphi}{kT_e}\right) \quad 4.2.6$$

where φ is the negative floating potential. With the T_e expression available, the density can be expressed as

$$n_e = \frac{J_{e0}}{e}\sqrt{\frac{2\pi m_e}{kT_e}} \quad 4.2.7$$

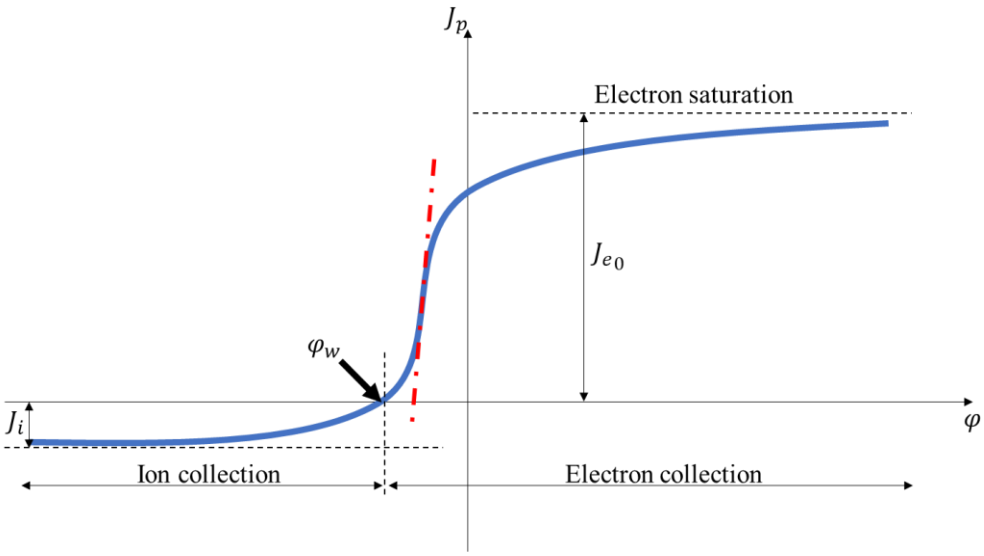

Fig. 33 Langmuir probe's characteristics of the current-potential curve, where the dotted red line represents the slope required for the calculation

The Langmuir probe design, as shown in Fig. 34 with the final product assembly shown in Fig. 35) is a four-pin design, such that we have one floating potential pin, one ion saturation current pin and two bias voltage pins.

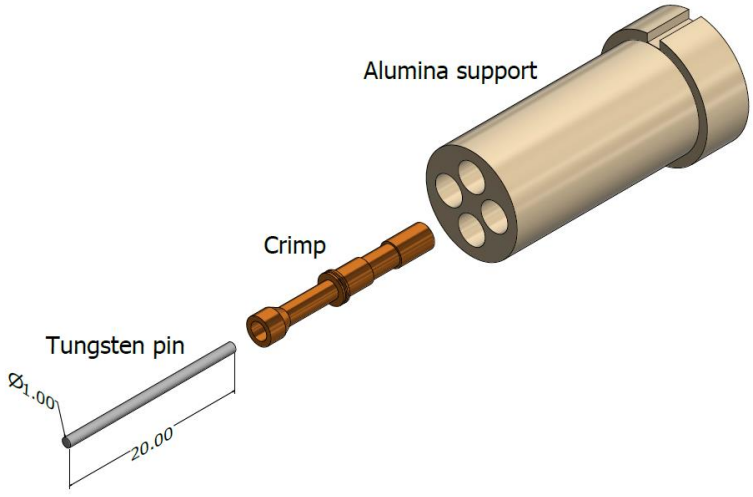

Fig. 34 Langmuir probe design showing the alumina support, one out of four crimps and one out

of four tungsten pins that have only 1.6mm exposed to plasma

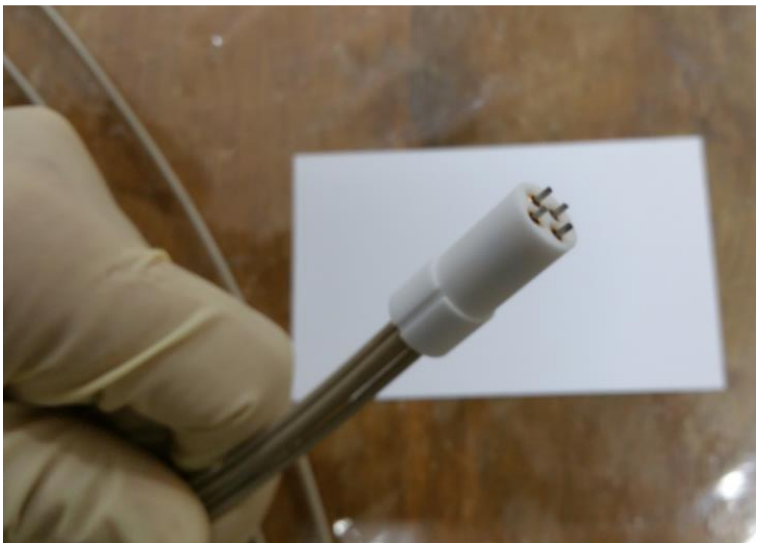

Fig. 35 Final assembly of the Langmuir probe

The probe pins are made of tungsten and are 1mm in diameter and the exposed tip is 1.6mm in length. The crimp is made of gold and the supporting body is made of alumina. The crimps are connected to the pin from one end, and to peek cables from the other. The entire structure is spot-welded into the inner side of the stainless steel guard with the cables covered by sheet steel to protect them from the high-temperature plasma. The peek cables are coaxial and the outer mesh is separately connected to a crimp and is grounded. A total of 8 probe pins gives a total of 16 peek cables that are connected to the 30-pin peek support from the other side, then connected to a flange. The atmospheric side of the flange is connected to BNC cables that are directly connected to the Langmuir probe circuit shown in Fig. 36.

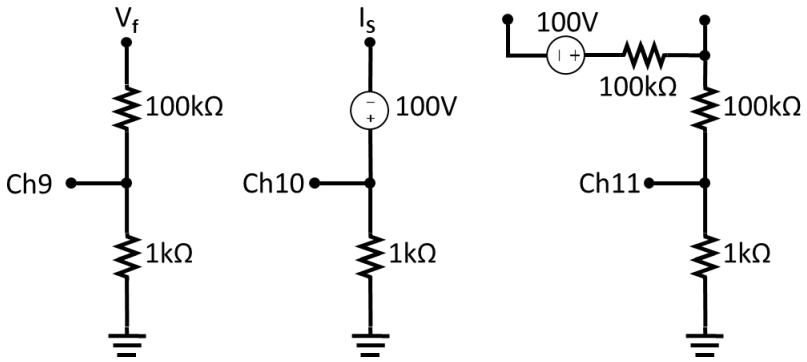

Fig. 36 Connecting circuit for the Langmuir probe such that V_f is the floating voltage, I_s the ion saturation current and Ch is the oscilloscope's connecting channel

The Langmuir probe data acquisition equations are as follows:

$$V_f\ [V] = 101 * Ch9\ [V] \tag{4.2.8}$$

$$I_S\ [A] = \frac{Ch10\ [V]}{1k\Omega} \tag{4.2.9}$$

$$T_e\ [eV] = \frac{Ch11\ [V] * 101 - V_f\ [V]}{\ln(2)} \quad 4.2.10$$

$$n_e[m^{-3}] = I_S.\exp\left(\frac{1}{2}\right)\frac{\sqrt{m_i}}{S_p.e.\sqrt{T_e e}} \quad 4.2.11$$

such that Ch9, Ch10, and Ch11 are the oscilloscope channels, T_e is the electron temperature in eV, n_e is the electron density in m^{-3}, and S_p is the exposed surface area of the pin, calculated as:

$$S_p = \pi r^2 + 2\pi r l \quad 4.2.12$$

where r is the pin radius (1mm) and l is the exposed pin length (1.6mm).

4.2.3 Sideband measurement setup

In addition, for confirming EBW mode conversion, EBW's parametric decay instability (PDI) is to be measured. The sideband is about 100 MHz before the 8.2 GHz band (8.1 GHz), so a high-bandwidth spectrum analyzer is required to measure it. Essentially, there are two connections of the spectrum analyzer (see Fig. 37):

A) connecting it to an unused LFS antenna and running LFS or HFS injection
B) connecting it to one of the HFS antennas and use it as a detector and operate at half of the HFS system power
C) connecting it to one of the HFS antennas and operate the LFS injection system at full capacity.

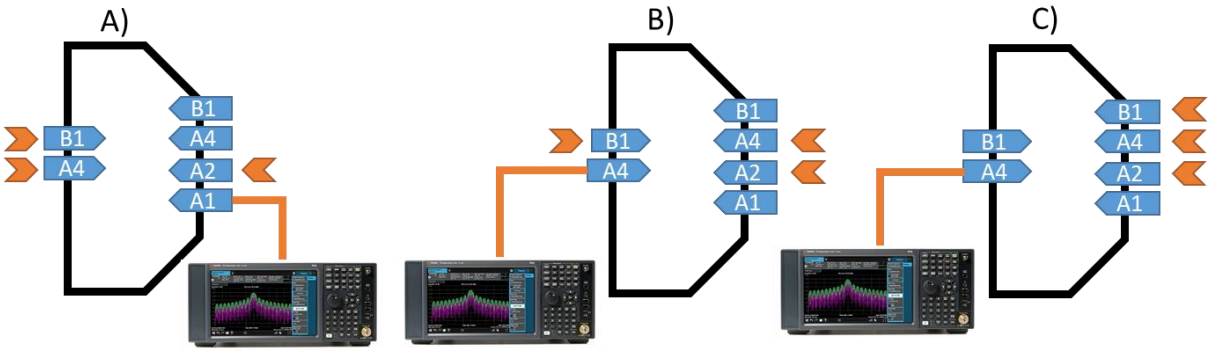

Fig. 37 Different spectrum analyzer connecting schemes such that A) has the spectrum analyzer connected to the LFS waveguide, which would allow for both LFS and HFS injections as non-used LFS waveguides are available, B) spectrum analuzer is connected to the HFS lower antenna, allowing for only half of the HFS injection power to be injected, and C) spectrum analyzer is connected to the HFS lower antenna with 100% of the LFS system operating.

Moreover, as shown in Fig. 38 a lower hybrid wave (LHW) will also exist [57] (at 100 MHz in our case), which is also useful to confirm, but as this wave has a low frequency, measuring it using an antenna would require the antenna to be oversized.

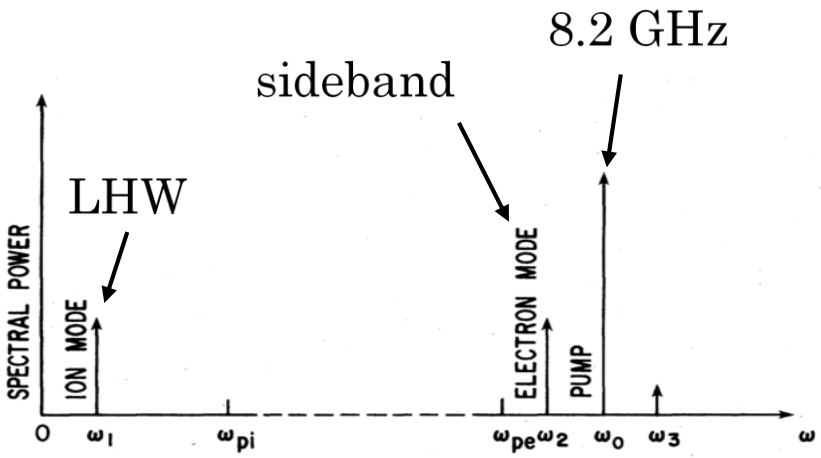

Fig. 38 Full spectrum of PDI where ω_1 is the lower hybrid angular frequency, ω_2 is the sideband frequency and ω_0 is the central frequency (8.2 GHz in this work) (from ref. [57]*)*

However, one of the Langmuir probes can have its ground pin disconnected so that it would act as an insertion antenna. This was applied to the mid-plane Langmuir probe. The antenna Langmuir probe had its ground disconnected, and its pin connected to a 350 MHz oscilloscope (see Fig. 39), which would capture its time evolution, that is to be later converted to spectrum using Fast Fourier Transform (FFT).

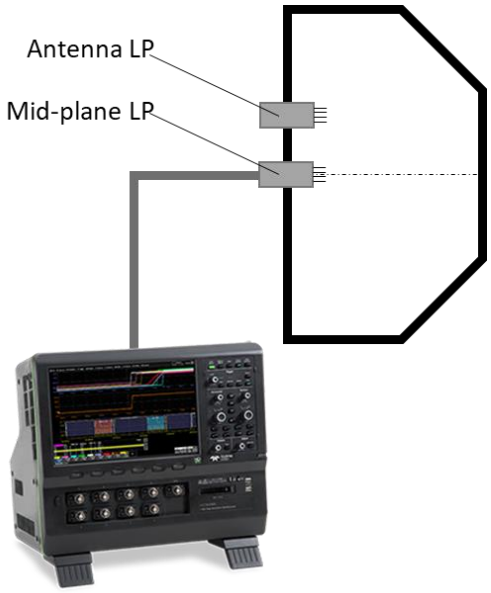

Fig. 39 The grounded pins of the antenna probe were removed, and its connection to the oscilloscope was replaced with the 350 MHz oscilloscope to try and measure the lower hybrid wave (LHW)

5. Results and discussion

This section discusses the experiment of HFS injection of X-mode in QUEST. It contains the experimental procedure as well as the results. The experiment was conducted within an RF shot pulse duration of 10 ms to prevent the RF system from overheating. Baking to improve the vacuum condition was also conducted at 80℃ instead of the usual 100℃ with a gradient of 5℃/hour to avoid rapid thermal expansion of the waveguides that might degrade the vacuum condition.

Typical waveform explanation is to be presented at first.

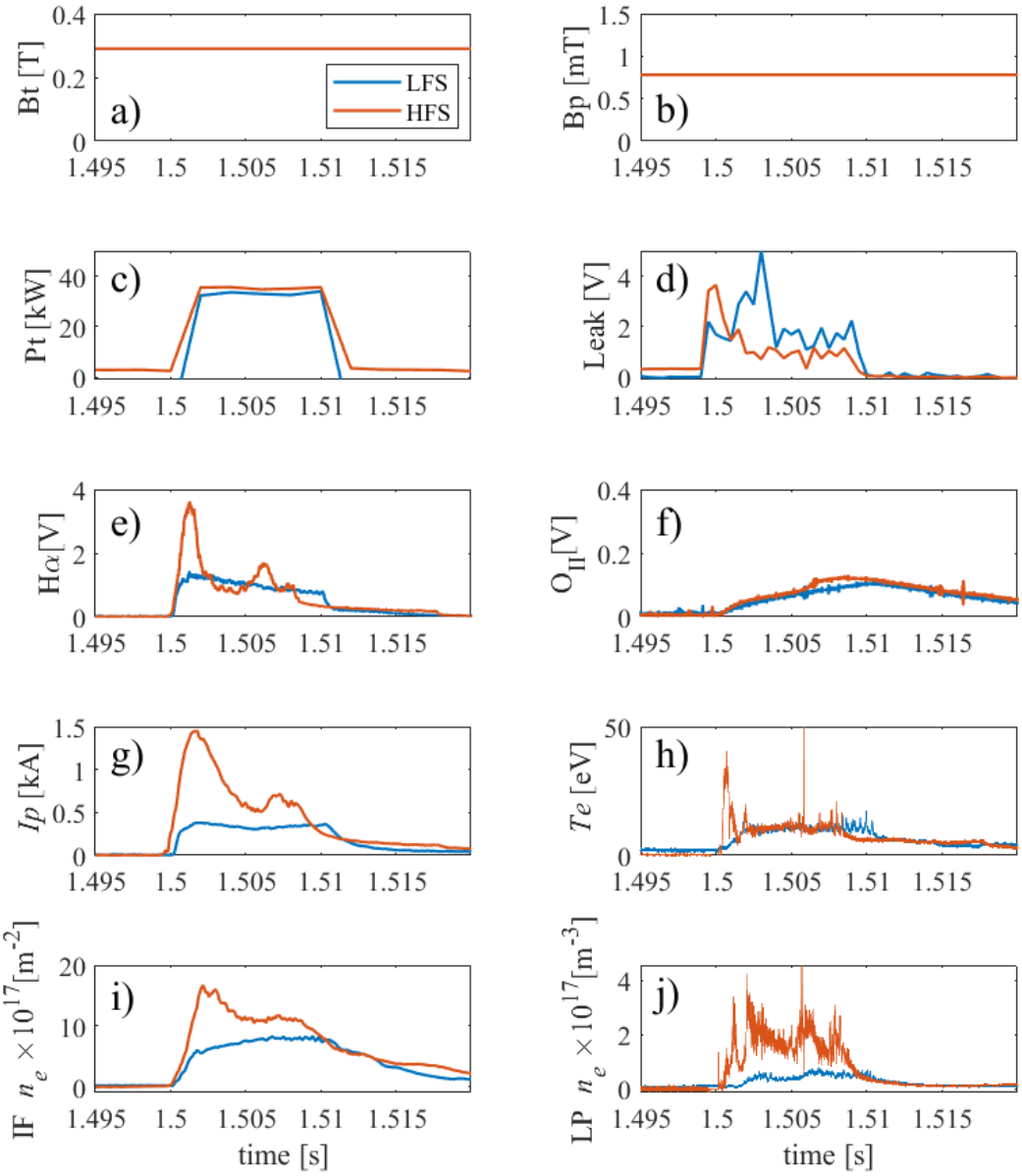

Fig. 40 A typical waveform of the different plasma control parameters and diagnostics for a single shot for both LFS and HFS such that a) is the toroidal field, b) is the poloidal field (PF2-6), c) is the total klystron power, d) is the leakage from RF monitor, e) is the Hα sensor, f) is the oxygen sensor, g) is the plasma current, h) is the electron temperature, i) is the interferometer's line-integrated electron density and j) is the Langmuir probe's local electron density (at the antenna position Z=19cm)

Fig. 40 represents a typical LFS vs HFS comparison where Bt represents the toroidal field measured at the ECRL position, Bp represents the poloidal field measured at the ECRL position and the mid-plane and Pt is the total input RF power. In this work, the RF duration determines the shot duration, which in this case is 10ms. It can be noticed from Fig. 40 that in a typical shot, Bt, Bp and Pt are all constant in time, which is why their time evolution will not be included later on. The reason why Pt for HFS is lower is because only two klystrons are connected to the HFS, whereas three klystrons are connected to the LFS. Bt is used to control the ECRL position such that increasing the toroidal coil current moves the ECRL towards the LFS and vice versa. Bp is used to control the plasma shape and size as well as help drive plasma current. Typically, HFS has higher plasma current than LFS, but HFS's plasma current is unstable. Leak is the RF monitor mentioned in section 4.2.1. This monitor measures the RF leakage losses in volts, which is proportional to the RF power absorption as shall be discussed later in this section. Typically, HFS leak is much lower than that of LFS, however, before plasma breakdown, HFS leak is higher. Both Hα and O_{II} monitors are line radiation sensors that measure Hα and O_{II} in volts respectively. Hα indicates how much plasma radiation is emitted, in which case the HFS injection system is much higher than that of LFS. O_{II} indicates how much impurities are outgassed from the wall due to the plasma-wall interaction. Both HFS and LFS have high O_{II} emission, which indicates the necessity of conducting discharge cleaning for improving the vessel vacuum conditions. Ip is the plasma current measured in kA via the Rogowski coil. Te is the Langmuir probe's electron temperature measured in eV, where the Langmuir probe location and setup are discussed in section 4.2.1. There are two methods of measuring plasma density in this work; the interferometer and the Langmuir probe. IF n_e and LP n_e are the interferometer density and Langmuir probe densities respectively.

5.1 HFS and LFS injections in toroidal field presence only

The purpose of this section is to prove that EBW mode was excited using the HFS injection system, and the mode conversion efficiency of the HFS injection system is higher than that of the LFS injection system. A test at the maximum toroidal field B_{TF} = 0.29 T and at injected RF power of P_T = 33 kW was conducted to compare between HFS and LFS as shown in Fig. 41 a) and b). At the value of B_{TF} = 0.29 T, plasma current peaked at I_P = 130 A for the HFS injection and 35 A for the LFS one.

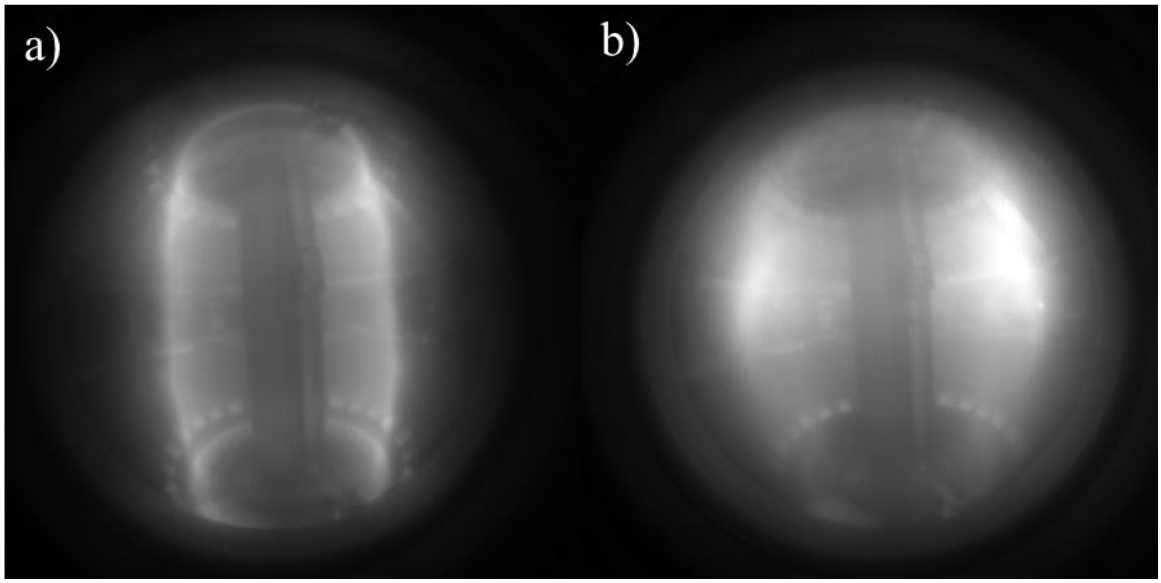

Fig. 41 Camera image for toroidal field current of R_{ECRL}=0.55m for (a) LFS and (b) HFS at 33 kW of injected 8.2 GHz RF power.

Given the obscurity of EBW mode, various attempts at confirming its excitation were conducted. The identifying methods used here were UHRL position identification and RF leakage Expected is for the HFS injection system to have more prominent evidence of EBW conversion, which indicates its higher conversion efficiency, compared to that of the LFS injection system.

To confirm EBW conversion, plasma density is used. An interferometer placed at the mid-plane measures the line-averaged density, which is then compared to plasma density based on the camera image (shown in Fig. 41). If the position of UHR as assumed to be at the maximum brightness point of the plasma, this will confirm EBW conversion and will enable the calculation of plasma density such that

$$R_{UHR} = \left(\frac{{\omega_{RF}}^2}{{\omega_{RF}}^2 - {\omega_{pe}}^2}\right)^{\frac{1}{2}} R_{ECRL} \qquad 5.1.1$$

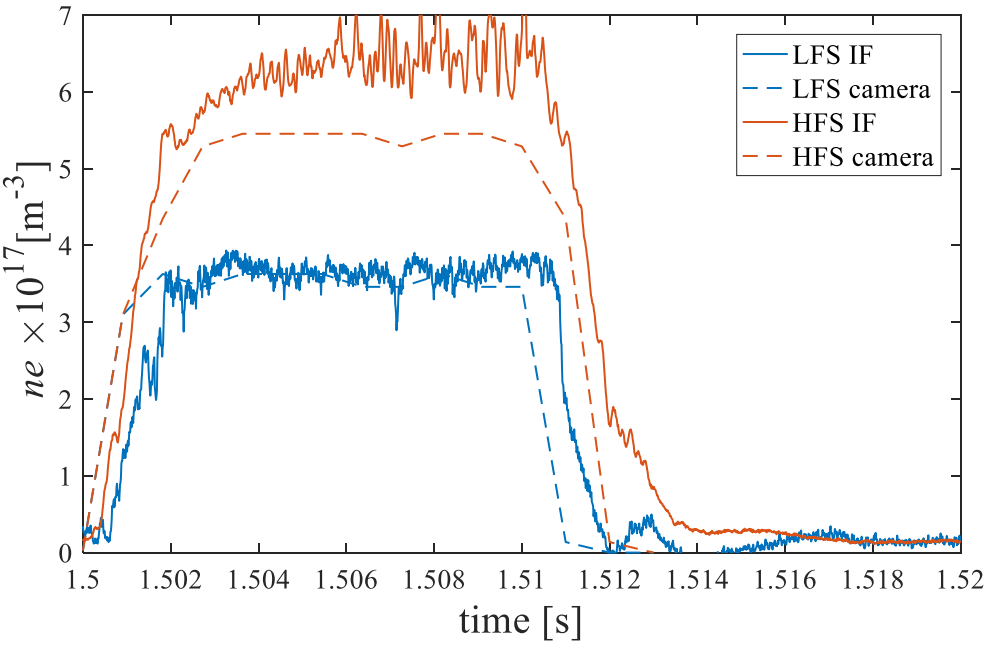

Fig. 42 Comparison between interferometer (IF) density and plasma edge (camera) density calculation for HFS and LFS

As shown in Fig. 42, interferometer signal strongly agrees with plasma edge density calculated from fast camera image which confirms that the maximum brightness point of the camera image is the UHR, therefore confirming EBW conversion.

In the case of HFS injection, Langmuir probe showed an electron temperature of 4.2 eV whereas in the LFS injection, it showed an electron temperature of 2.67 eV, as shown in Fig. 43.

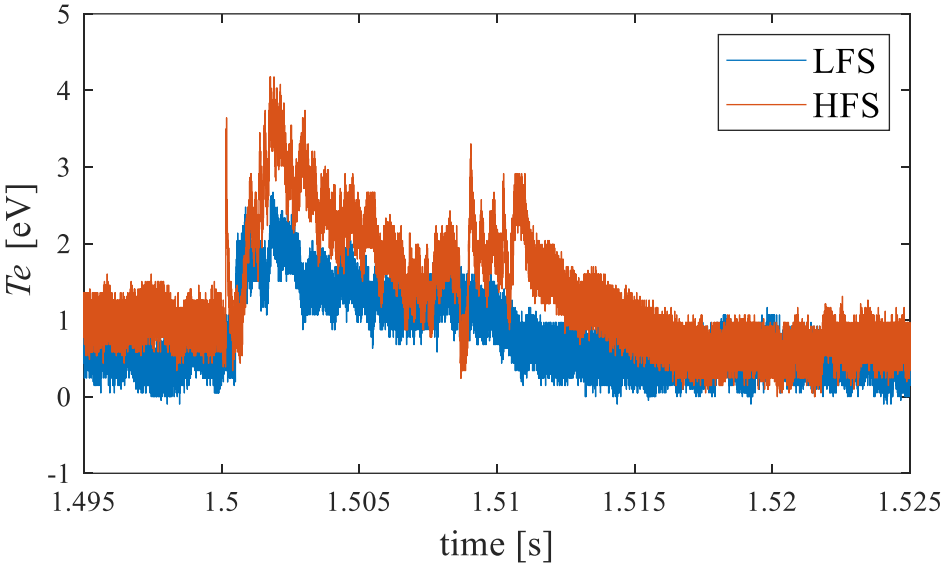

Fig. 43 Langmuir Probe's electron temperature for HFS and LFS where R_{ECRL} = 0.55m, P_t = 33 kW and no poloidal field

This might be another indicator that HFS injection has higher EBW conversion efficiency than that of the LFS, but it is difficult to conclude as the Langmuir probe only measures the plasma edge density, which in this case might indicate loss of plasma temperature from the plasma core to the edge. To verify that HFS injection has higher electron temperature, a radial profile of the temperature is required, which can be achieved via the movable probe as shall be discussed in section 7.

Nonetheless, a method of confirming EBW is the absorption efficiency. High efficiency EBW conversion would lead to efficient power absorption of the RF wave and therefore low RF leakage. To confirm, RF leakage monitors installed outside QUEST vessel as shown in Fig. 31 were used to verify the leakage of LFS and HFS. The leakage results, as shown in Fig. 44, indicate that HFS injection made a better ERF absorption than LFS one and it is consistent with the efficient EBW conversion.

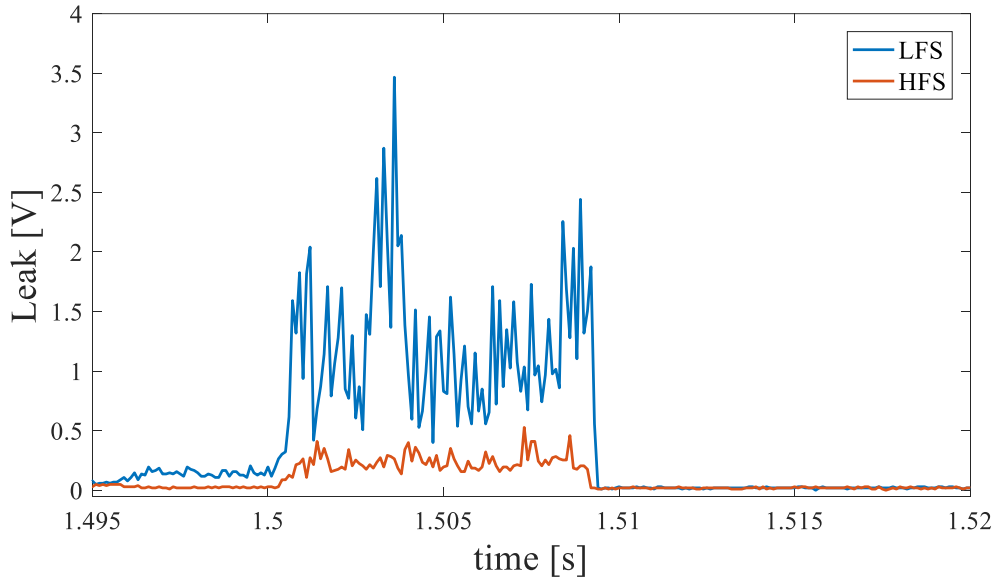

Fig. 44 Comparison between HFS and LFS in terms of time evolution of leakage power

Fig. 45 shows the leakage for plasma shots of different Pt for HFS and LFS, where the slopes can be calculated as shown in the best fit representations. The absorption for the HFS case would then be calculated to be 96% as opposed to 40% for the LFS case. This shows that the higher power injection makes a higher temperature plasma and enhances RF absorption. This is the characteristics of fundamental ECR absorption as described in [73]. In the LFS injection case, significant RF power may come around HFS and the RF absorption at fundamental ECR may work well, although the consideration is just speculation. Whatever the case, the RF absorption in the case of HFS injection shows that it is superior to that of the LFS injection.

One issue with this method is the fact that the HFS antenna is much closer to the resonance layer as show in Fig. 46, therefore it can be assumed that HFS injection has a lower chance of diffraction compared to LFS injection, and therefore a lower chance of leakage, making this comparison seem questionable. However, considering Fig. 47, the toroidal field was moved closer to the LFS antenna (higher toroidal field current) with no signs of improving RF power absorption. Therefore, it is safe to conclude that HFS injection has a better absorption that LFS even with the asymmetric antenna distribution accounted for.

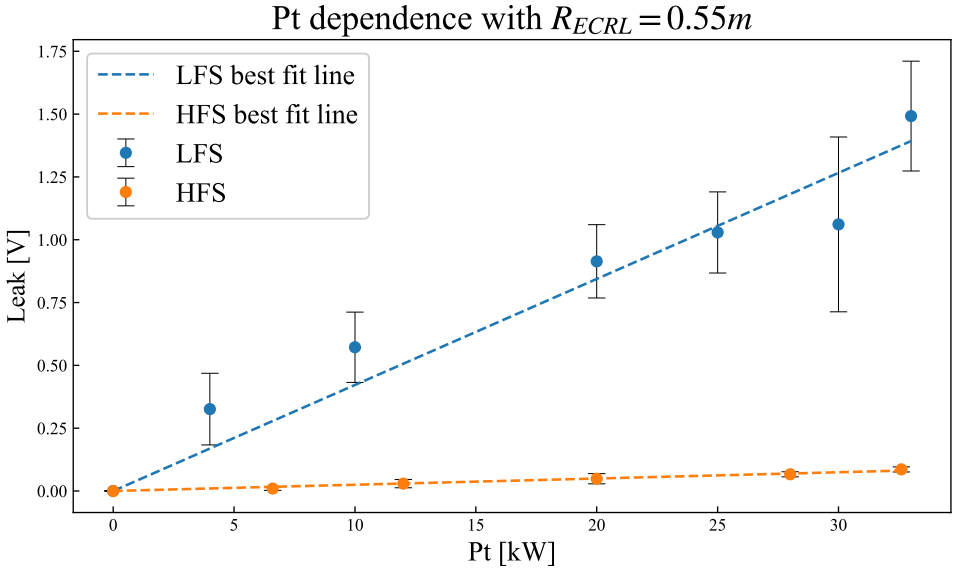

Fig. 45 Power dependency of the leakage for HFS and LFS during plasma discharges where the dashed lines are the best fit lines for both HFS and LFS cases.

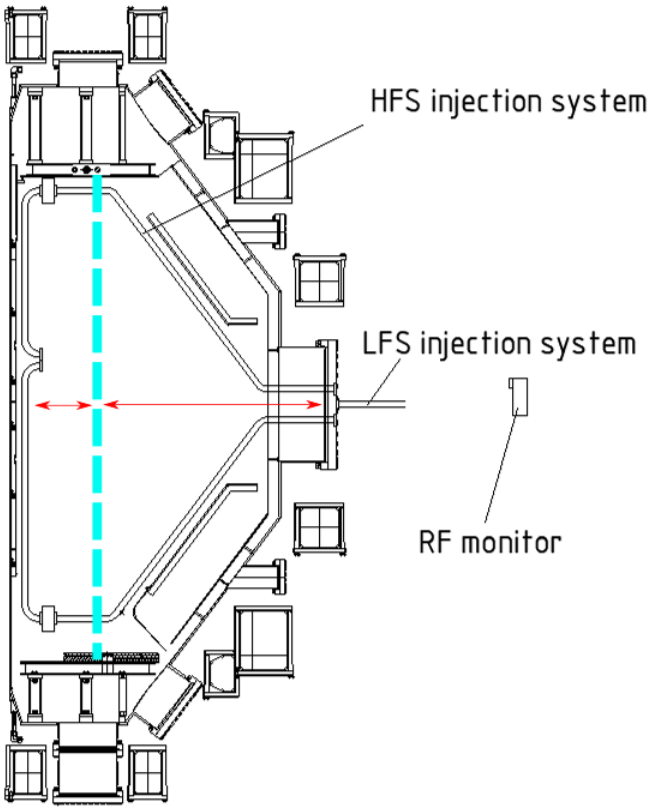

Fig. 46 The red arrows show the distance between the injection systems and the ECRL (dashed cyan line)

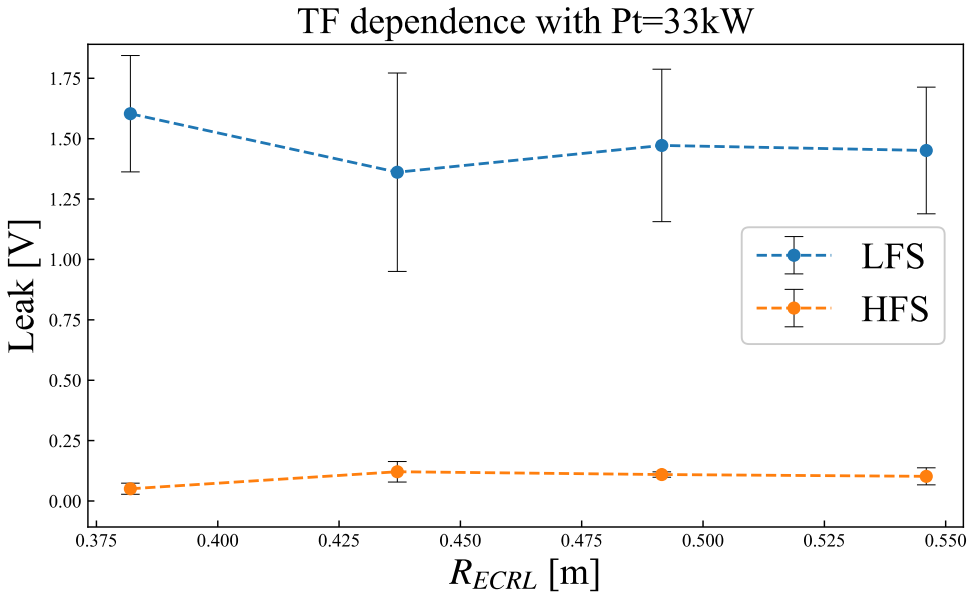

Fig. 47 Leakage for HFs and LFS by changing the toroidal field current, which would then change the position of the ECRL (R_{ECRL})

5.2 HFS and LFS injections in toroidal and poloidal field presence

The introduction of the poloidal field has two purposes: to attempt to achieve magnetic equilibrium for tokamak configuration, and to attempt to drive EBWCD. Sideband measurement was conducted after the poloidal field was installed to further verify EBW excitation.
Introducing poloidal field and scanning B_{PF}, B_{TF} for monitoring I_P was conducted. The aim of this scan was to maximize I_P in order to test whether EBWCD is achievable. Maximum HFS plasma current of I_P=1.4 kA was achieved at $B_{PF2\text{-}6}$=0.78 mT, R_{ECRL}=0.44 m, GP=24ms and total RF power of 33 kW in the case of HFS injection and 0.5 kA at $B_{PF2\text{-}6}$=0.78 mT, R_{ECRL}=0.44 m, GP=24ms and 33 kW in the case of LFS one. Note that the toroidal and poloidal fields are measured horizontally at the ECRL position and vertically at the mid-plane.
Optimizing the magnetic parameters and the gas puff for maximizing the Ip was done through four steps: 1- Optimize the PF2-6 coil at R_{ECRL}=0.55m (as Fig. 47 suggests 0.55m is optimal), 2- Optimize the ECRL position at the optimal PF2-6 position, 3- Re-optimize the PF2-6 coil at the optimal R_{ECRL}, 4- Optimize the gas puff duration.

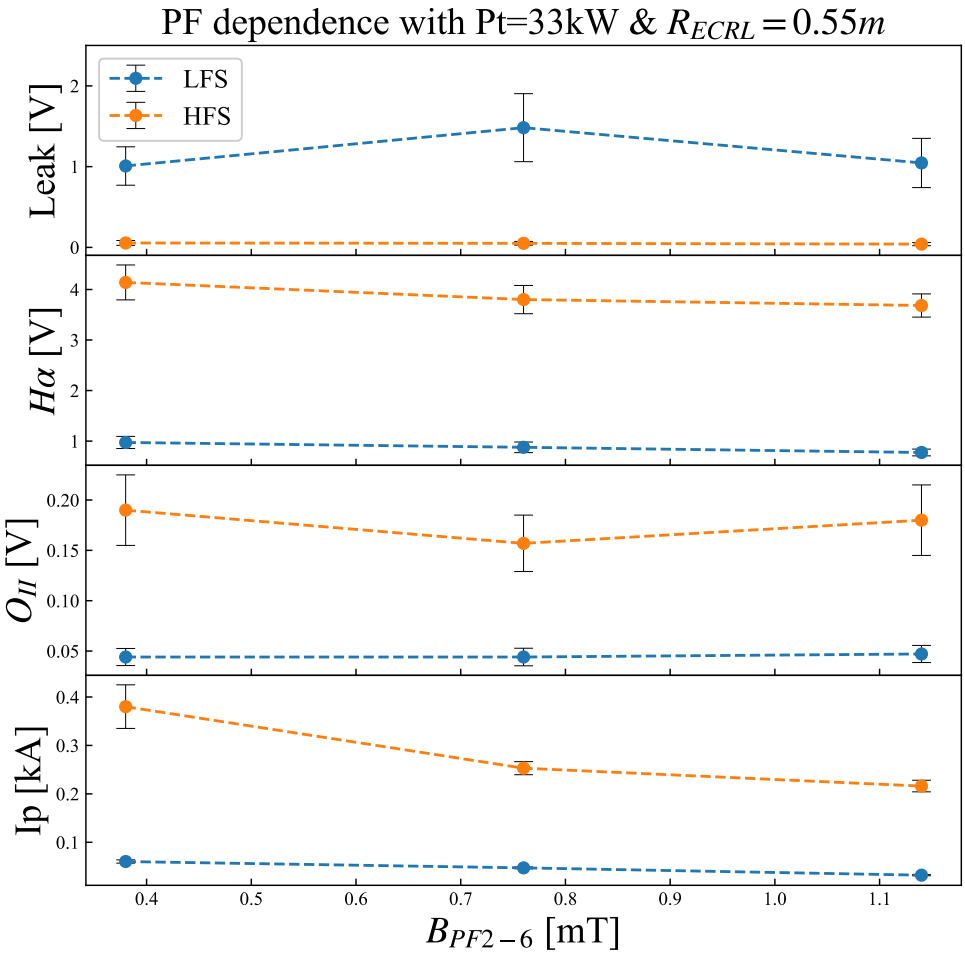

Fig. 48 Poloidal field dependence at total klystron power and ECRL position of R_{ECRL}=0.55m. Both Hα and O_{II} show $B_{PF2\text{-}6}$ dependency, however, it is not so significant and while Ip show's a significant dependence. It shall be noted that even though it is clear that smaller values of $B_{PF2\text{-}6}$ result in higher Ip, we shall stop at 0.38mT as the results will be affected once the other steps are conducted.

The maximum plasma current, as shown in Fig. 48 (step 1) was obtained at $B_{PF2\text{-}6}$=0.38mT at R_{ECRL}=0.55m and gas puff GP =40ms. Further optimization of R_{ECRL} showed that the maximum

plasma current was obtained at R_{ECRL}=0.44m and GP =40ms as shown in Fig. 49 (step 2). B_{PF2-6} was optimized once more at the new R_{ECRL} position and GP =40ms, showing a maximum plasma current at B_{PF2-6}=0.78mT as shown in Fig. 50 (step 3). Finally, the gas puff was optimized at the aforementioned parameters, giving a maximum plasma current at GP=24ms as shown in Fig. 51 (step 4).

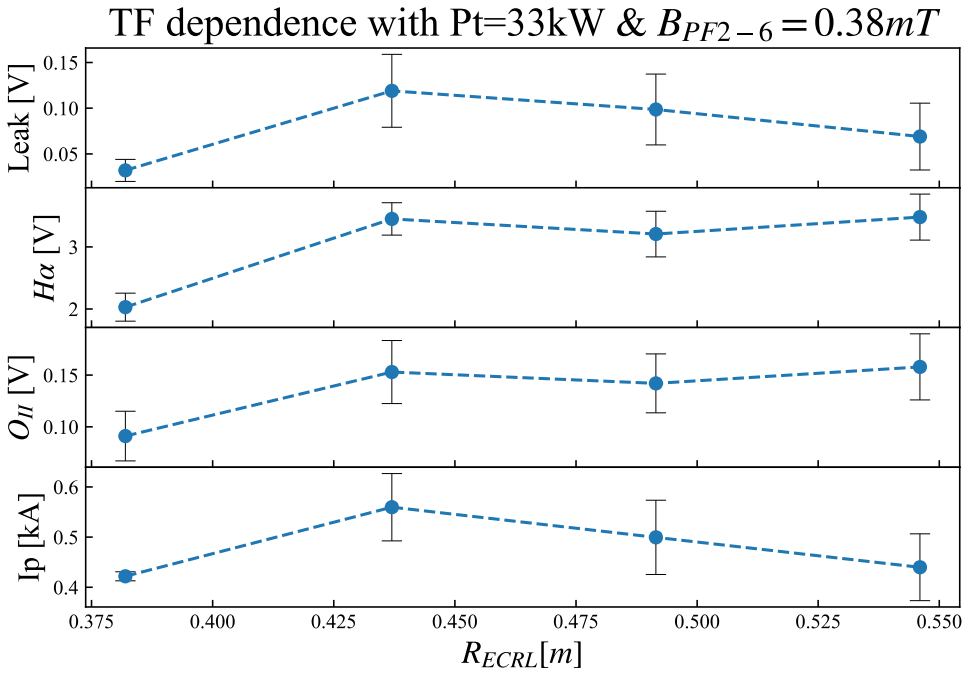

Fig. 49 Toroidal field (TF) dependence at total klystron power and B_{PF2-6}=0.38mT. Leak does not show any significant dependency on the toroidal field strength, while Hα and O_{II} show a positive tendency towards higher toroidal field strength. However, Ip, the most important factor in this scan, shows an optimum position around R_{ECRL}=0.44m

In Fig. 49, even though there seems to be a significant dependence of Leak on toroidal field strength, however, the highest amount of Leak still leads to very small losses and the majority of the RF power will be absorbed, so the Leakage tendency is to be ignored. Both Hα and O_{II} seem to get higher with increasing the toroidal field strength, however, from R_{ECRL}=0.44m onwards, the tendencies do not seem to be significant. Nonetheless, Ip seems to depend on the TF scan significantly, peaking at R_{ECRL}=0.44m, so that value is taken as a reference for the next scan. However, in the case of step 3 (Fig. 50), re-optimizing the PF strength seems to have some impact on the Leak. Even though percentage absorption decreased from 94% to 85%, the plasma current improved from 0.4kA to 0.56kA. Moreover, Hα and O_{II} are both decreasing, which is an indicator that the vessel condition is slightly improving during the scan, which is a partial reason for why the plasma current has increased as the impurities act as a resistance to the plasma current. Moreover, as the O_{II} impurities partially absorb RF power, their reduction suggests why the percentage absorption increased. Fig. 51 shows the gas puff dependence by controlling the duration of the injected hydrogen gas. It can be noticed that Hα and O_{II} are in continual decline with decreasing the gas puff giving plasma current a chance to peak at 0.8 kA.

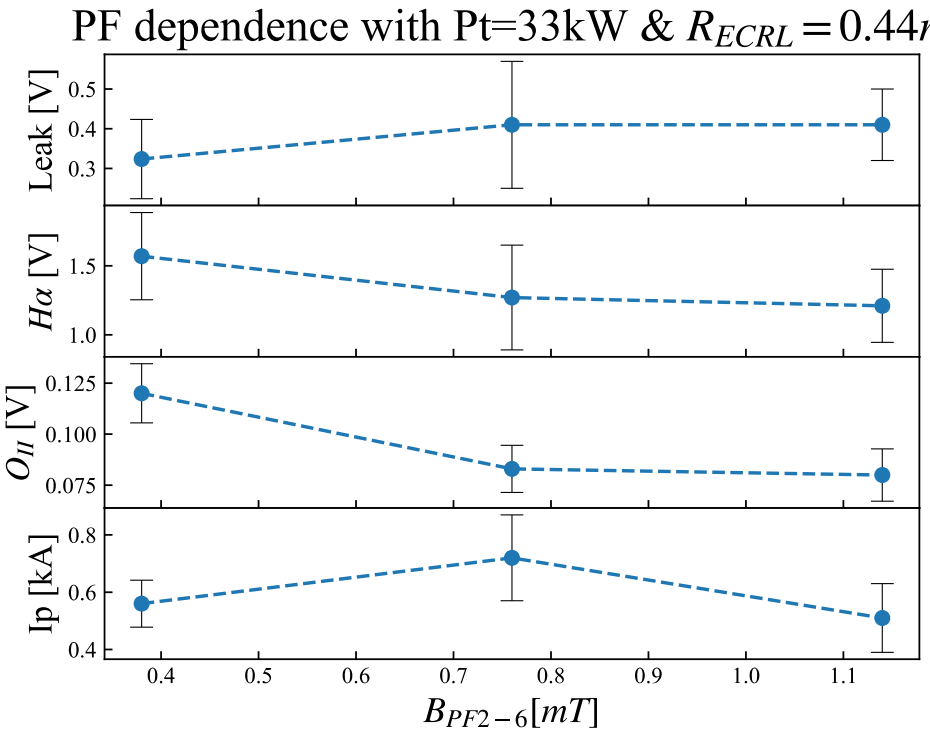

Fig. 50 Poloidal field dependence at total klystron power and ECRL position of R_{ECRL}=0.44m. Ip, in this test as well, showed a tendency towards an optimum B_{PF2-6} that does not agree with Hα and O_{II}, nonetheless, as mentioned previously, Ip is of highest priority. Leak does not show any dependency.

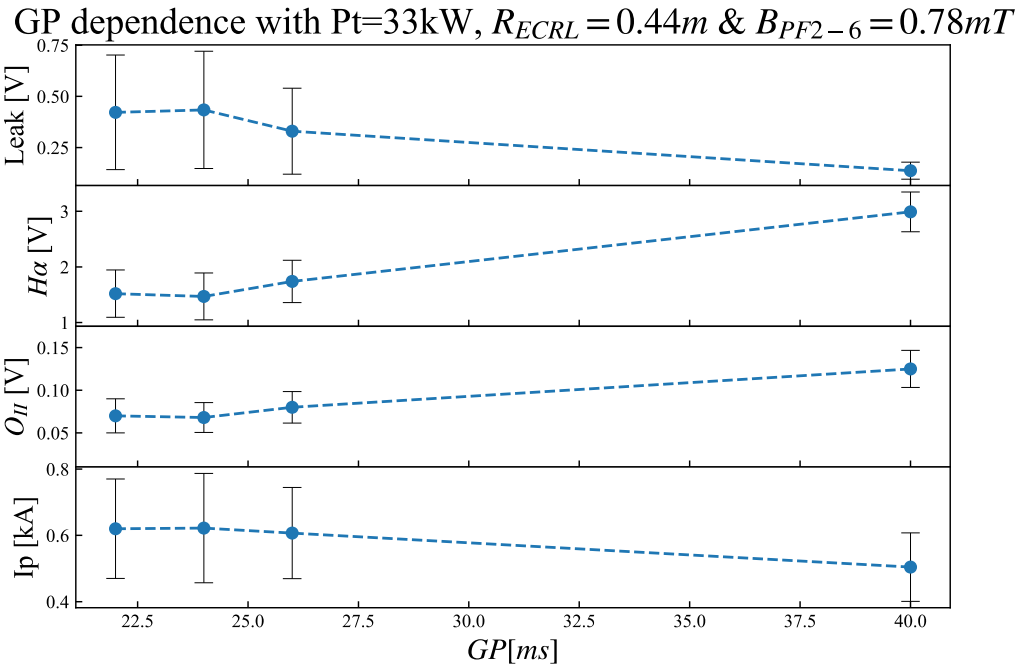

Fig. 51 Gas puff dependence at total klystron power, R_{ECRL}=0.44m and B_{PF2-6}=0.78mT

Furthermore, the horizontal field coils (HCUL) were used to try and lower the equilibrium point of the magnetic field as the plasma is asymmetric due to the vertical displacement of the antennas,

however, the effect of the HCUL was insignificant as shown in Fig. 52. This shows that plasma current is not centralized but rather spread, which indicates a difficulty in forming a CFS.

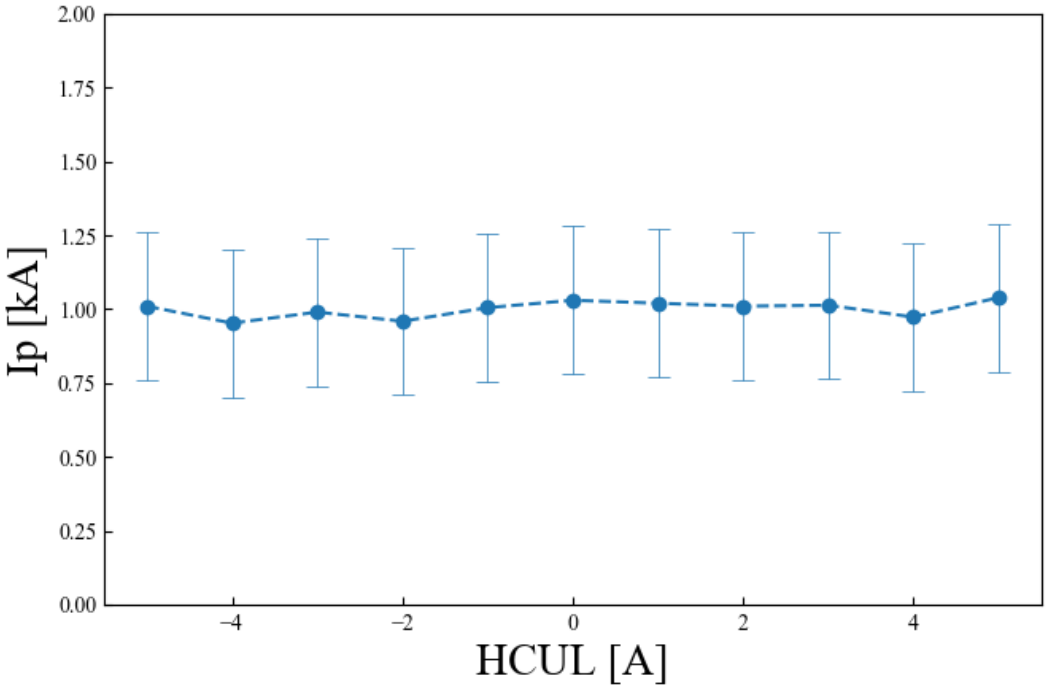

Fig. 52 HCUL dependency of Ip for the HFS case

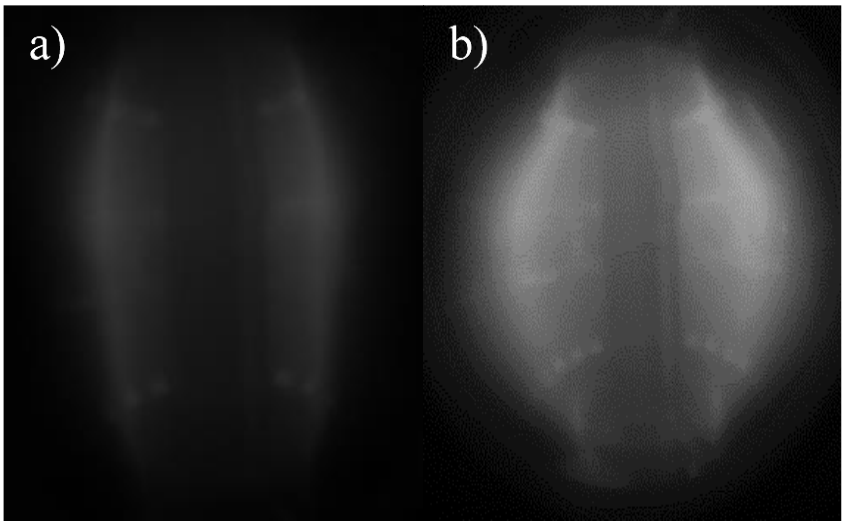

Fig. 53 Fast camera image comparison between a) LFS and b) HFS for R_{ECRL}=0.44m, $B_{PF2\text{-}6}$=0.78mT and GP=24ms

The camera image shown in Fig. 53 can clearly show where the brightest point is, and how it bends outwards in time. This is more useful for analyzing the interferometer data as well as locate the UHRL position.

Diagnostic results for HFS are shown in Fig. 54 while LFS are shown in Fig. 55. Both Te and n_e are measured by the Langmuir probe, positioned at the mid-plane.

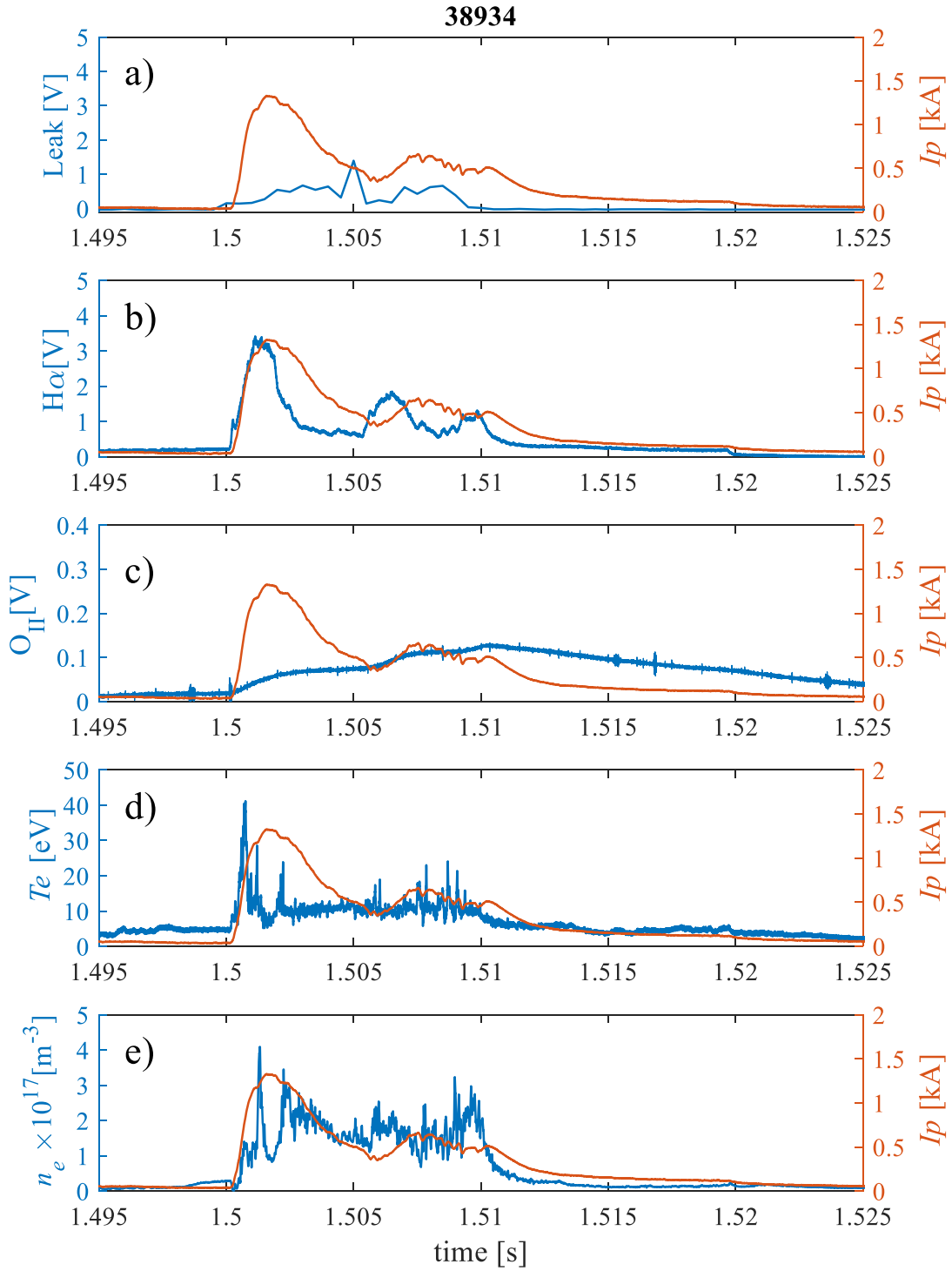

Fig. 54 Shot number 38934: 10ms HFS injection at $B_{PF2\text{-}6}$=0.78 mT, R_{ECRL}=0.44 m, GP=24ms such that a) is leakage monitor measured in volts, b) Hα radiation sensor measured in volts, c) oxygen sensor measured in volts, d) Langmuir probe's electron temperature measured in eV (at Z=19cm) and e) Langmuir probe's electron density measured in m^{-3} (at Z=19cm). The right y-axis in all those figures show plasma current measured in kA.

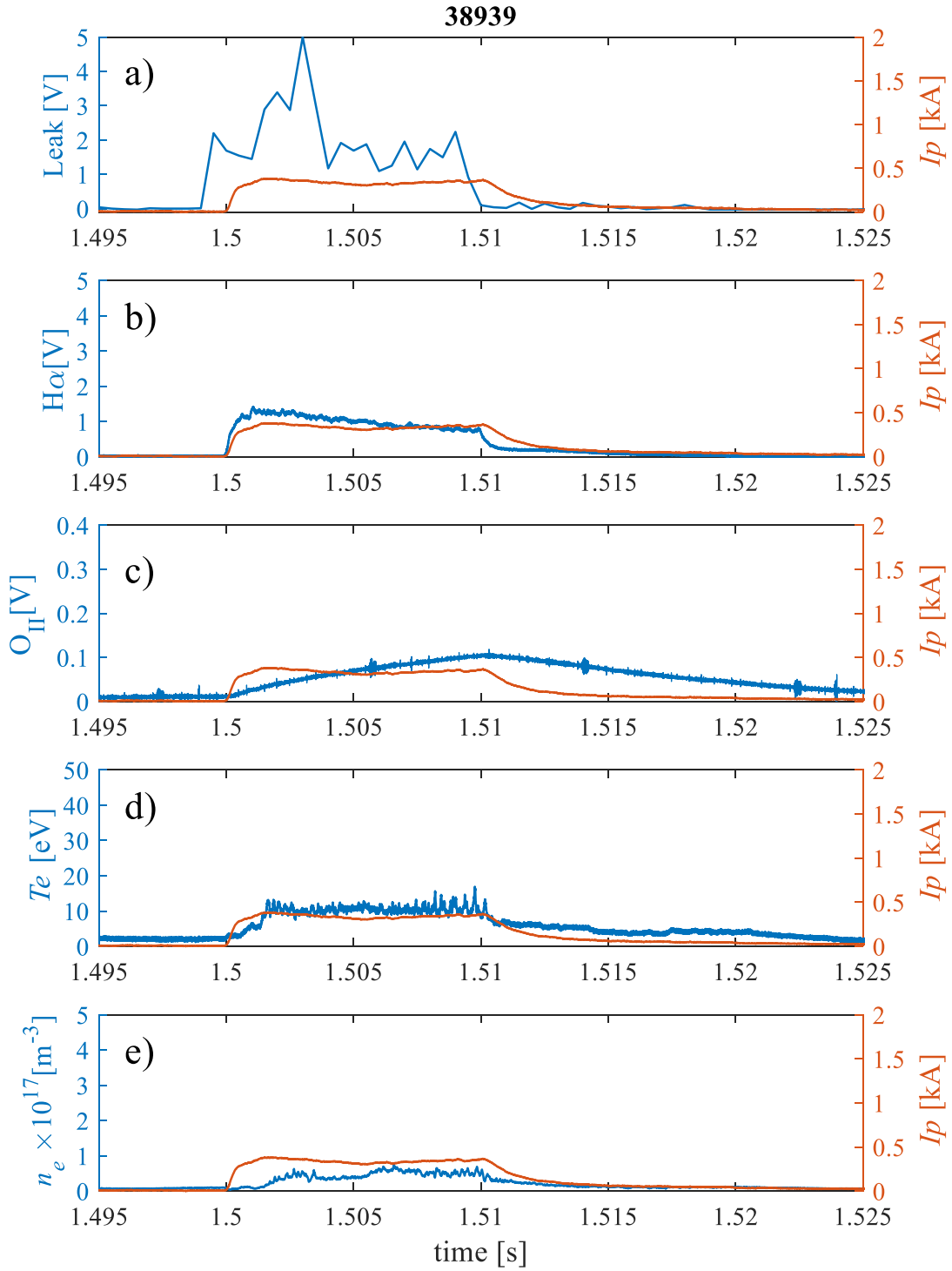

Fig. 55 Shot number 38939: 10ms LFS injection at $B_{PF2\text{-}6}$=0.78mT, R_{ECRL}=0.44m, GP=24ms such that a) is leakage monitor measured in volts, b) Hα radiation sensor measured in volts, c) oxygen sensor measured in volts, d) Langmuir probe's electron temperature measured in eV (at Z=19cm) and e) Langmuir probe's electron density measured in m^{-3} (at Z=19cm). The right y-axis in all those figures show plasma current measured in kA.

The sharp rise of Leak at the beginning of Fig. 54 is because breakdown has not occurred yet at that time. Hα's drop after its rise is due to the plasma getting colder, which can also be verified by LP Te. The huge rise in O_{II} indicates the large amount of impurity, which exists due to lack of discharge cleaning, but can also be an indicator of how effective HFS is in creating plasma that interacts with the wall. LP n_e starts decreasing when the plasma current is at maximum. The increase in Ip is correlated with the increase in Hα and Te, which indicates that at some time 1.503s, the plasma started to cool down. In addition, the timing of the peak plasma current coincides with the valley that is observed in the LP n_e. This indicates that not only does plasma temperature decreases at 1.503, but also it shrinks in size, hence the lower density. On the other hand, LFS injection (shown in Fig. 55) shows that plasma current in the case of HFS is much higher than that of the LFS. Furthermore, Hα in the case of HFS is much higher than that of the LFS. This indicates that the plasma density as well as temperature in the case of HFS are much higher than the LFS. This can then be confirmed by checking the plasma temperature and density of the Langmuir probe, which indeed suggests that HFS plasma is hotter and denser than its counterpart. Not to mention, plasma current and Hα in the LFS case are very stable and do not experience the fluctuations found in the HFS case. To further explore this problem, a longer shot duration is required. The vacuum window might experience some stress from the thermal deposition associated with the longer pulse durations, which is why the longer pulse duration will not exceed 100ms. The 100ms shots were conducted for HFS and LFS cases , and the results are shown in Fig. 56 and Fig. 57. As shown in Fig. 56 and Fig. 57, the comparison between HFS and LFS became more meaningful. It can be observed from the graphs that HFS has superior Leak compared to LFS, even for extended durations. In addition, it can be clear that both Ip and Hα are fluctuating in the HFS case, while completely stable in the LFS one. Furthermore, even though in the case of 10ms, O_{II} was almost the same in HFs and LFS discharges, the 100ms discharge reveals that HFS O_{II} is much higher than that of LFS. Nonetheless, the O_{II} level seems to saturate after 50ms. This indicates that O_{II} measurement system has an integration circuit that has a very limited time response, rendering this system partially flawed for our shot pulse duration limit. Noteworthy to mention, is the fact that HFS injection experiences a very large Ip in the first 5ms, while after that it regresses to become slightly higher than that of the LFS one. The same can be said for the Langmuir probe density and temperature. The main difference between Ip, Te and n_e for HFS and LFS is the large fluctuations in the case of HFS, as opposed to the small difference between both. Several hypotheses arise as to why this peculiar phenomenon occurs. One of which is that the impurities in the case of HFS are so large that they act as a resistance to the plasma current. Another hypothesis is that the plasma is rapidly and uncontrollably drawn outwards by the magnetic field, until it makes contact with the wall, in which case it disappears. To verify this hypothesis, a detailed investigation of the fast camera image is required, as shall be thoroughly discussed later in this section.

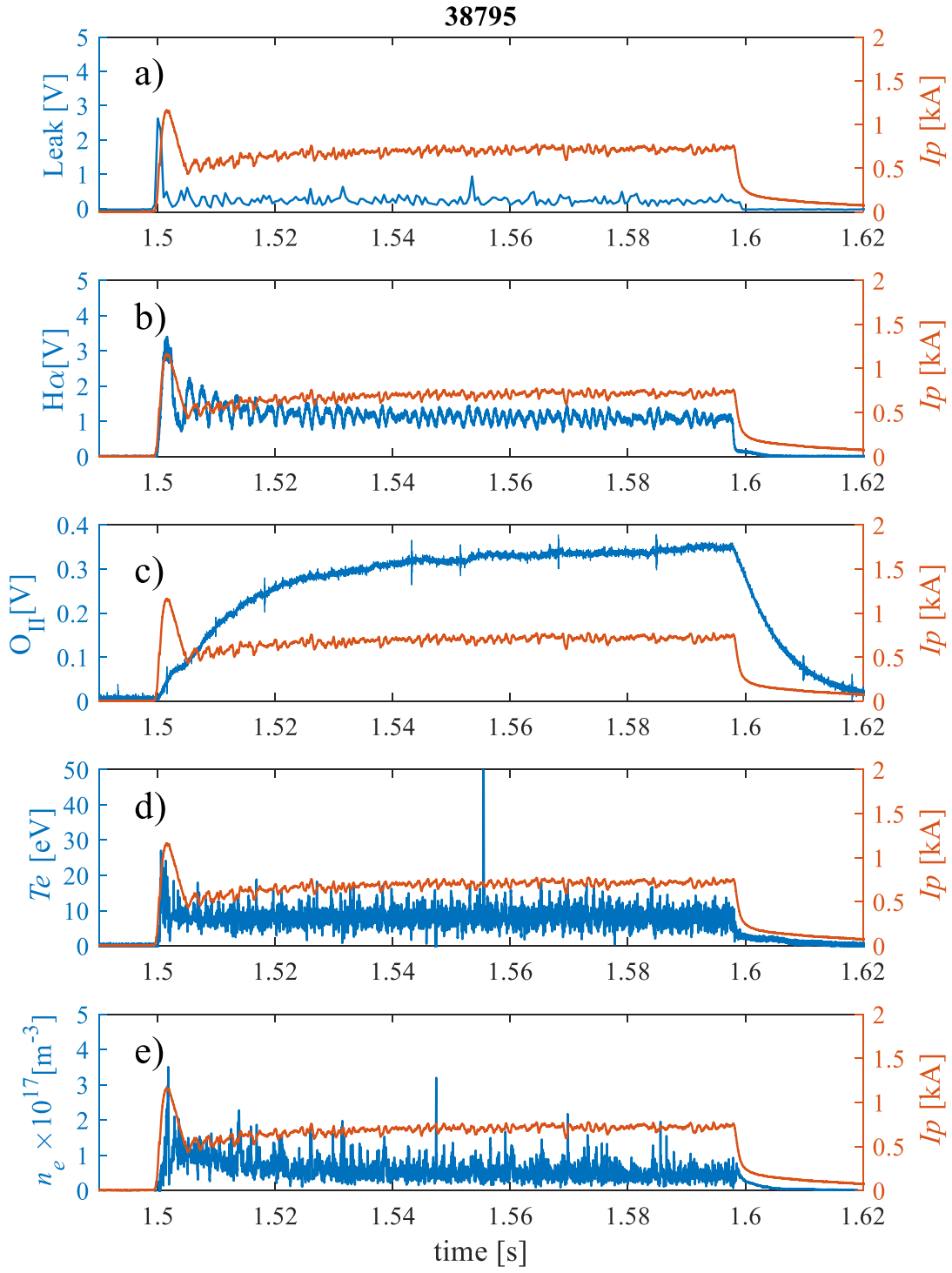

Fig. 56 Shot number 38795: 100ms HFS injection at $B_{PF2\text{-}6}$=0.78mT, R_{ECRL}=0.44m, GP=24ms such that a) is leakage monitor measured in volts, b) Hα radiation sensor measured in volts, c) oxygen sensor measured in volts, d) Langmuir probe's electron temperature measured in eV (at Z=19cm) and e) Langmuir probe's electron density measured in m^{-3} (at Z=19cm) . The right y-axis in all those figures show plasma current measured in kA.

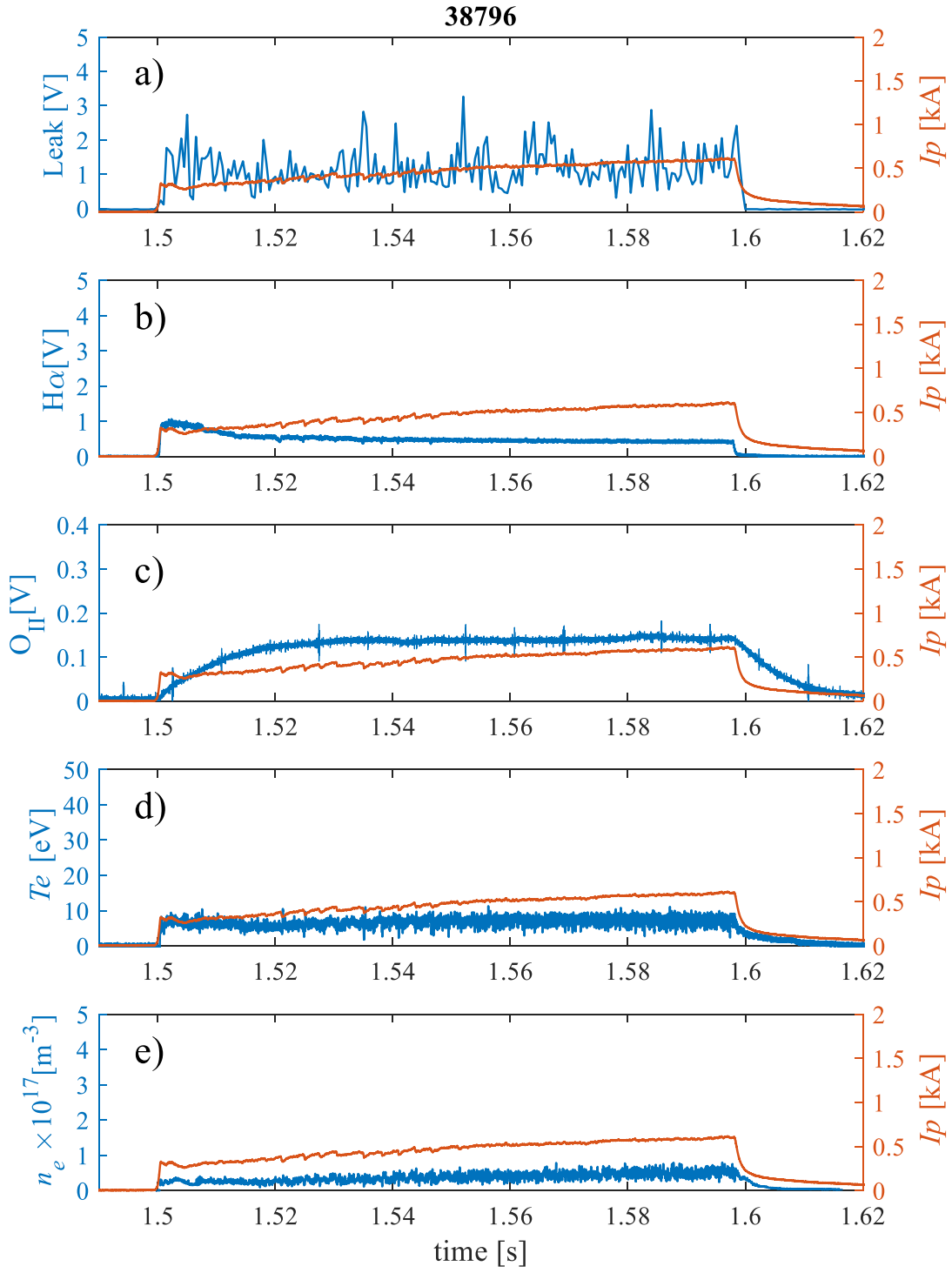

Fig. 57 Shot number 38796: 100ms LFS injection at $B_{PF2\text{-}6}$=0.78mT, R_{ECRL}=0.44m, GP=24ms such that a) is leakage monitor measured in volts, b) Hα radiation sensor measured in volts, c) oxygen sensor measured in volts, d) Langmuir probe's electron temperature measured in eV (at Z=19cm) and e) Langmuir probe's electron density measured in m^{-3} (at Z=19cm) . The right y-axis in all those figures show plasma current measured in kA.

To investigate the plasma current regression problem, the camera image needs to be inspected. The fast camera snapshots are shown in Fig. 58.

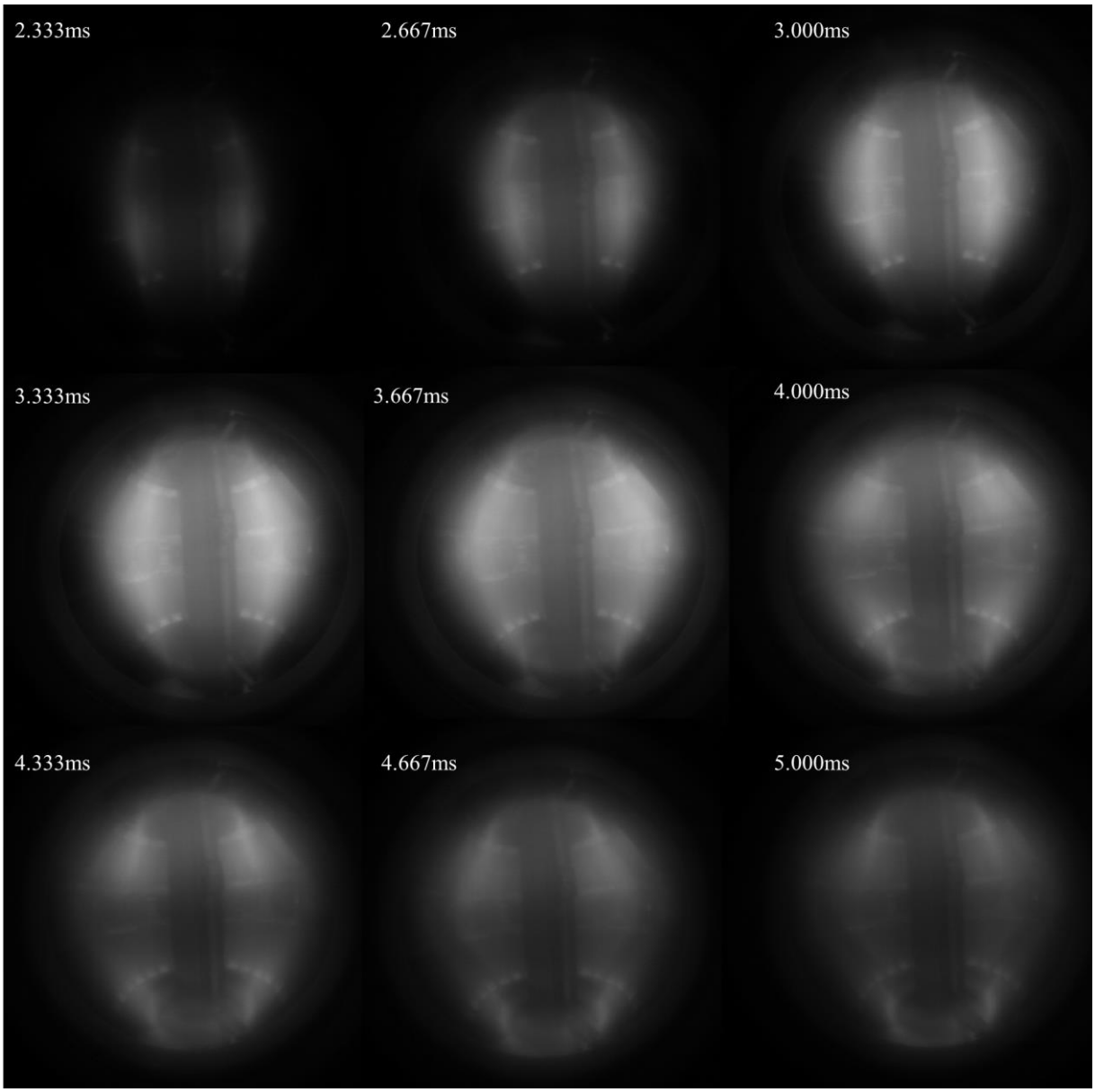

Fig. 58 The snapshots of the fast camera of shot 38941

To analyze the camera image, a meter was set inside the vessel and a picture was taken to understand the scaling as shown in Fig. 59 where each mark represents 10 cm. This can help translate pixels to meters where the exact position of the plasma can be accurately determined with simple image processing techniques. A mid-plane segment was acquired from the camera image starting from the center stack and ending at the vessel wall. This segment is where the scale lies so that the translation from pixels to meters can be done accurately. During the plasma discharge, the plasma brightness distribution is captured, translated to a graph function in the major radius R and the brightness, but also has a third dimension which is time (this shall be discussed in details later in section 5.2.3). In this case, the maximum brightness point can be fetched and represented as a function in time. This will in turn enable us to monitor the radial

change in the maximum brightness point. The results are shown in Fig. 60.

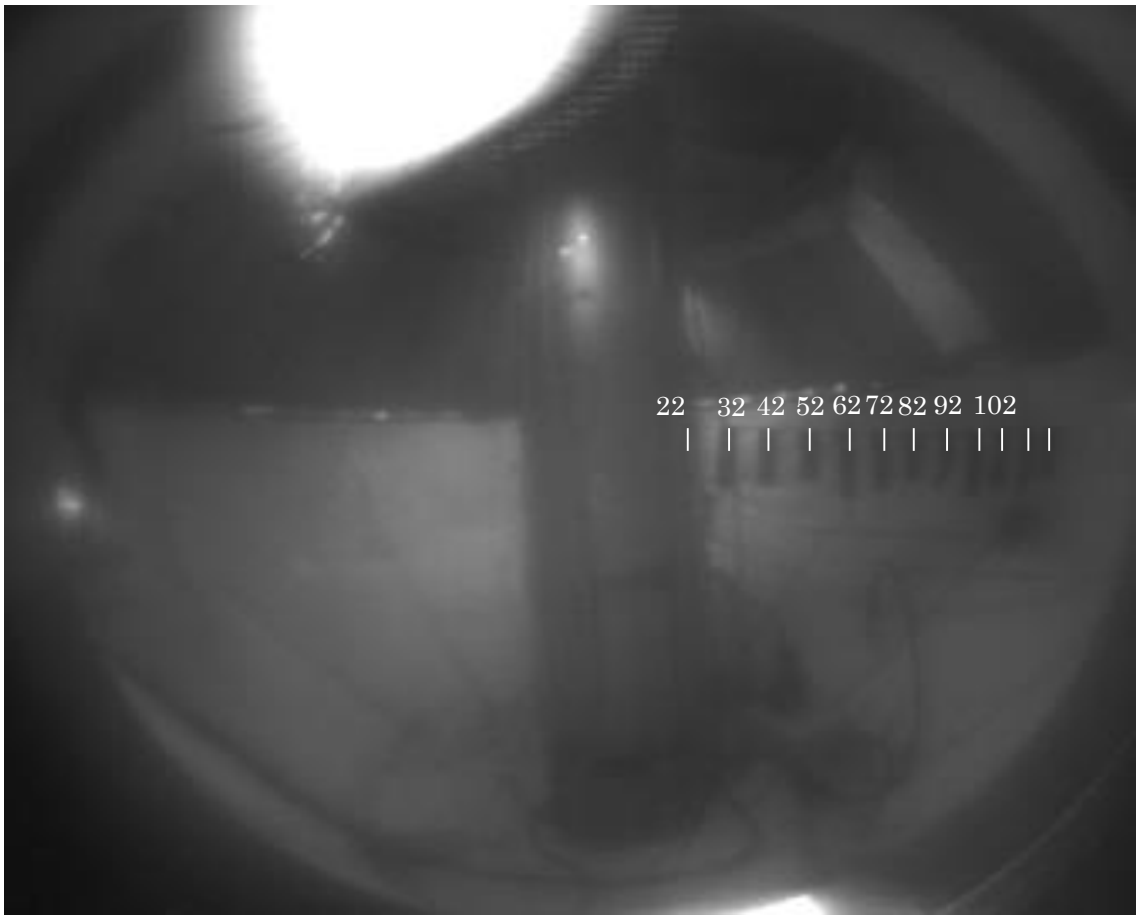

Fig. 59 A scale was installed to measure the distance, while capturing the camera image from the exact same position as the plasma shots. This is to translate pixels to distance

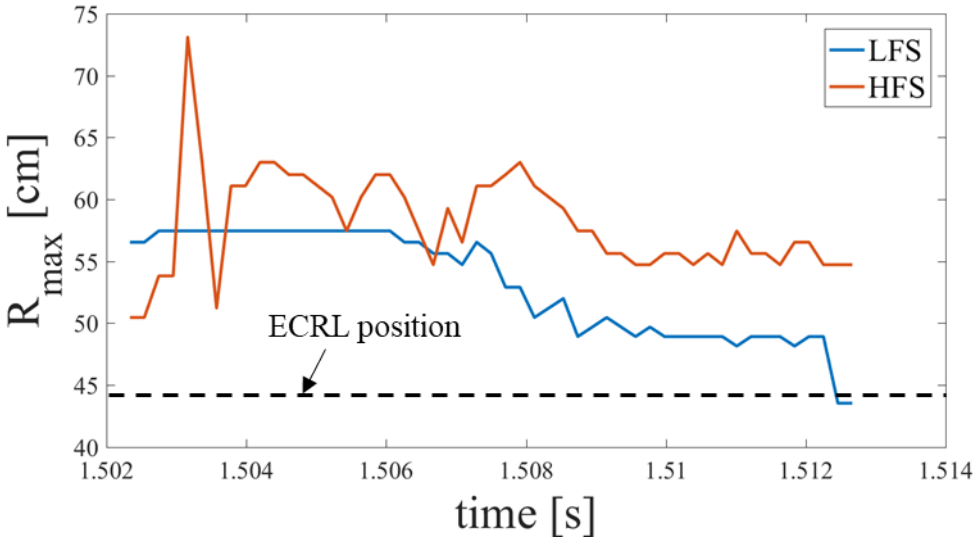

Fig. 60 The time evolution of R_{max} where R_{max} is the radial position of the brightest point at the mid-plane

As shown in Fig. 60, the maximum radial position of the brightest point is far away from the wall (140cm), therefore there is no indicator that the plasma is making contact with the wall at some time during the discharge.

5.2.1 Sideband measurement

EBW excitation has already been confirmed at this point, after testing the UHRL position, comparing between HFS and LFS injections results (brightness, Ip and Te) and comparing their absorption. With EBW conversion at hand, sideband detection (as discussed in section 4.2.2) should be possible.

Several attempts to measure the sideband data were conducted. However, it was concluded that measuring the sideband by connecting the spectrum analyzer to one of the LFS antennas is ineffective, so connecting it from the HFS was the only option. Connecting the spectrum analyzer to the HFS antenna showed a sideband measured at 8.1 GHz (see Fig. 61), however, the main lobe to side lobe ratio (side lobe level) is too high compared to theoretical prediction.

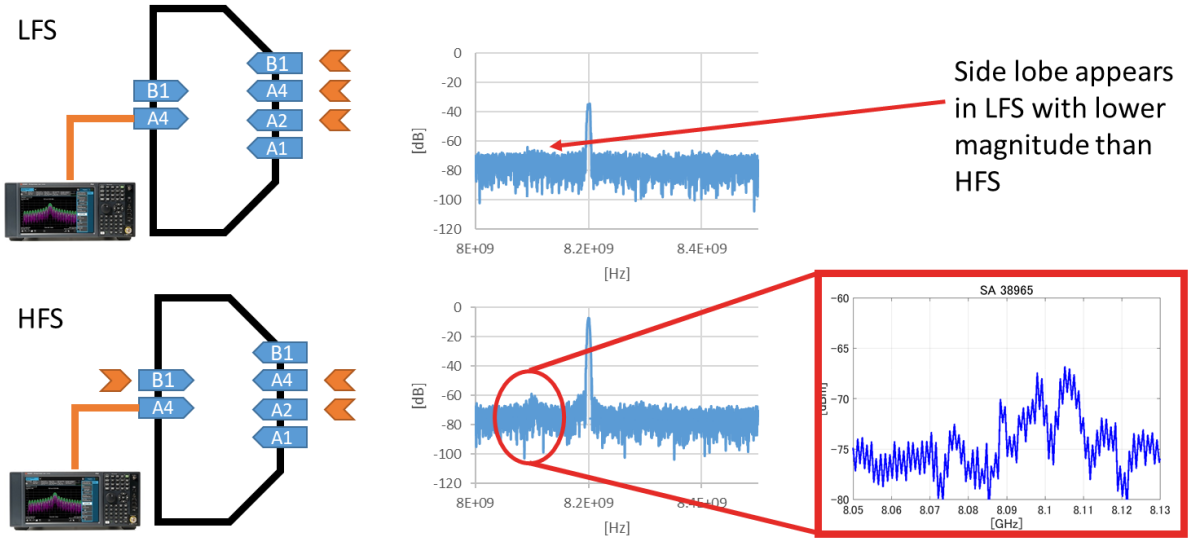

Fig. 61 LFS and HFS spectrum analyzer results such that 'LFS' indicates 3 klystrons injecting from LFS while connecting the spectrum analyzer from the HFS and 'HFS' indicates only one klystron firing from HFS because the spectrum analyzer is connected to the HFS, and another two are firing from LFS.

Various reasons could be associated with this including the fact that the HFS antenna is located near the center stack, which is far away from the UHRL where mode conversion takes place, hence there is a path loss.

Furthermore, it is expected from the lower hybrid detection measurement to have a very low magnitude lobe as well since the Langmuir probe is far away from the UHRL (see Fig. 39).

The output FFT signal of the oscilloscope is shown in Fig. 63. It can be seen that the spectrum is located at 80 MHz rather than the spectrum analyzer's 100 MHz, in which lower-than-expected measurement was observed in [81] reporting that the spectrum was at a slightly lower frequency than expected.

Both Fig. 64 and Fig. 63 show that the HFS sideband and LHW are more prominent (of higher magnitude) than that of the LFS, endorsing the fact that EBW conversion took place and that HFS has higher conversion efficiency than that of the LFS. To compare those results to the theory, the LHW frequency was calculated such that

$$\omega_{LH} = \frac{1}{\sqrt{\frac{1}{\Omega_e \Omega_i} + \frac{1}{{\omega_{pi}}^2}}} \qquad 5.2.1$$

such that ω_{LH} is the LH angular frequency, Ω_e and Ω_i are the electron and ion cyclotron frequencies respectively, and ω_{pi} is the ion plasma frequency. The LHW frequency can be expressed as a function in the radial position as shown in Fig. 62 by substituting ω_{pi} with $\omega_{pe} m_i/m_e$ in the equation 5.1.1.

The expected BW1 is 30 MHz.

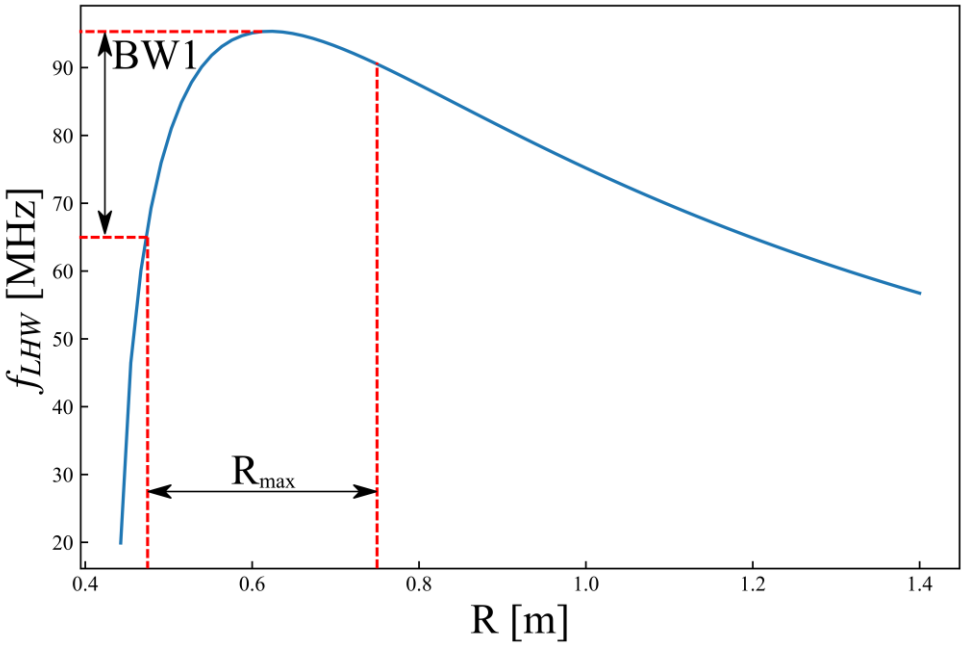

Fig. 62 LHW frequency vs R where R_{max} is the same as that in Fig. 60 and BW1 is the LHW bandwidth

It can be concluded that the expected BW to be measured is in the range of 65~88 MHz, while for the HFS case, BW should be more than that of the LFS case. This should be an indicator that R_{max} does indicate the UHRL position.
Fig. 63 shows the measured results of the Langmuir probe, with a HFS BW1 of 10 MHz while in the LFS case, BW1 was 4 MHz. The measured BW1 are the half-power-beam-width (HPBW).

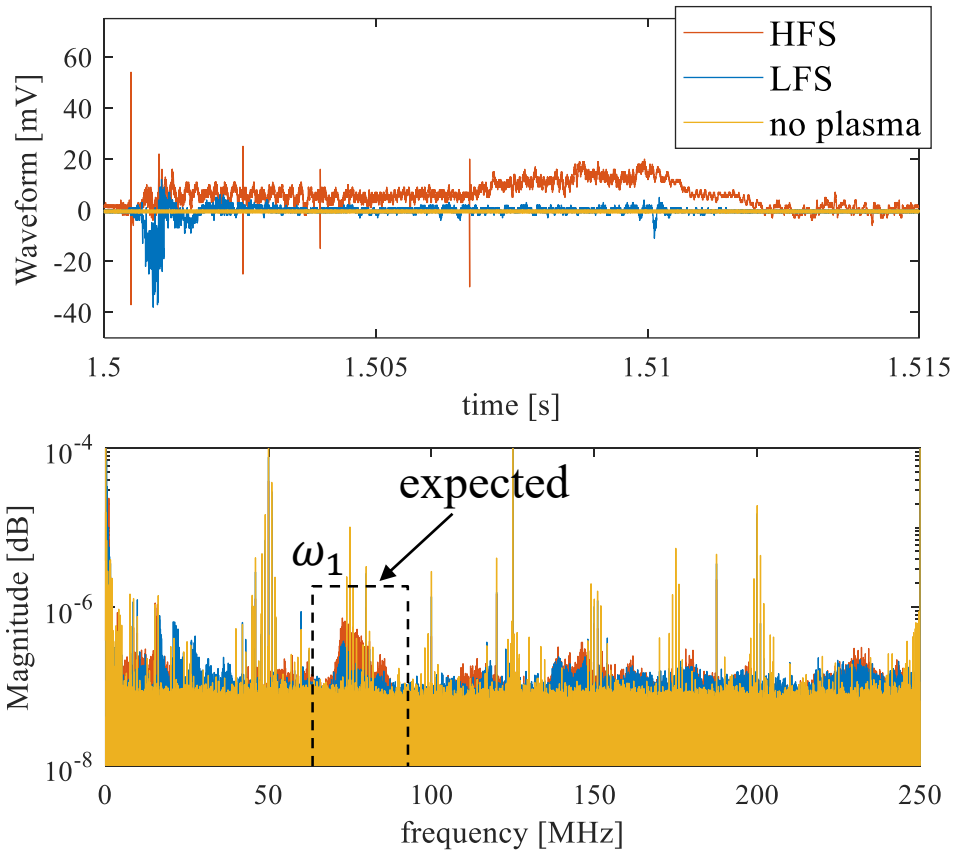

Fig. 63 (Upper) the Langmuir probe antenna's waveform as captured by the oscilloscope, and (Lower) is the spectrum after FFT conversion. The no plasma shot was included for reference. The dotted-black line shows the expected LHW bandwidth only without any magnitude expectations.

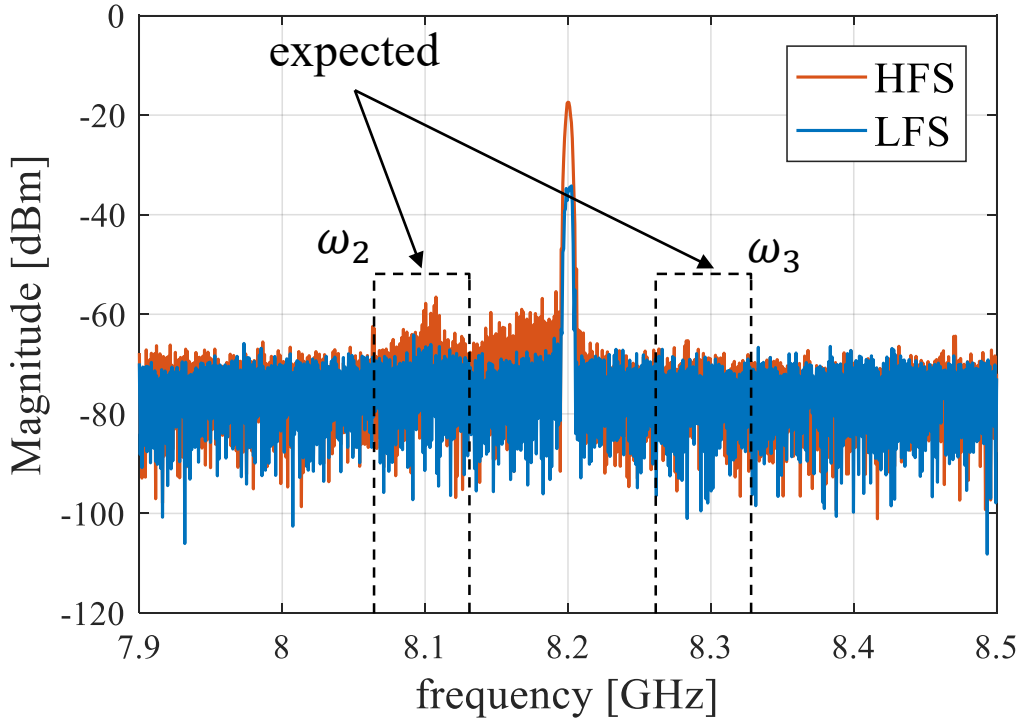

Fig. 64 SA reading of HFS and LFS such that the dotted black line is the expected sideband bandwidths.

Fig. 64 shows that the ω_2 side lobe of the HFS case is at -55 dBm while the LFS one is at -65 dBm. In addition, the ω_2 side lobe was measured at a frequency of 8.1GHz as theory predicted. However, the bandwidth for HFS case is larger than that of the LFS case, which can be attributed to the fact that the UHRL is moving outwards, causing a Doppler's blue shift. This further indorses the fact that EBW conversion took place both in HFS and LFS case, with HFS having better conversion efficiency. Not to mention, the ω_3 side lobe was also measured with very low magnitude at -65 dBm for the HFS case, and -70 dB for the LFS one. One problem with this measurement system is that diffraction between adjacent antennas occurs. Since the spectrum analyzer is connected to the HFS injection antenna, HFS injection would cause a lot of diffraction leading to a higher main lobe (at 8.2 GHz) for HFS despite HFS injection system having higher absorption efficiency. In conjunction, LFS injection would cause a peak of -10dBm when connecting the spectrum analyzer to an adjacent LFS antenna.
An ω_3 side lobe magnitude lower than that of the ω_2 side lobe is normal and was reported in several literatures such as [57] and [82]. Both cases were measured at a frequency of 8.3GHz as theory predicts. Moreover, the LHW side lobe for both the HFS and LFS cases was measured at a frequency that matches that of the theoretical prediction. To confirm that the LHW signal is not just noise, both a low pass filter (LPF) and a high pass filter (HPF) were applied to the signal to confirm whether the higher frequency components are just noise. It can be seen from the HPF signal that after applying IFFT to the spectrum, the waveform has partial agreement with that of the Hα one, suggesting that the existence of this lobe might be due to EBW excitation.

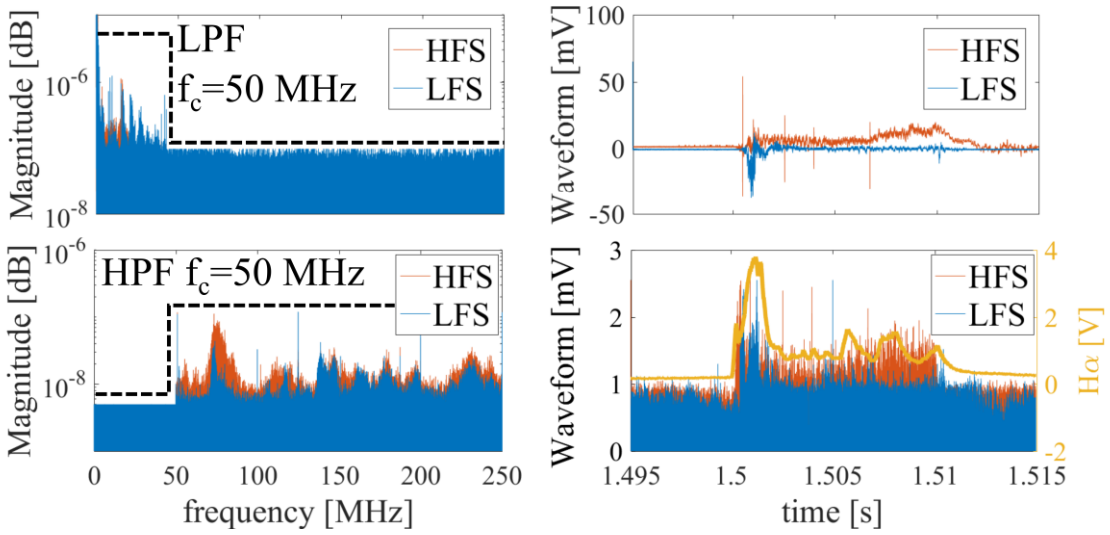

Fig. 65 (Top) Ideal low pass filter spectrum (right) and wavegorm (left) for a cutoff frequency of 50MHz, and (bottom) ideal high pass filter for the spectrum (left) and waveform (right) for a cutoff frequency of 50MHz. The bottom right figure has the no plasma at 0mV so it is invisible as it lies behind the HFS and LFS signals, and the right yaxis and the purple curve show the Hα time evolution of this shot.

5.2.2 EBWH/CD results

An attempt to test EBWCD excitation was conducted. In order to ensure that the obtained plasma current is not pressure driven, reversing the polarity of the poloidal field was applied. However, with reversing the polarity of the poloidal field, plasma current did not change much indicating that the obtained plasma current is dominated by pressure-drive (as shown in Fig. 66). It is inconclusive to state that EBWCD did not occur as it could have been masked by the pressure-driven current since in QUEST, pressure-driven currents of up to 2 kA were experienced before. Therefore, higher plasma current is required for EBWCD to be achieved. In order to get a higher plasma current, CFS formation is necessary.

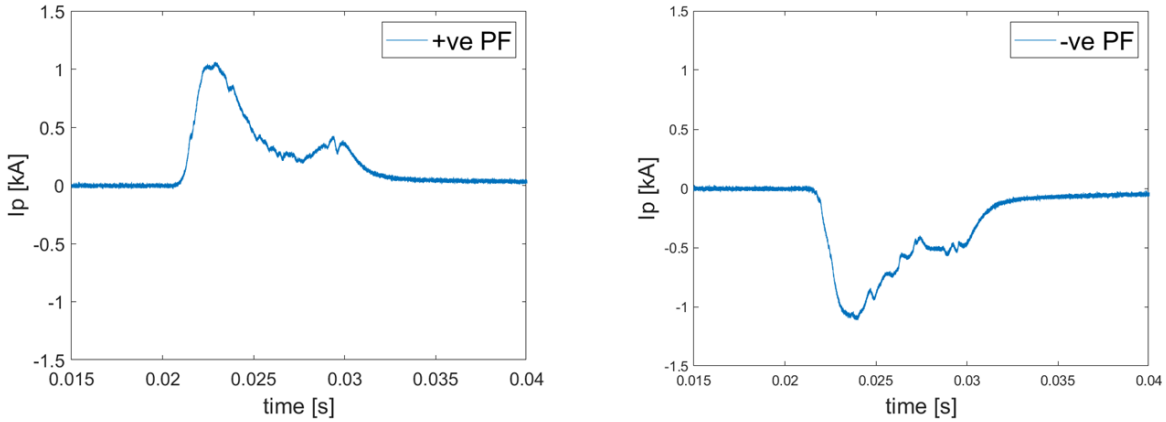

Fig. 66 (Left) Ip for forward polarity of the poloidal field, peaking at 1.1 kA, and (Right) Ip for reverse polarity of the poloidal field peaking at -1.06 kA

To attempt to create a closed flux surface, and to achieve higher plasma current (more than that of the pressure-driven threshold of 2kA), CS (PF4) was operated even though this seems to be counter-intuitive as the primary target of this work is to heat and drive plasma current non-inductively. Nonetheless, the effect of EBW current drive was the purpose of checking for this test.

The results of the PF4 use is shown in Fig. 69 and Fig. 70 for HFS, and Fig. 71 for LFS. In shot 38957, PF4 had its Ip-ramping effect a little late, so it started affecting Ip after it regressed. In shot 38959, PF4 was set a little earlier to counter this effect, which as shown in Fig. 70 was successful, however, the overall Ip did not increase much in comparison. The same was conducted for shot 38973 (Fig. 71), which is just for the LFS for comparative purposes. It can be concluded that the plasma did not form a closed flux loop, as shown in Fig. 67 for HFS, and Fig. 68 for LFS. EBWCD's absence could be attributed to the fact that with this poloidal field configuration, the magnetic decay index (n_{index}) is low. In Kyoto University's reactor, LATE, after moving the limiter from 0.125m to 0.25m (changing the aspect ratio from 1.3 to 3), an n-index of 0.25 was required to be achieved instead of 0.05 for the CFS to be formed and for the plasma current to jump [83]. n_{index}, calculated as

$$n_{index} = \frac{RB_p}{\partial R \partial B_p} \qquad 5.2.2$$

is 0.17 at the ECRL and the mid-plane in our case, whereas it should be larger than 0.3 given that the plasma limiter is now set at 0.37m instead of the default 0.22m. To increase n_{index}, the inclusion of other PF coils would be required. An n_{index} of 0.36 can be achieved in the case of including PF1-7 with a coil current of $B_{PF1\text{-}7}$ = -0.43mT along with $B_{PF2\text{-}6}$ = 0.78mT.

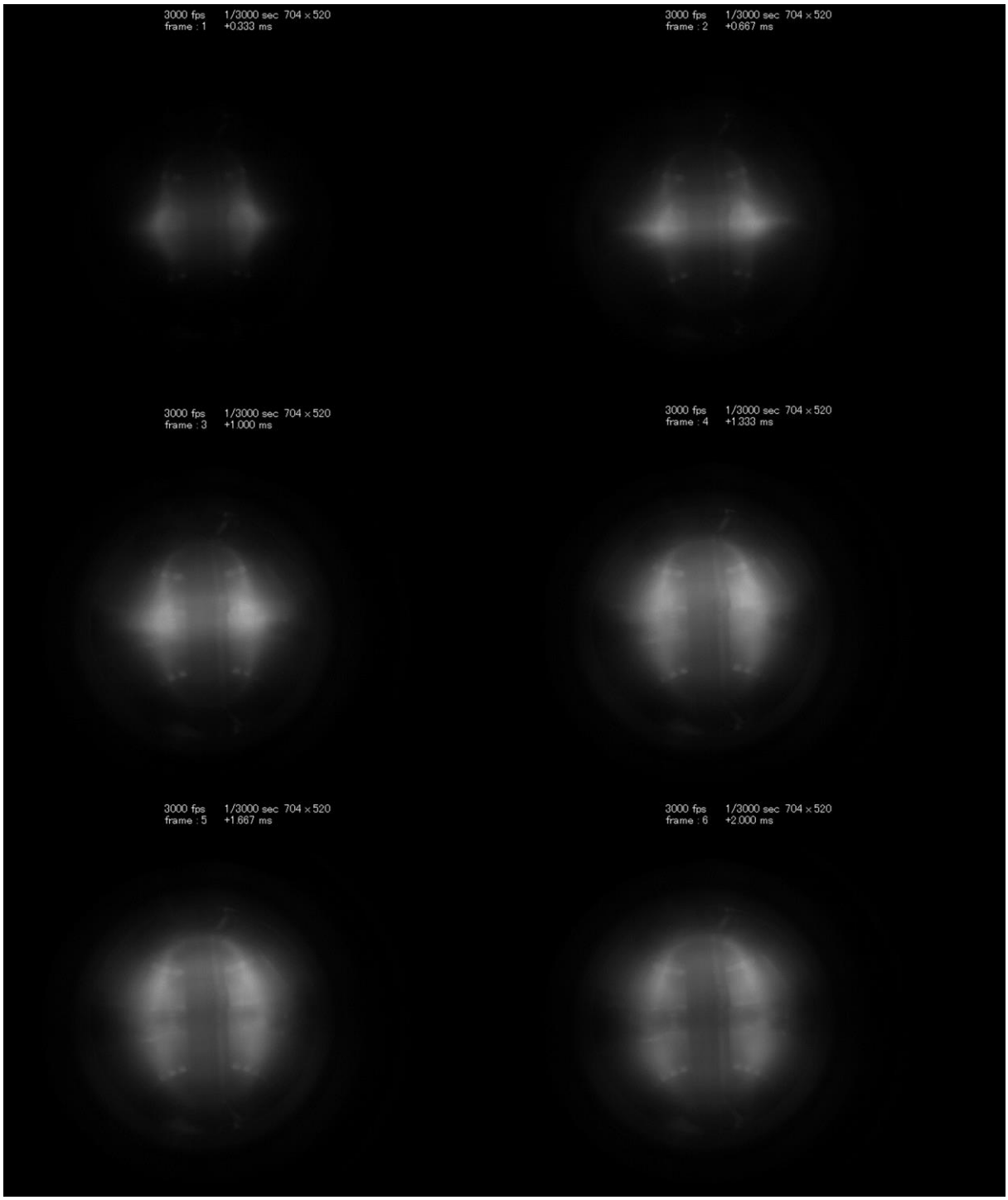

Fig. 67 Fast camera snapshot results for HFS with PF4 (shot 38957) for nine instances from 0.333ms to 2.000ms

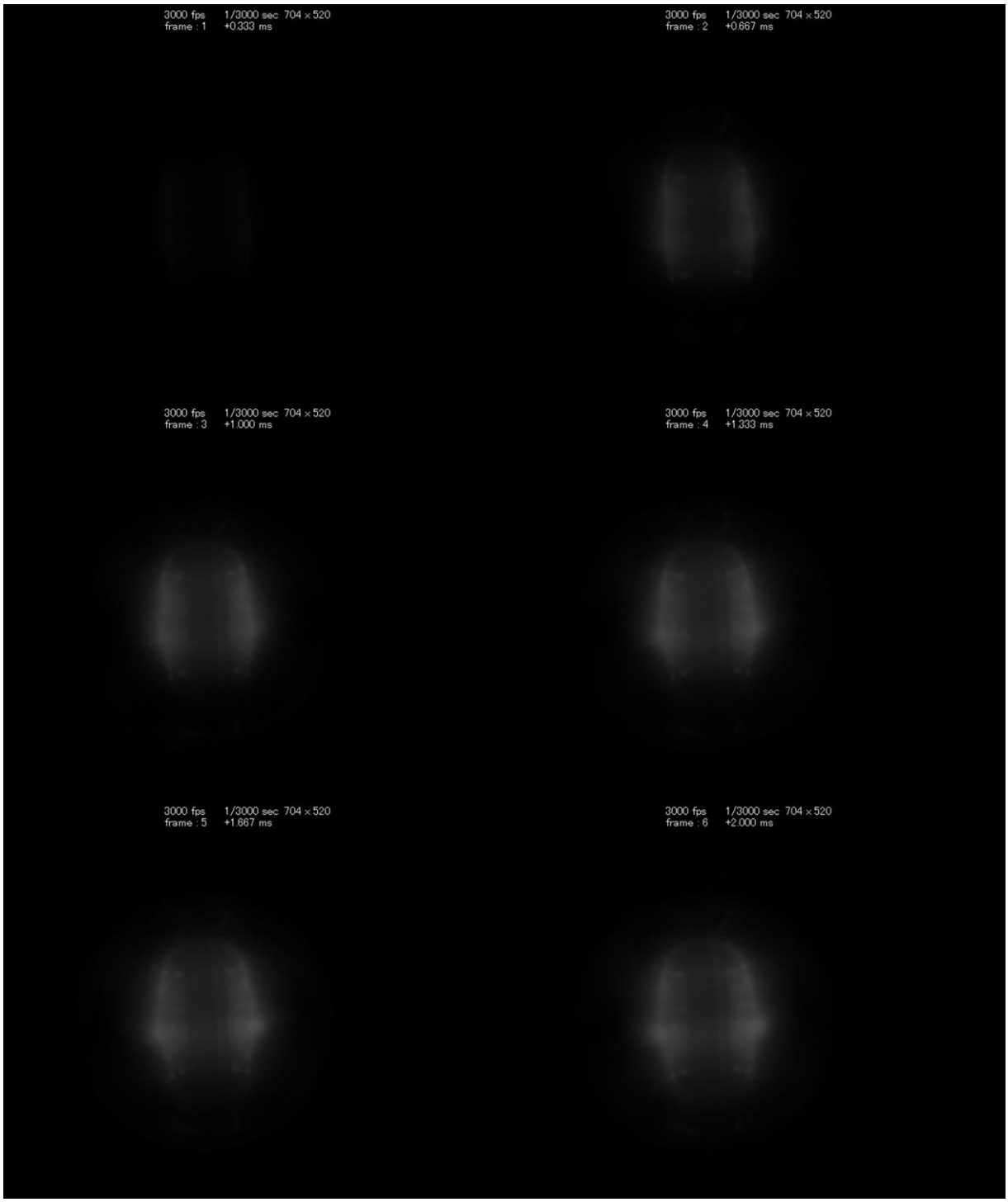

Fig. 68 Fast camera snapshot results for HFS with PF4 (shot 38973) for nine instances from 0.333ms to 2.000ms

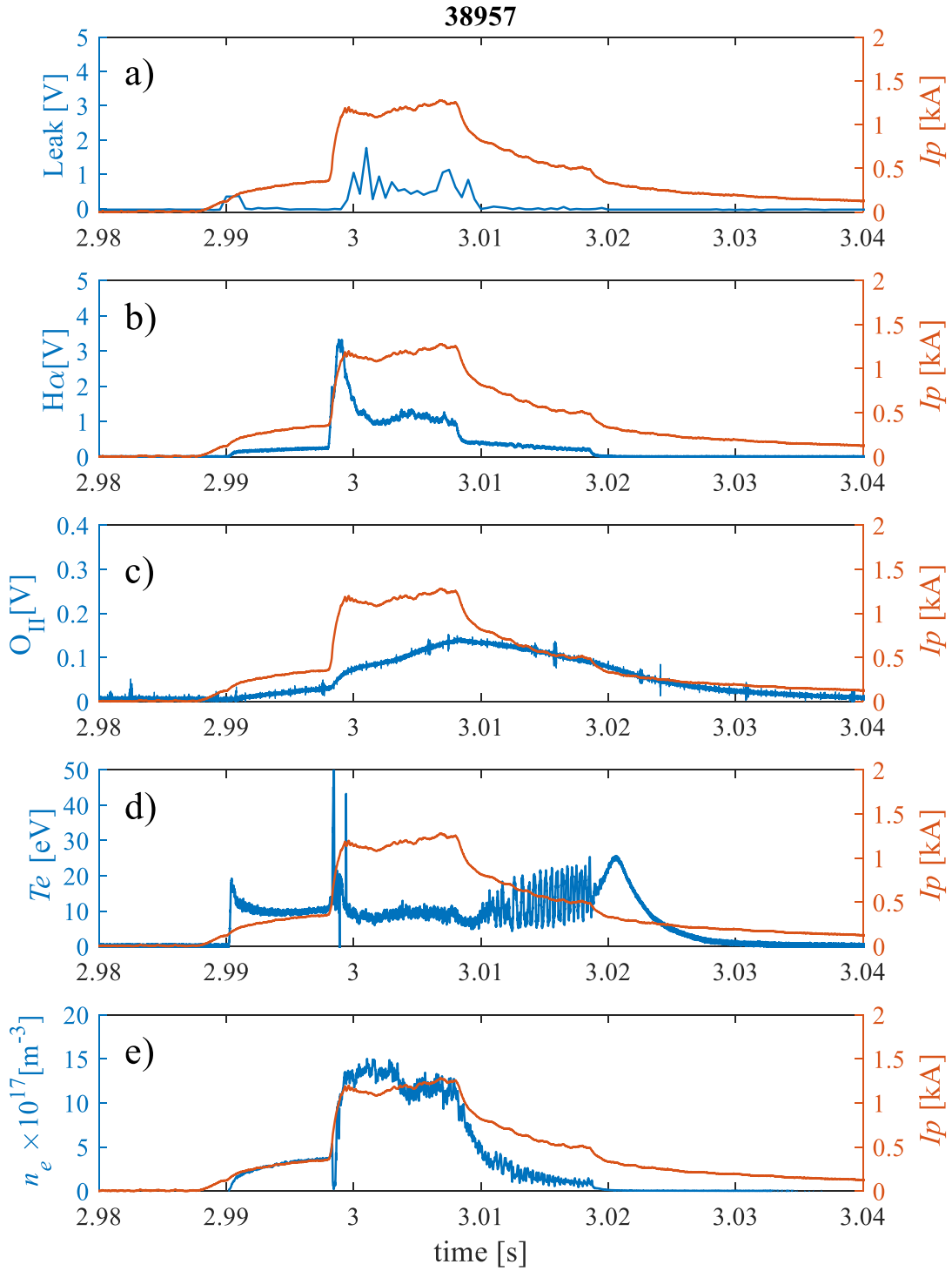

Fig. 69 Shot number 38957: HFS injection at $B_{PF2\text{-}6}$=1.5mT, $B_{PF1\text{-}7}$=0.0863mT, R_{ECRL}=0.44m, GP=24ms, and B_{PF4}=- 0.6578mT such that a) is leakage monitor measured in volts, b) Hα radiation sensor measured in volts, c) oxygen sensor measured in volts, d) Langmuir probe's electron temperature measured in eV (at Z=19cm) and e) Langmuir probe's electron density measured in m^{-3} (at Z=19cm) . The right y-axis in all those figures show plasma current measured in kA.

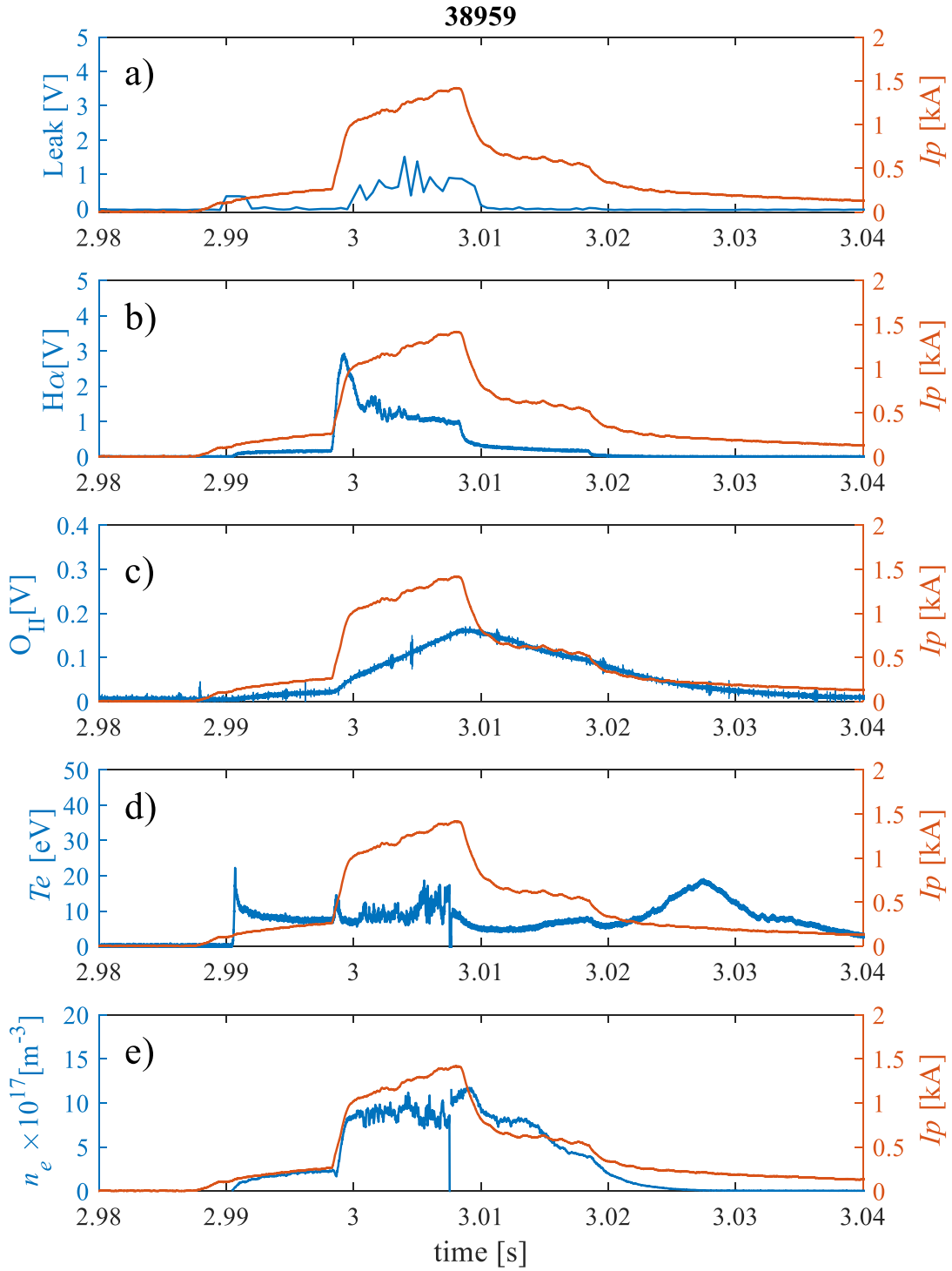

Fig. 70 Shot number 38959: HFS injection at $B_{PF2\text{-}6}$=1.5mT, $B_{PF1\text{-}7}$=0.0863mT, R_{ECRL}=0.44m, GP=24ms, and B_{PF4}=- 0.6578mT but starts rising 10ms earlier than 38957. a) is leakage monitor measured in volts, b) Hα radiation sensor measured in volts, c) oxygen sensor measured in volts, d) Langmuir probe's electron temperature measured in eV (at Z=19cm) and e) Langmuir probe's electron density measured in m^{-3} (at Z=19cm) . The right y-axis in all those figures show plasma current measured in kA.

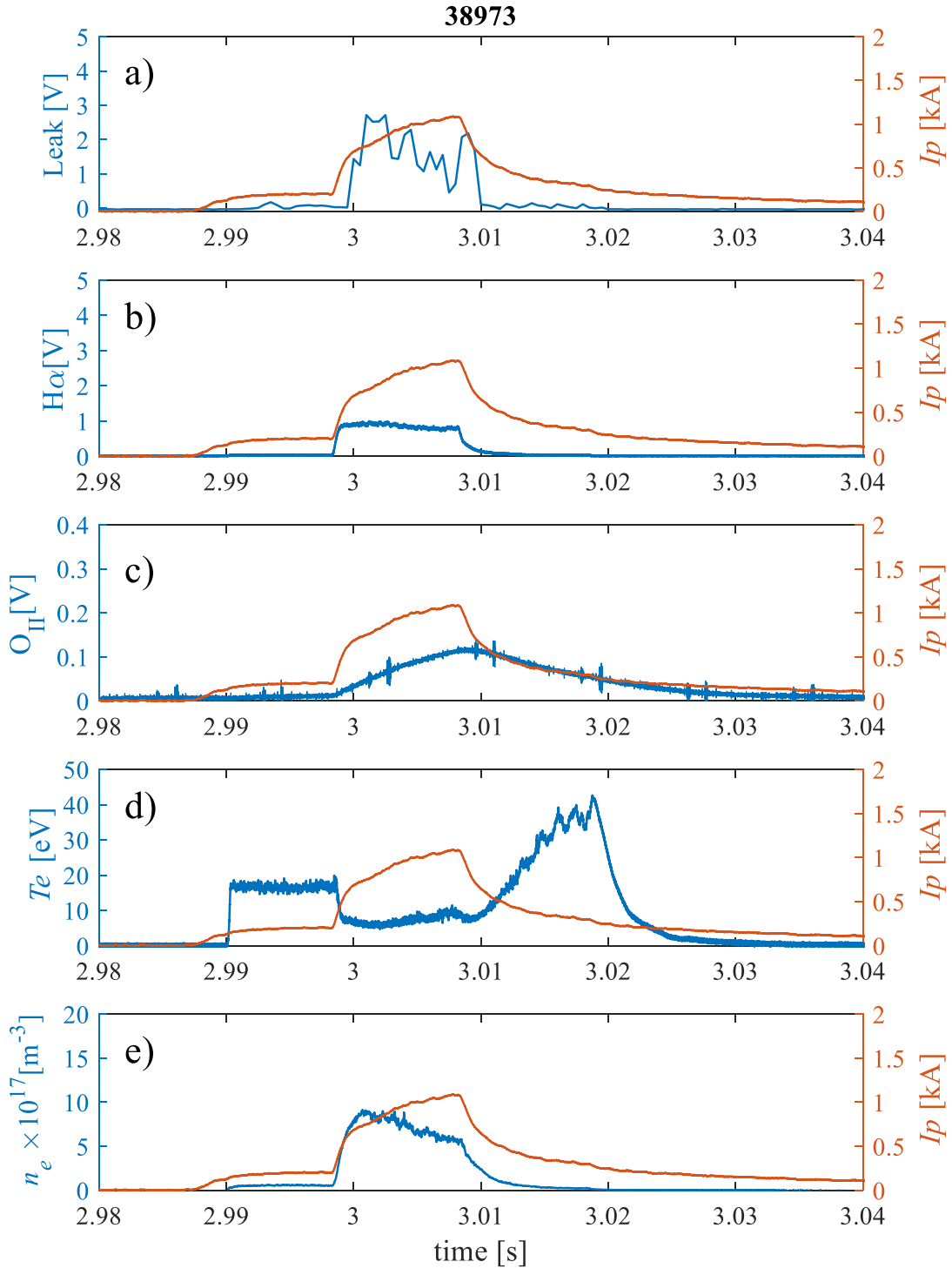

Fig. 71 Shot number 38973: LFS injection at $B_{PF2\text{-}6}$=1.5mT, $B_{PF1\text{-}7}$=0.0863mT, R_{ECRL}=0.44m, GP=24ms, and B_{PF4}=- 0.6578mT and starts at the same timing as shot 38959. a) is leakage monitor measured in volts, b) Hα radiation sensor measured in volts, c) oxygen sensor measured in volts, d) Langmuir probe's electron temperature measured in eV (at Z=19cm) and e) Langmuir probe's electron density measured in m^{-3} (at Z=19cm) . The right y-axis in all those figures show

plasma current measured in kA.

The results of using PF4 coil are shown in Fig. 69, Fig. 70 and Fig. 71. For the cases of using PF4, a loop voltage as shown in Fig. 72 was used in all of them. All diagnostics started at 2.99s even though the RF power started at 3.00s. This breaks down plasma before RF injection, which can help improve plasma performance such as absorption. A peculiar Te waveform exists in the case of using PF4, which is because the center stack drives the energetic electrons, causing the probe temperature to rise after the RF power is off. It is noteworthy to mention that even though plasma current sustained consistently in the case of HFS injection, however, Hα kept its unstable form as shown in Fig. 69 and Fig. 70. Moreover, Fig. 71 showed a low absorption percentage even with the usage of PF4. Nonetheless, Langmuir probe temperature and density rose significantly in both HFS and LFS injections, and in the case of LP Te, LFS achieved higher temperature, but this is solely based on energetic electrons as the peak temperature was achieved after the RF power was cut. Moreover, Ip significantly rose in the case of LFS injection, while in the case of HFS injection, the rise was slightly higher than the initial phase that occurs in the absence of PF4.

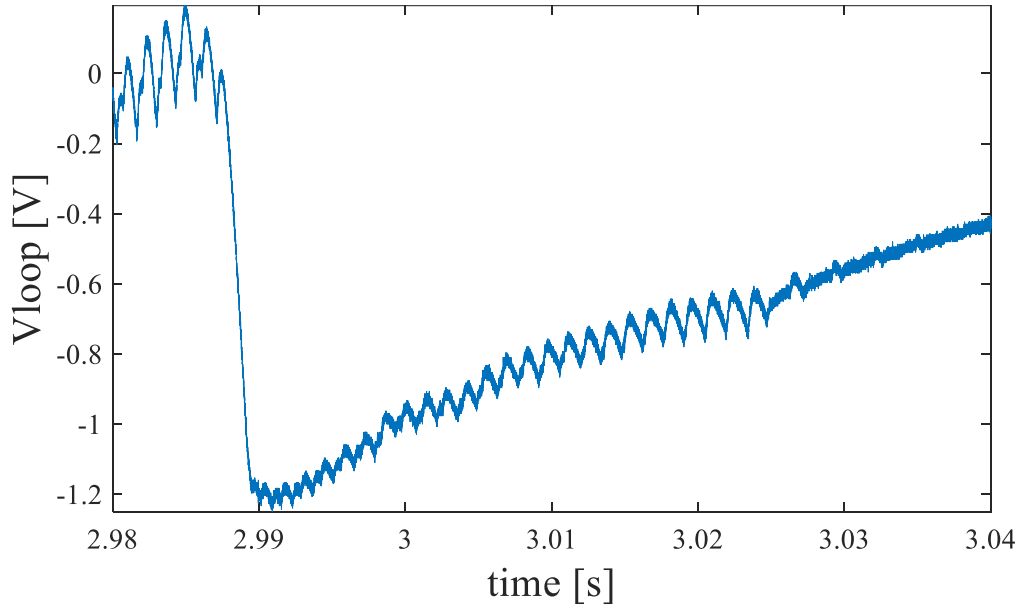

Fig. 72 Time evolution of the center stack loop voltage. It started from 2.99s while the RF power injection started at 3.0s. This loop voltage is the equivalent of a magnetic field of 1.495mT at the mid-plane and the ECRL position.

5.2.3 High Density plasma production results

The interferometer only measures line-integrated density, which is not necessarily useful without translating it to line-averaged density. The formula for translating from line-integrated density to line-averaged density is

$$\int_l n_e = \overline{n_e} * 2l \qquad 5.2.3$$

where l is the path length of microwave to measure the density and interferometer signal is integrated along with the path length. Therefore, in order to obtain $\overline{n_e}$, l needs to be carefully analyzed for results that are as accurate as possible.

In order to evaluate l, it is important to first analyze the camera image in a 3D fashion where the x-axis is time, y-axis is radius, and z-axis is brightness as shown in Fig. 73

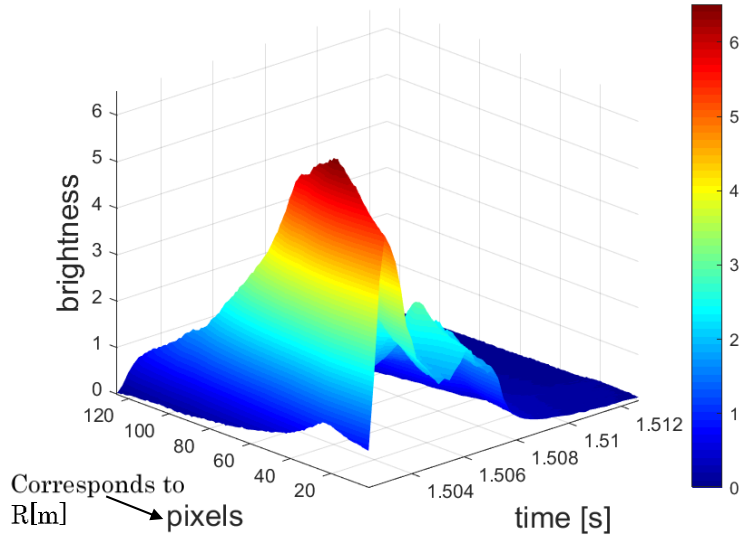

Fig. 73 A 3D image of the plasma video for HFS injection (shot 38941) after only considering the mid-plane slice, where x-axis is time, y-axis is pixels representing the radial axis, and z-axis is brightness.

Then the translation from pixels to radius is to be conducted by using the scale created in Fig. 74

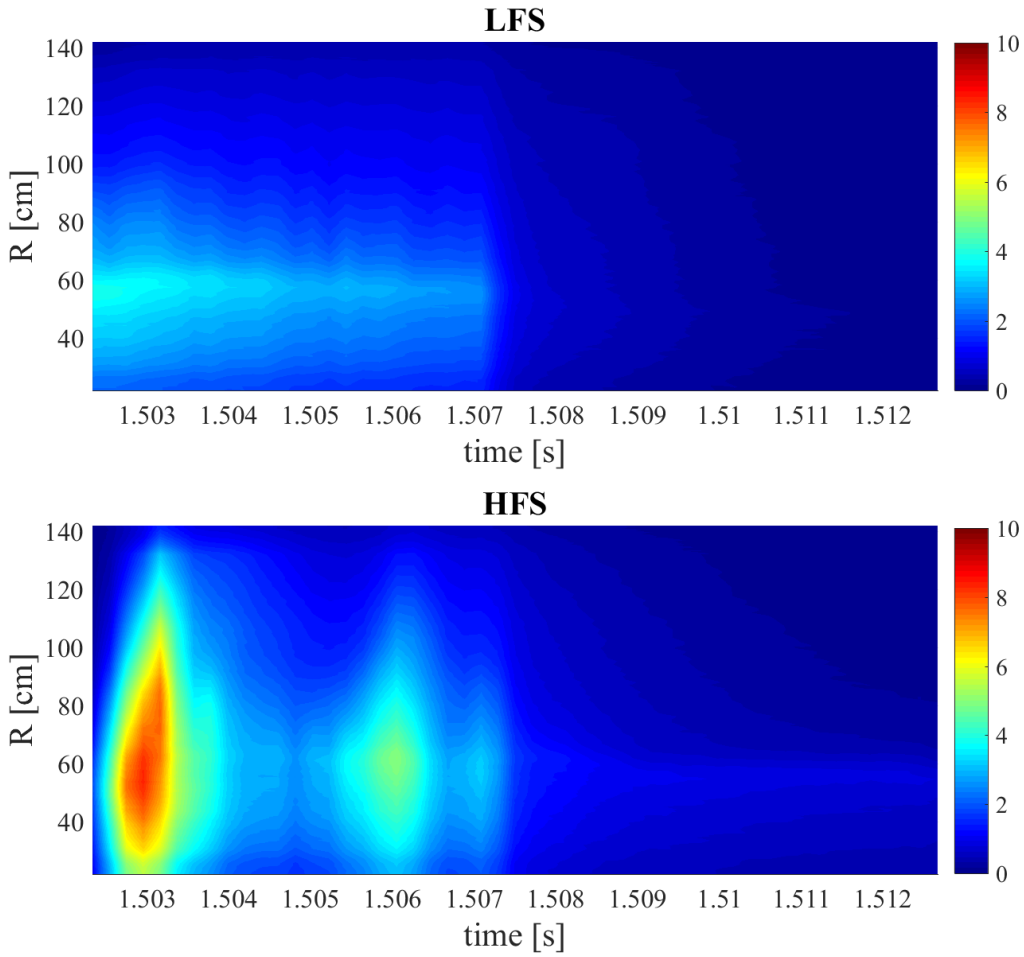

Fig. 74 Comparison between LFS (shot 38939) and HFS (shot 38941) for the mid-plane slice of the camera video such that the x-axis represents time, y-axis represent radius R, and the color axis represents camera image brightness

To decide where plasma starts and stops, a threshold needs to be set. First, we take a snapshot at a particular time (for example at t = 1.503 s because it is the brightest time sample) as shown in Fig. 75

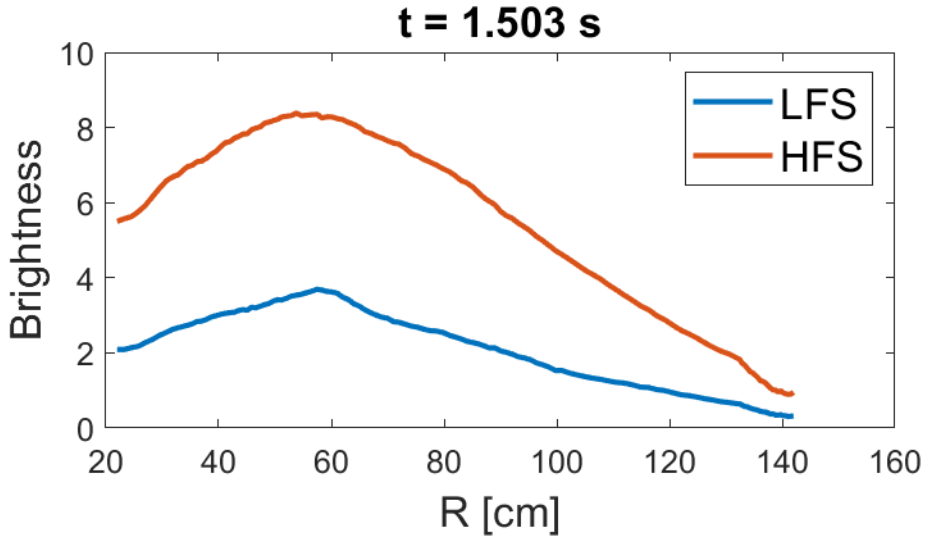

Fig. 75 The brightness for LFS (shot 38939) vs HFS (shot 38941) as a function in the radius R at time t=1.503s

Two methods of setting a threshold exist:
(a) hard threshold
(b) soft threshold.

Hard threshold:
Just set a brightness level for which, anything lower is assumed to be background noise. This method doesn't consider the fact that background noise is proportional to plasma brightness.
For example, if we considered that background noise is where brightness is less than 3, then apply to both HFS and LFS, we will get
$R_{LFS} = 39{\sim}69cm$ and $R_{HFS} = 37{\sim}117cm$

Soft threshold:
An adaptive threshold, based on the peak brightness of each case is to be considered
For example, if we considered each case on its own and set background noise to be 50% of peak brightness, we will get
$R_{LFS} = 37{\sim}94cm$ and $R_{HFS} = 37{\sim}105cm$

Applying hard threshold seems to gives results that agree with visual inspection of the camera data, however, choosing the threshold value has no discrete basis other than the entire image scale and the background darkness.

Calculating l as a function in time is then required for calculating the line-averaged density time evolution. Fig. 76 shows the detailed steps of how to interpret the plasma density from the interferometer.

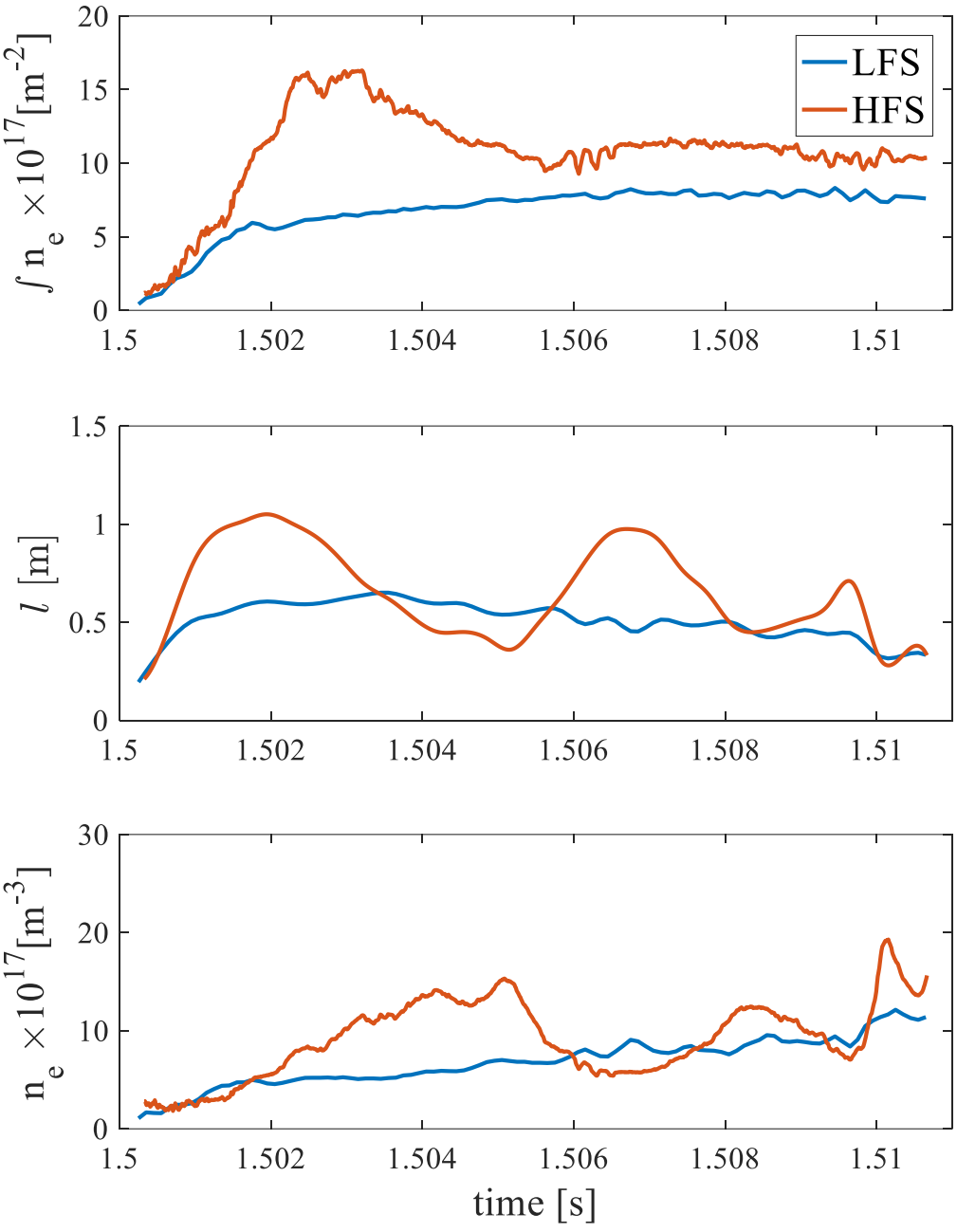

Fig. 76 Interferometer data analysis for LFS (shot 38939) vs HFS (shot 38941) where (top) is line-integrated density, (middle) the path length of the interferometer signal inside the plasma [one-way], and (bottom) is the line-averaged density at a threshold of 20%

The threshold in Fig. 76 is at 25% from the maximum brightness, giving a peak density of 18×10^{17} m^{-3}. However, a change in the threshold can dramatically change the peak density as shown in Fig. 77.

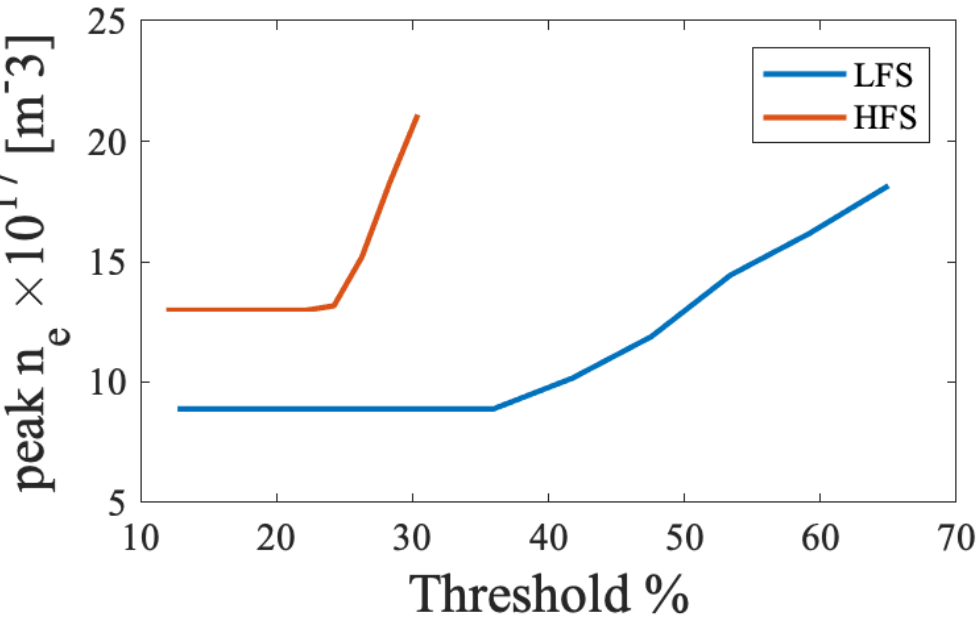

Fig. 77 Peak density as a function in the threshold percentage

Due to the fact that plasma can exist in the non-visible region, sometimes the camera image is misleading. This can complicate the threshold decision making even further. To make sure that this data is reliable, a safety measure of assuming the lowest threshold is taken, then the line-averaged density is calculated. The result for assuming a constant l of $1.4 - 0.35$ m gives a HFS plasma density 1.75 that of the cutoff density, where the LFS is the same as that of the cutoff density.

It is noteworthy to say that there is a big difference between interferometer density and Langmuir probe density. The reason why such difference exists can be attributed to the fact that the probes are placed far away from the UHRL where the mode conversion occurs as shown in

Fig. 78, and since the Langmuir probe can only measure the localized density, it should be expected to have much lower densities than the maximum.

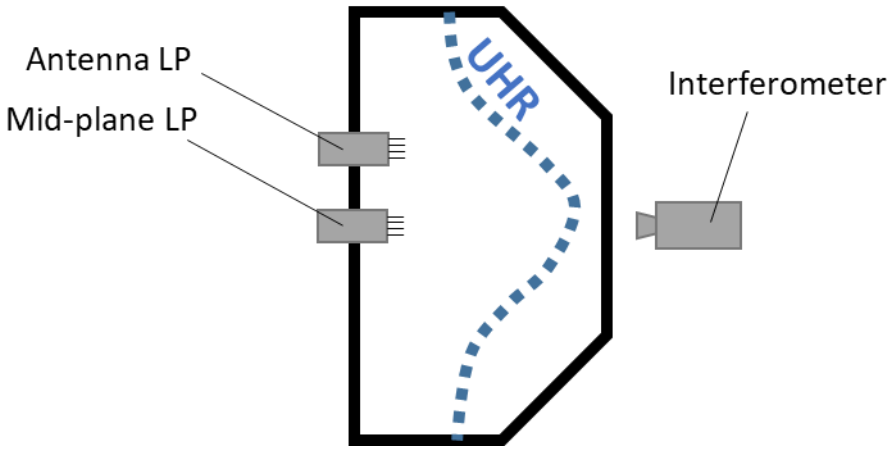

Fig. 78 The position of the HFS-installed Langmuir probe compared to the UHRL

5.3 Discussion about Ip regression and fluctuations

Several hypotheses were considered to explain the instabilities of the HFS Ip. This section discusses them in details, attempting to verify their validity.
Upon investigating the plasma current regression, several hypotheses came to mind. The first of which was that the HFS impurity is much larger than that of the LFS, as shown by the O_{II} signal, where it has a negative impact on the plasma current drive. However, after inspecting the O_{II} meter in the case of 100ms discharge, it can be clearly seen that the plasma current starts regressing while the O_{II} meter is rising. Nonetheless, as mentioned previously, the time response of this measurement system is not suitable for comparison due to the presence of the integrated circuit. Not to mention, the integrated circuit would cumulatively add data as time progresses, which explains why the O_{II} signal waveform keeps rising upon decreasing Ip. Furthermore, a small kink exists when the plasma current started regressing (as shown in Fig. 79), which demonstrates that a highly likely correlation between both exists.

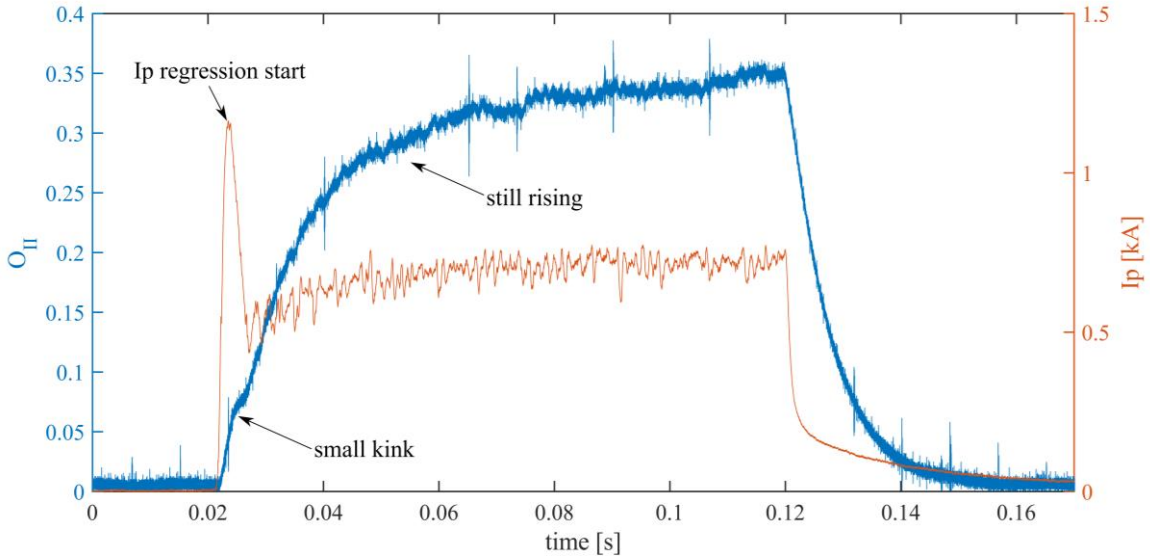

Fig. 79 Time evolution of O_{II} and Ip for the 100ms shot

Another hypothesis regarding the plasma current regression was that the poloidal magnetic field draws the plasma significantly outwards, such that the plasma hits the wall and breaks the equilibrium away. To further investigate this hypothesis, an analysis of the different camera images for different poloidal field values was conducted as shown in Fig. 80. It can be observed from Fig. 80 that the poloidal field contributes to the outwards displacement of the plasma's brightest point, however, it is nowhere near the wall so it can be concluded that the plasma does not make contact with the wall and hence regressing the plasma current.

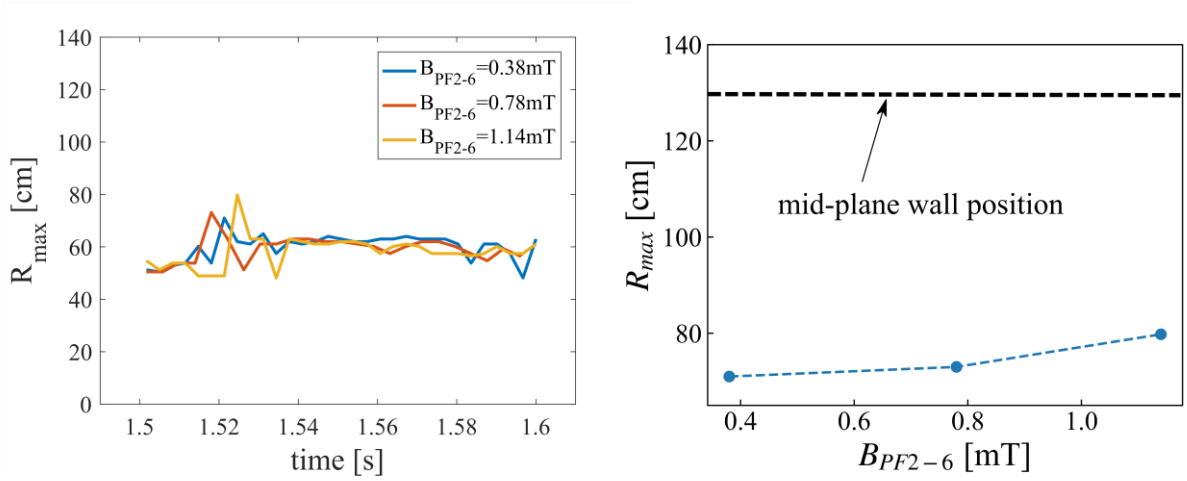

Fig. 80 The maximum brightness radial position for different poloidal fields

Upon further investigation, a prediction made by GENRAY (discussed in section 3.2) showed that the RF ray tends to bend upwards with increasing the plasma density until a point where the RF ray loses contact with the UHLR. This hypothesis requires further investigation to conclude whether ray bending occurred. One lead for investigating this hypothesis is to check the time evolution of the absorption, and compare it to the time evolution of the density. In Fig. 56, it can be noticed that the density is fluctuating, which might indicate that the RF ray loses access to the UHRL, then the density starts decreasing (along with the leakage), then the RF ray would regain access to the UHRL, and so on. To investigate this hypothesis, the convolution between both the density signal (acquired from the interferometer) and the RF leakage monitor was calculated, and the results in Fig. 82 show that 0.5ms after the plasma reaches the over-dense state, the leakage starts rising, suggesting that no RF power is delivered to the UHRL. This gives some credit to this hypothesis. It shall be noted that when calculating the convolution, the peak at the start of the RF monitor was not taken into consideration as this was before plasma breakdown.

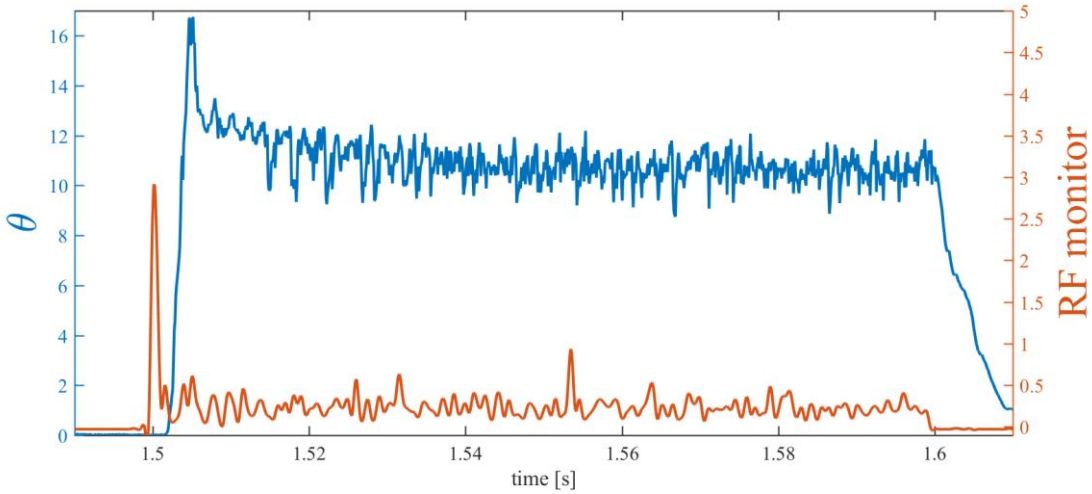

Fig. 81 Time evolution of the interferometer's line integrated phase difference compared to the RF monitor's

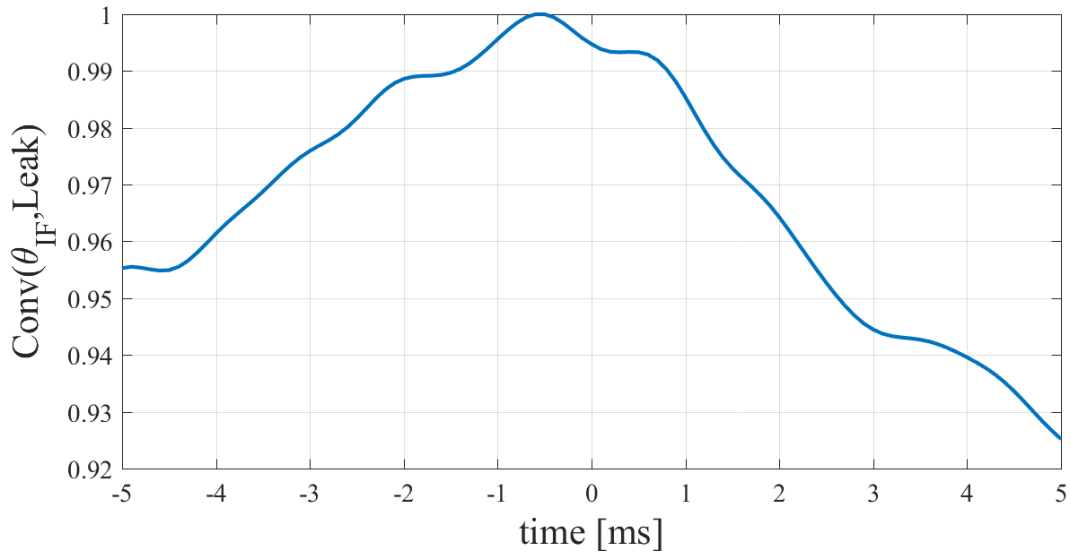

Fig. 82 The convolution between the RF leakage monitor and the phase difference of the interferometer, showing that they both are in synchrony as the maximum value of the convolution is at time 0.5ms

Nonetheless, it is worth noting that checking the camera image (see Fig. 58) for poloidal irregularities in the brightness is another indicator for this hypothesis. Expected is to have higher brightness at Z>19cm (antenna position), and that this brightness keeps moving upwards until access to the UHRL is lost (at t=1.504s), which should be where Ip starts regressing. However, the camera image (as shown in Fig. 83) barely shows any signs of a brighter local spot vertically, which indicates that there is a chance this hypothesis does not stand. The same figure for the LFS case is shown in Fig. 84, however, given the large difference in brightness, it is difficult to compare between both as the LFS case is very dim. Nevertheless, in case of amplifying the LFS brightness, such kind of oscillations are very discrete, as shown in Fig. 85. In Fig. 86, the oscillations from the interferometer phase, the Leakage monitor and the camera image are analyzed as shown by normalizing the amplitudes of them, then removing the biases. Afterwards, FFT was made to the signal to check the frequency of these oscillations. θ's oscillating frequency is at 700 Hz, Leak's oscillating frequency is at 660 Hz, and R_{max}'s oscillating frequency is at 640 Hz. It can safely be said that they are all in synchrony which gives some credit to the ray bending argument.

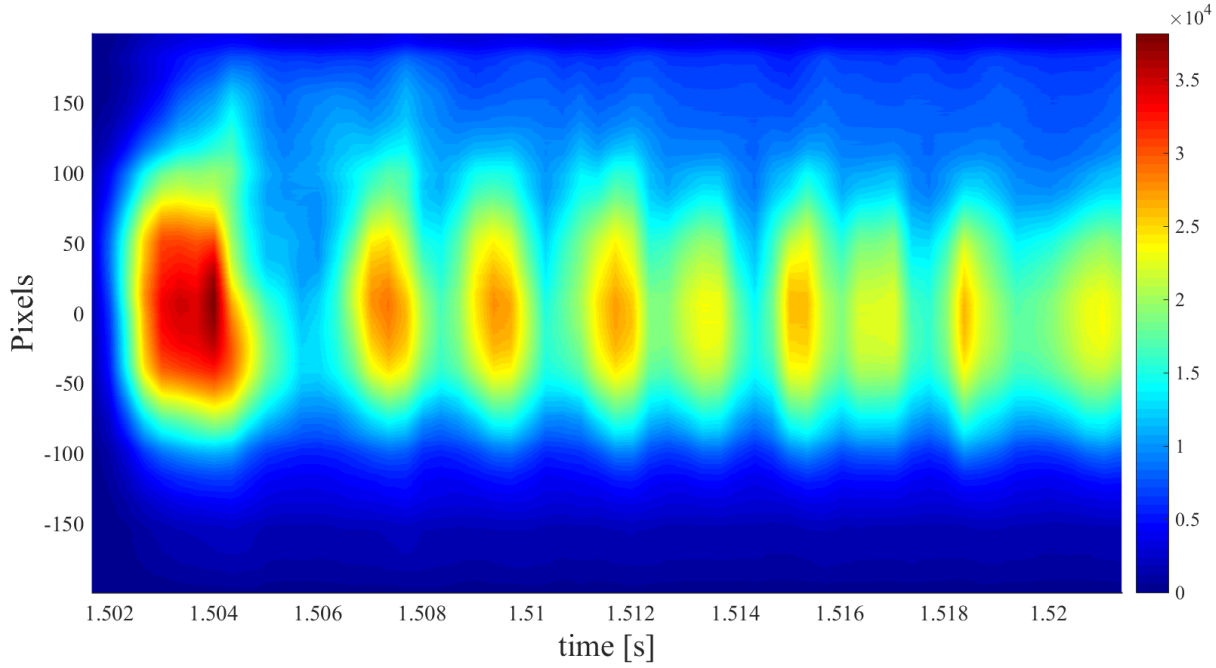

Fig. 83 Pixels vs time for HFS shot 38795. Note that pixels indicate the vertical displacement (Z-axis), however, an accurate translation from pixels to Z is not available.

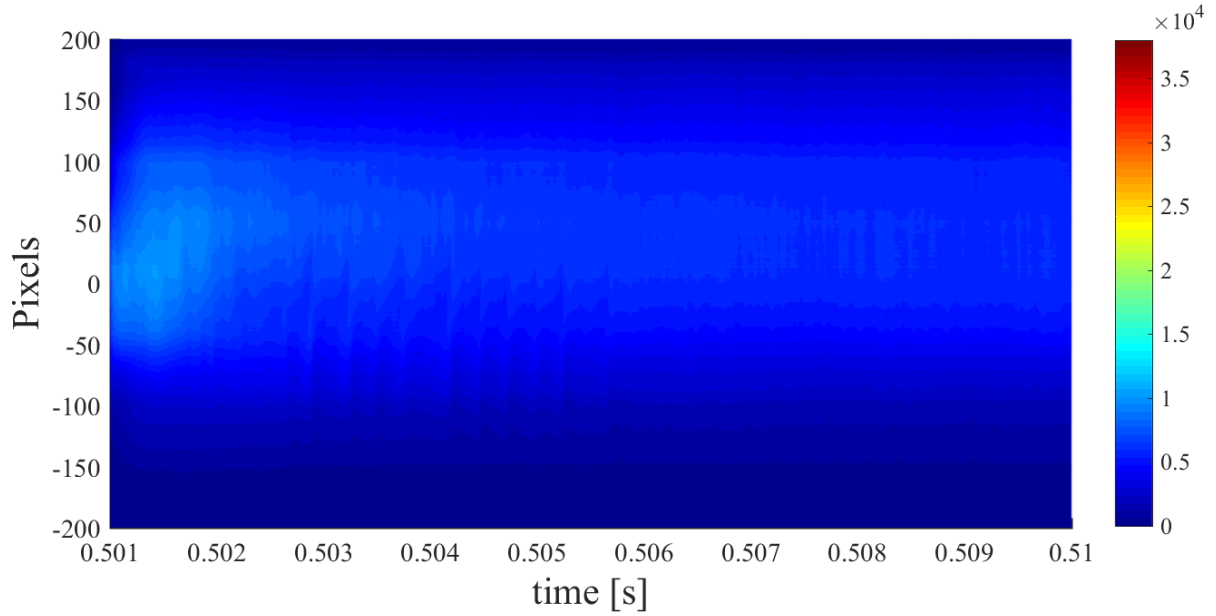

Fig. 84 Pixels vs time for LFS shot 38796. Note that pixels indicate the vertical displacement (Z-axis), however, an accurate translation from pixels to Z is not available.

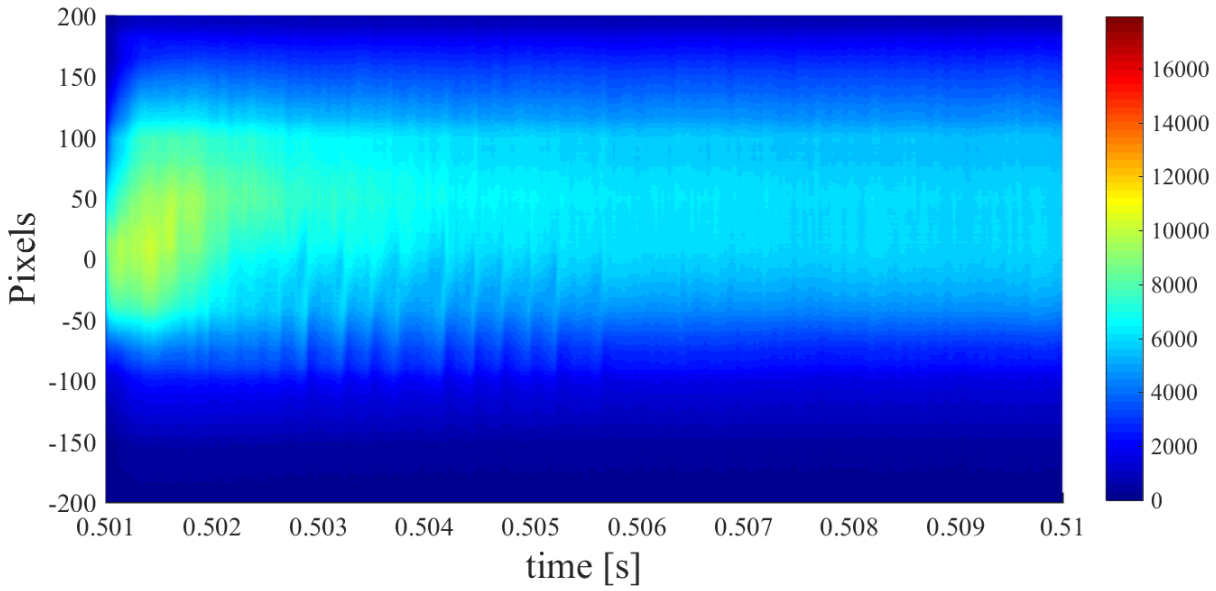

Fig. 85 Same as Fig. 84 but the brightness is amplified

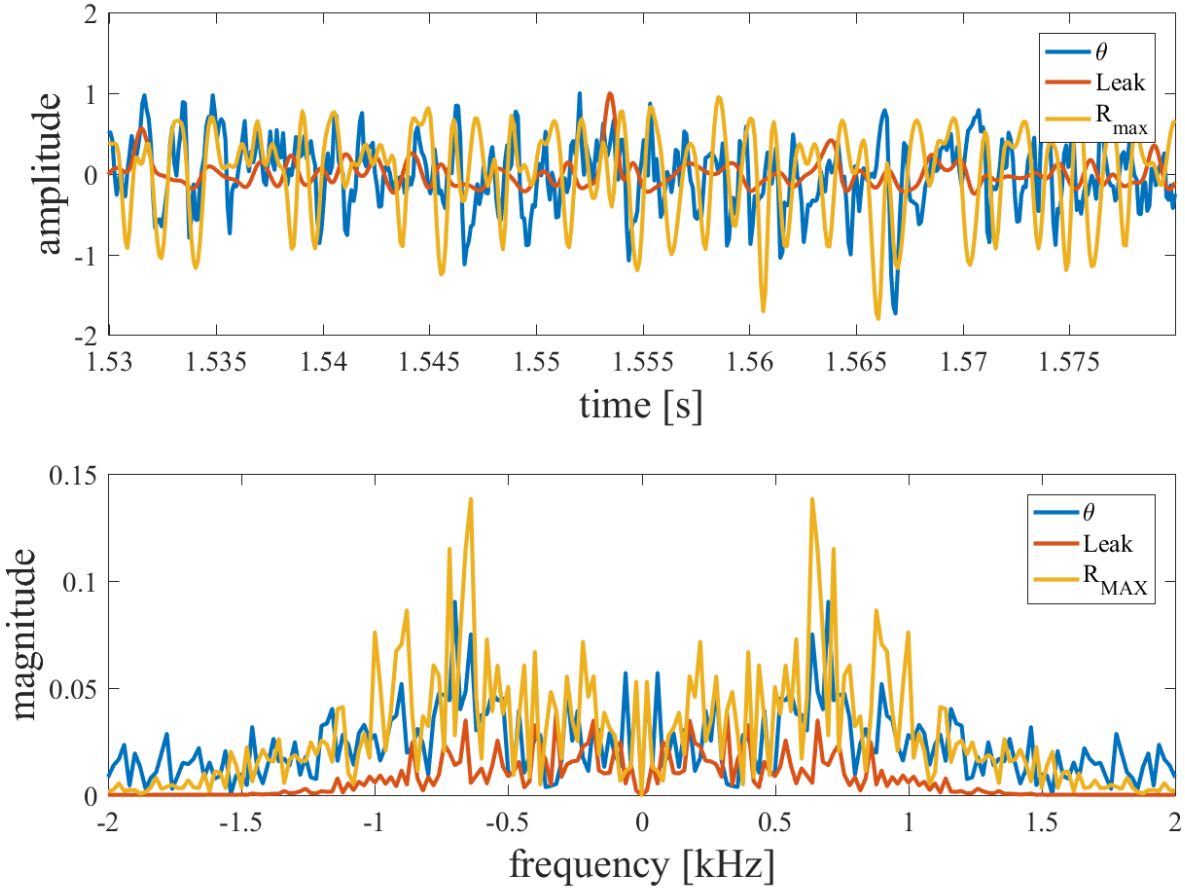

Fig. 86 (Top) waveforms of interferometer phase shift, Leak and Rmax after normalizing the amplitude and removing the bias, and (bottom) is the FFT to check whether the signals are in synchrony

6. Summary

In conclusion, using waveguides as an alternative method to mirror polarizers for HFS injection of X-mode for X-B conversion for EBW excitation is possible.

In the case of toroidal magnetic field, EBW excitation was confirmed by measuring the bent UHRL position, and comparing its corresponding density to that of the interferometer, in which case the results agreed, which confirms EBW excitation. HFS injection was demonstrated to be superior to LFS in terms of plasma current, radiation (Hα and fast camera's visible light), electron temperature and electron density, which proves that HFS injection has a higher EBW conversion efficiency than that of the LFS injection.

Next was the application of poloidal field in addition to that of the toroidal field to construct magnetic equilibrium, drive plasma current and check for EBWCD. The addition of poloidal field ramped the plasma current of both HFS and LFS cases up, however, a regression in the plasma current in the case of HFS was observed. One possible candidate for the regression of the HFS plasma current is due to the fact that the high density prevents RF ray from accessing the UHRL. An attempt to centralize the magnetic point for equilibrium construction by modifying the horizontal field failed to give any significant results, which can be attributed to the fact that the plasma current is not centralized, which indicates that forming CFS is difficult.

Nonetheless, sideband detection was successful, and it showed that a sideband of larger magnitude was achieved in HFS injection compared to LFS injection, further indicating that HFS injection has a higher conversion efficiency than that of LFS. LHW was also detected even though it was detected at a slightly lower frequency. This further confirms that EBW excitation via HFS injection was achieved, and is of higher efficiency than that of the LFS injection.

Measuring EBWCD was attempted by measuring plasma current, then reversing the polarity of the poloidal field, then re-measuring the plasma and checking for differences. The results did not show any significant differences between forward and reverse polarity of the poloidal field, and hence EBWCD excitation could not be concluded. The measured plasma current is thought to be pressure-driven as its magnitude is within the theoretical pressure-driven current.

Creating a closed flux surface inductively (using PF4) was attempted to create a plasma current jump, which would then be tested for EBWCD, but without success. This can be attributed to the fact that the magnetic decay index is comparatively low, in which case including more poloidal field coils would improve it.

Lastly, HFS plasma density was measured to be approximately twice that of the cutoff density, which was the primary target of this work.

7. Future Work

Several improvements can be done to the current HFS injection system for more accurate data acquisition as well as superior results.
Firstly, to deal with the fact that GENRAY is a code that cannot operate without closed flux surface, another ray tracing code that doesn't require the magnetic reconstruction as an input is to be used in order to simulate and analyze this experimental campaign's results.
In addition, to solve the problem of creating a closed flux surface, a change in n_{index} is required by including a combination of different poloidal field coils. It is estimated that the use of PF1-7 in combination with PF26, with inverse polarity in the case of PF1-7, will increase n_{index} as shown in Fig. 87.

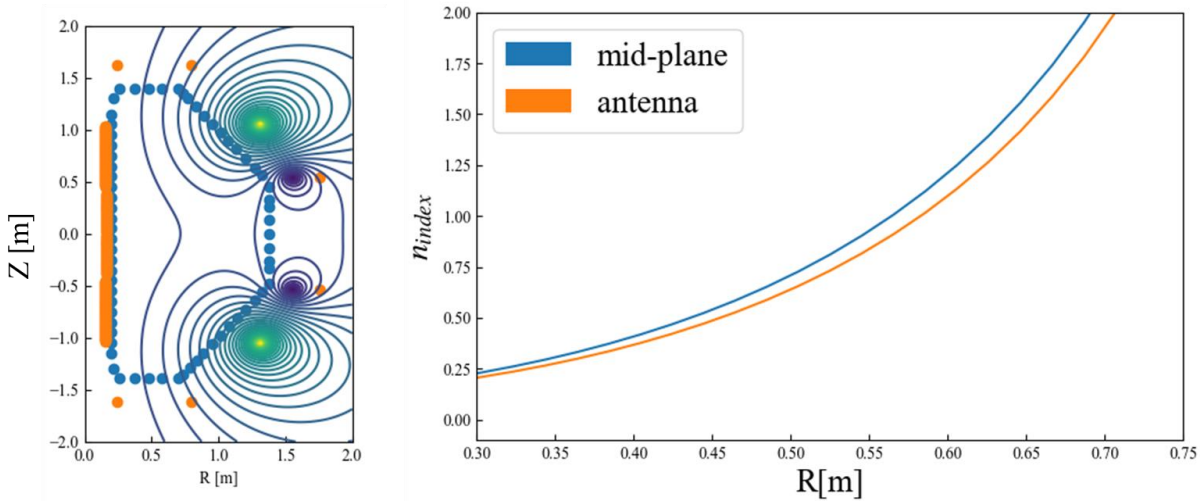

Fig. 87 (Left) Spatial distribution of flux and (right) n_{index} at B_{PF2-6}=0.78mT and B_{PF1-7}=-0.43mT

In this configuration, at the ECRL position, n_{index} at the mid-plane is 0.52 and at the antenna's vertical position is 0.47. This should give enough magnetic decay index to supply a CFS.
To further optimize, a device design can free up the HFS range close to the center stack. The injection can be done at an angle from the bottom as shown in Fig. 88.

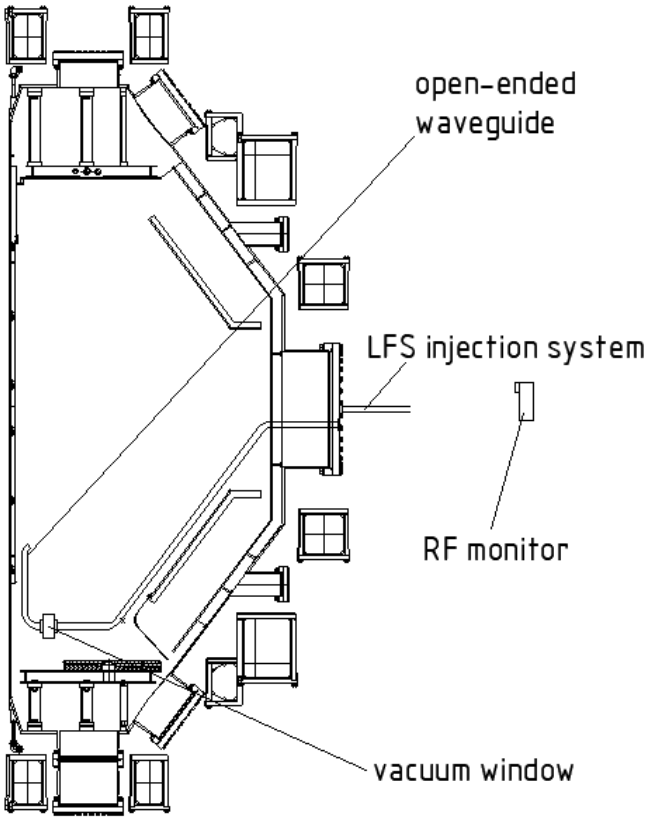

Fig. 88 Modified HFS injection system showing a tilted antenna from the bottom to free up the CS space for better magnetic reconstruction

Furthermore, all the diagnostics used for measuring the density are flawed. The Langmuir probe is placed far away from the resonance position, and the interferometer measures the line-averaged density and highly depends on the camera, so an exact value of the maximum density is not obtainable. Thomson scattering is known for its accuracy in measuring the density and temperature, however, an insertion probe is the best solution for the problem at hand. This movable probe would enable us to displace it exactly where the UHR layer is, as well as give us a radial distribution of density, that is also time-varying, so a correlation with the camera image is possible.

Last but not least, is to include water cooling to the waveguides and the vacuum windows. HFS has already proven its superiority over LFS, so with the inclusion of water cooling, HFS can be used in a steady state fashion. To further optimize this problem, if the waveguides were placed behind the diverter plate, more vessel space would be available, allowing for better confinement. The current limitation to this method is that there are a lot of other diagnostics and water cooling channel beneath the diverter plates, so the available real estate is very limited.

List of publications

Conferences

Hatem Elserafy, et al., “Fundamental concept of high field side injection of RF for EBW excitation in QUEST”, A3 Foresight Spherical Tokamak, Kunming – China, Feb. 2017

Hatem Elserafy, et al., “Preparation of high field side injection of X-mode for EBW conversion experiment in QUEST”, International Spherical Tokamak Workshop, Seoul – Korea, Sep. 2017

Hatem Elserafy, et al., “Design of direct high field side injection of X mode for EBW conversion in QUEST”, 核融合プラズマ連合講演会, Shiga – Japan, Jun. 2018

Hatem Elserafy, et al., “Direct high field side injection of X mode for EBW conversion in QUEST”, Green Asia forum, Kyushu University, Oct. 2018

Hatem Elserafy, et al., “Design of high field side injection of X-mode for EBW conversion experiment in QUEST”, International Toki Conference, Gifu – Japan, Nov. 2018

Hatem Elserafy, et al., “Design of high field side injection of X-mode for EBW conversion experiment in QUEST”, 第 35 回核融合年会, Osaka – Japan, Dec. 2018

Hatem Elserafy, et al., “Comparison between low field side and high field side injections for EBW conversion in QUEST”. 第 22 回若手科学者によるプラズマ研究会プログラム, Ibaraki – Japan, Mar. 2019

Journal articles

Hatem Elserafy, et al., “HFS Injection of X-Mode for EBW Conversion in QUEST”, Plasma and Fusion Research, Vol. 14, 1205038, Mar. 2019

Ryota Yoneda, Kazuaki Hanada, Hatem Elserafy, Nicola Bertelli, Masayuki Ono, “High-Field-Side RF Injection for Excitation of Electron Bernstein Waves”, Plasma and Fusion Research, Vol. 13, 3402115, Oct. 2018

Hatem Elserafy, “Assessment of DEMO Reactors for Fusion Power Utilization”, Evergreen Joint Journal of Novel Carbon Resource Sciences & Green Asia Strategy, Vol. 5, no. 4, pp 18 – 25, Dec. 2018

Bibliography

[1] M. Meinshausen *et al.*, "Greenhouse-gas emission targets for limiting global warming to 2°C," *Nature*, vol. 458, no. 7242, pp. 1158–1162, 2009.

[2] N. H. A. Bowerman, D. J. Frame, C. Huntingford, J. A. Lowe, and M. R. Allen, "Cumulative carbon emissions, emissions floors and short-term rates of warming: implications for policy," *Philos. Trans. R. Soc. A Math. Phys. Eng. Sci.*, vol. 369, no. 1934, pp. 45–66, 2011.

[3] H. D. Matthews, N. P. Gillett, P. A. Stott, and K. Zickfeld, "The proportionality of global warming to cumulative carbon emissions," *Nature*, vol. 459, no. 7248, pp. 829–832, 2009.

[4] UNFCCC, "Report of the Conference of the Parties on its fifteenth session, held in Copenhagen from 7 to 19 December 2009, Addendum, Part Two: Action taken by the Conference of the Parties at its fifteenth session," *Unfccc*, pp. 1–43, 2010.

[5] C. McGlade and P. Ekins, "The geographical distribution of fossil fuels unused when limiting global warming to 2°C," *Nature*, vol. 517, no. 7533, pp. 187–190, 2015.

[6] BP Global, "Statistical Review of World Energy 2018," pp. 1–53, 2018.

[7] D. Meade, "50 Years of Fusion Research," *Nucl. Fusion*, vol. 50, no. 1, 2010.

[8] Y. I. Kolesnichenko, "The role of alpha particles in tokamak reactors," *Nucl. Fusion*, vol. 20, no. 6, pp. 727–780, 1980.

[9] J. D. Lawson, "Some criteria for a power producing thermonuclear reactor," *Proc. Phys. Soc. Sect. B*, vol. 70, no. 1, pp. 6–10, 1957.

[10] J. Nucholls, L. Wood, A. Thiessen, and G. Zimmerman, "Laser Compression of Matter to Super-High Densities: Thermonuclear (CTR) Applications," *Nature*, vol. 239, pp. 37–38, 1972.

[11] S. D. Knecht, R. P. Golingo, B. A. Nelson, and U. Shumlak, "Calculation of the equilibrium evolution of the ZaP Flow Z-Pinch using a four-chord interferometer," *IEEE Trans. Plasma Sci.*, vol. 43, no. 8, pp. 2469–2479, 2015.

[12] R. Betti *et al.*, "Thermonuclear ignition in inertial confinement fusion and comparison with magnetic confinement," *Phys. Plasmas*, vol. 17, no. 5, 2010.

[13] J. D. Lindl, R. L. Mccrory, and E. M. Campbell, "Progress toward Ignition and Burn Propagation in Inertial Confinement Fusion," *Phys. Today*, vol. 45, no. 9, pp. 32–40, 1992.

[14] D. R. Wells, J. Davidson, L. G. Phadke, J. G. Hirschberg, P. E. Ziajka, and J. Tunstall, “High-Temperature, High-Density Plasma Production by Vortex-Ring Compression,” *Phys. Rev. Lett.*, vol. 41, no. 3, 1978.

[15] K. M. McGuire *et al.*, “Review of deuterium-tritium results from the Tokamak Fusion Test Reactor,” *Phys. Plasmas*, vol. 2, no. 6, pp. 2176–2188, 1995.

[16] A. A. Galeev, R. Z. Sagdeev, and G. P. Fewers, “Plasma diffusion in a toroidal stellarator,” *J. Appl. Mech. Tech. Phys.*, vol. 9, no. 6, pp. 617–625, 1972.

[17] A. Sagara, Y. Igitkhanov, and F. Najmabadi, “Review of stellarator/heliotron design issues towards MFE DEMO,” *Fusion Eng. Des.*, vol. 85, no. 7–9, pp. 1336–1341, 2010.

[18] H. A. B. Bodin and A. A. Newton, “Reversed-field-pinch research,” *Nucl. Fusion*, vol. 20, no. 10, pp. 1255–1324, 1980.

[19] T. R. Jarboe, “Review of spheromak research,” *Plasma Phys. Control. Fusion*, vol. 36, no. 6, pp. 945–990, 1994.

[20] R. S. Devoto and D. J. Bender, “Review Paper the Magnetic Mirror Approach To Fusion *,” vol. 1579.

[21] B. D. Bondarenko, “Role played by O. A. Lavrent’ev in the formulation of the problem and the initiation of research into controlled nuclear fusion in the USSR,” *Physics-Uspekhi*, vol. 44, no. 8, 2001.

[22] N. J. Peacock, D. C. Robinson, M. J. Forrest, and P. D. Wilcock, “Measurement of the Electron Temperature by Thomson Scattering in Tokamak T3,” *Nature*, vol. 224, pp. 4–6, 1969.

[23] K. Uehara, N. Fujisawa, T. Yamamoto, T. Imai, and T. Nagashima, “Particle and Heat Transport during Lower Hybrid Heating in JFT-2 Tokamak,” *J. Phys. Soc. Japan*, vol. 48, no. 4, pp. 1333–1340, 1980.

[24] D. C. Lorents, C. Brenot, and D. C. Lorents, “Finite-beta_e Universal Mode Turbulence and Alcator Scaling,” vol. 4, no. 8, 1979.

[25] G. M. McCracken, S. J. Fielding, S. K. Erents, A. Pospieszczyk, and P. E. Stott, “Re-cycling experiments in the DITE tokamak,” *Nucl. Fusion*, vol. 18, no. 1, pp. 35–45, 1978.

[26] F. Wagner *et al.*, “Regime of Improved Confinement and High Beta in Neutral-Beam-Heated Divertor Discharges of the ASDEX Tokamak,” *Phys. Fluids Phys. Fluids Rev. Lett. Appl. Phys. Lett. Phys. Fluids Phys. Fluids Phys. Rev. Lett. Phys.*

Rev. Lett. Phys. Rev. Lett, vol. 17, no. 43, pp. 1179–1068, 1974.

[27] JET team, "Fusion energy production from a deuterium-tritium plasma in the JET tokamak," *Nucl. Fusion*, vol. 32, no. 2, pp. 187–203, 1992.

[28] R. Aymar, P. Barabaschi, and Y. Shimomura, "THe ITER design," *Plasma Phys. Control. Fusion*, vol. 44, pp. 519–565, 2002.

[29] H. Idei *et al.*, "Fully non-inductive second harmonic electron cyclotron plasma ramp-up in the QUEST spherical tokamak," *Nucl. Fusion*, vol. 57, no. 12, 2017.

[30] J. A. Bittencourt, *Fundamentals of Plasma Physics*. 2004.

[31] N. H. Balshaw, "Comparison table of spherical tokamaks," *http://home.clara.net/balshaw/tokamak/table-of-spherical-tokamaks.pdf*, 2016. .

[32] K. Hanada *et al.*, "Steady-State Operation Scenario and the First Experimental Result on QUEST," *Plasma Fusion Res.*, vol. 5, pp. 1–6, 2010.

[33] M. Hasegawa *et al.*, "Development of plasma control system for divertor configuration on QUEST," *Fusion Eng. Des.*, vol. 88, no. 6–8, pp. 1074–1077, 2013.

[34] H. Zhou *et al.*, "Effects of surface conditions on the plasma-driven permeation behavior through a ferritic steel alloy observed in VEHICLE-1 and QUEST," *J. Nucl. Mater.*, vol. 463, pp. 1066–1070, 2015.

[35] S. Tashima *et al.*, "Role of energetic electrons during current ramp-up and production of high poloidal beta plasma in non-inductive current drive on QUEST," *Nucl. Fusion*, vol. 54, no. 2, p. 023010, 2014.

[36] H. Idei *et al.*, "Differential-Phase Reflectometry and Electron Bernstein Wave Radiometry using Phased-array Antenna System in the QUEST," *Plasma Fusion Res.*, vol. 9, pp. 112–117, 2010.

[37] W. Jiang, Y. Peng, Y. Zhang, and G. Lapenta, "Numerical modeling of tokamak breakdown phase driven by pure Ohmic heating under ideal conditions," *Nucl. Fusion*, vol. 56, no. 126017, pp. 1–15, 2016.

[38] S. M. Kaye and R. J. Goldston, "Global energy confinement scaling for neutralrbeam-heated tokamaks," *Nucl. Fusion*, vol. 25, no. 1, pp. 65–69, 1985.

[39] S. M. Kaye, "A review of energy confinement and local transport scaling results in neutral-beam-heated tokamaks," *Phys. Fluids*, vol. 28, no. 8, pp. 2327–2343, 1985.

[40] J. D. Strachan *et al.*, "High-temperature plasmas in a tokamak fusion test reactor," *Phys. Rev. Lett.*, vol. 58, no. 10, pp. 1004–1007, 1987.

[41] F. F.Chen, “Plasma ionization by helicon waves,” *Plasma Phys. Control. Fusion*, vol. 33, no. 4, pp. 339–364, 1991.

[42] V. Erckmann and U. Gasparino, “Electron cyclotron resonance heating and current drive in toroidal fusion plasmas,” *Plasma Phys. Control. Fusion*, vol. 36, pp. 1869–1962, 1869.

[43] Perkins.F.W, “Heating tokamaks via the ion-cyclotron and ion-ion hybrid resonances,” *Nucl. Fusion*, vol. 17, no. 6, p. 1197, 1977.

[44] Perkins.F.W, “Heating tokamaks via the ion-cyclotron and ion-ion hybrid resonances,” *Nucl. Fusion*, vol. 17, no. 6, p. 1197, 1977.

[45] V. F. Shevchenko, M. R. O’Brien, D. Taylor, and A. N. Saveliev, “Electron Bernstein wave assisted plasma current start-up in MAST,” *Nucl. Fusion*, vol. 50, no. 2, 2010.

[46] A. Ejiri *et al.*, “Non-inductive plasma current start-up by EC and RF power in the TST-2 spherical tokamak,” *Nucl. Fusion*, vol. 49, no. 6, 2009.

[47] M. Uchida, T. Yoshinaga, H. Tanaka, and T. Maekawa, “Rapid current ramp-up by cyclotron-driving electrons beyond runaway velocity,” *Phys. Rev. Lett.*, vol. 104, no. 6, pp. 2–5, 2010.

[48] S. Tashima *et al.*, “Role of energetic electrons during current ramp-up and production of high poloidal beta plasma in non-inductive current drive on QUEST,” *Nucl. Fusion*, vol. 54, no. 2, 2014.

[49] M. Ishiguro *et al.*, “Non-inductive current start-up assisted by energetic electrons in Q-shu University experiment with steady-state spherical tokamak,” *Phys. Plasmas*, vol. 19, no. 6, 2012.

[50] H. Miura *et al.*, “Comparison between non-inductive plasma current start-up using ECRH with and without fundamental resonance on QUEST,” *Plasma Fusion Res.*, vol. 10, pp. 8–11, 2015.

[51] B. Bernstein, “Waves in a plasma in a magnetic field,” *Phys. Rev.*, vol. 109, no. 1, pp. 10–21, 1958.

[52] F. W. Crawford and J. A. Tataronis, “Absolute instabilities of perpendicularly propagating cyclotron harmonic plasma Waves,” *J. Appl. Phys.*, vol. 36, no. 9, pp. 2930–2934, 1965.

[53] T. H. Stix, *Waves in Plasmas*. 1992.

[54] H. P. Laqua, “Electron Bernstein wave heating and diagnostic,” *Plasma Phys.*

Control. Fusion, vol. 49, no. 4, 2007.

[55] S. P. Kuo, "Parametric excitation of electromagnetic waves by electron Bernstein waves," *Phys. Fluids B*, vol. 4, no. 12, pp. 4094–4100, 1992.

[56] B. Thidé, H. Kopka, and P. Stubbe, "Observations of stimulated scattering of a strong high-frequency radio wave in the ionosphere," *Phys. Rev. Lett.*, vol. 49, no. 21, pp. 1561–1564, 1982.

[57] M. Porkolab and R. P. H. Chang, "Nonlinear wave effects in laboratory plasmas: A comparison between theory and experiment," *Rev. Mod. Phys.*, vol. 50, no. 4, pp. 745–795, 1978.

[58] E. Yatsuka, K. Kinjo, J. Morikawa, and Y. Ogawa, "Radio-frequency electromagnetic field measurements for direct detection of electron Bernstein waves in a torus plasma," *Rev. Sci. Instrum.*, vol. 80, no. 2, 2009.

[59] M. D. Carter, J. D. Callen, D. B. Batchelor, and R. C. Goldfinger, "Collisional effects on coherent nonlinear wave–particle interactions at cyclotron harmonics," *Phys. Fluids*, vol. 29, no. 1, p. 100, 1986.

[60] F. S. McDermott, G. Bekefi, K. E. Hackett, J. S. Levine, and M. Porkolab, "Observation of the parametric decay instability during electron cyclotron resonance heating on the Versator II tokamak," *Phys. Fluids*, vol. 25, no. 9, pp. 1488–1490, 1982.

[61] J. Seol, C. C. Hegna, and J. D. Callen, "Nonlinear cyclotron harmonic absorption," *Phys. Plasmas*, vol. 16, no. 5, 2009.

[62] Y. Nagashima *et al.*, "Observation of beat oscillation generation by coupled waves associated with parametric decay during radio frequency wave heating of a spherical tokamak plasma," *Phys. Rev. Lett.*, vol. 104, no. 24, pp. 1–4, 2010.

[63] T. Yamada *et al.*, "Direct measurement of density oscillation induced by a radio-frequency wave," *Rev. Sci. Instrum.*, vol. 78, no. 8, 2007.

[64] J. Preinhaelter and V. Kopecký, "Penetration of high-frequency waves into a weakly inhomogeneous magnetized plasma at oblique incidence and their transformation to Bernstein modes," *J. Plasma Phys.*, vol. 10, no. 1, pp. 1–12, 1973.

[65] F. R. Hansen, J. P. Lynov, and P. Michelsen, "The O-X-B mode conversion scheme for ECRH of a high-density Tokamak plasma," *Plasma Phys. Control. Fusion*, vol. 27, no. 10, pp. 1077–1100, 1985.

[66] A. Iiyoshi, M. Fujiwara, O. Motojima, N. Ohyabu, and K. Yamazaki, "Design

Study for the Large Helical Device," *Fusion Technol.*, vol. 17, no. 1, pp. 169–187, 2017.

[67] H. P. Laqua, V. Erckmann, H. J. Hartfuß, and H. Laqua, "Resonant and Nonresonant Electron Cyclotron Heating at Densities above the Plasma Cutoff by O-X-B Mode Conversion at the W7-As Stellarator," *Phys. Rev. Lett.*, vol. 78, no. 18, pp. 3467–3470, 1997.

[68] H. Renner, W. Team, N. Group, I. Group, and E. Group, "Initial operation of the Wendelstein 7AS advanced stellarator You may also be interested in :," *Plasma Phys. Control. Fusion*, vol. 31, no. 10, pp. 1579–1596, 1989.

[69] V. Shevchenko, Y. Baranov, M. O'Brien, and A. Saveliev, "Generation of Noninductive Current by Electron-Bernstein Waves on the COMPASS-D Tokamak," *Phys. Rev. Lett.*, vol. 89, no. 26, pp. 1–4, 2002.

[70] H. IGAMI *et al.*, "First Observation of ECH by Electron Bernstein Waves Excited via X-B Mode Conversion Process in LHD," *Plasma Fusion Res.*, vol. 1, pp. 052–052, 2006.

[71] M. Bornatici, R. Cano, O. De Barbieri, and F. Engelmann, "Electron cyclotron emission and absorption in fusion plasmas," *Nucl. Fusion*, vol. 23, no. 9, pp. 1153–1257, 1983.

[72] H. Igami *et al.*, "Electron Bernstein wave heating via the slow X-B mode conversion process with direct launching from the high field side in LHD," *Nucl. Fusion*, vol. 49, no. 11, 2009.

[73] R. Wilhelm *et al.*, "Electron cyclotron resonance heating and confinement in the W VII-A stellarator Robert J Goldston," *Plasma Phys. Control. Fusion*, vol. 26, no. 12A, pp. 1499–1444, 1984.

[74] T. Maekawa *et al.*, "Doppler-shifted cyclotron absorption of electron Bernstein waves via N ∥ -upshift in a tokamak plasma," *Phys. Rev. Lett.*, vol. 86, no. 17, pp. 3783–3786, 2001.

[75] L. L. Lao, H. S. John, R. D. Stambaugh, A. G. Kellman, and W. Pfeiffer, "Reconstruction of current profile parameters and plasma shapes in tokamaks," *Nucl. Fusion*, vol. 25, no. 11, pp. 1611–1622, 1985.

[76] A. P. Smirnov and R. W. Harvey, "The GENRAY ray tracing code," 2001.

[77] R. Yoneda, K. Hanada, H. Elserafy, N. Bertelli, and M. Ono, "High-Field-Side RF Injection for Excitation of Electron Bernstein Waves ∗)," vol. 13, pp. 1–4, 2018.

[78] V. F. Shevchenko *et al.*, “Long Pulse EBW Start-up Experiments in MAST,” in *EPJ Web of Conferences*, 2015, vol. 87, pp. 3–8.

[79] K. Kuroda *et al.*, “Current Start-Up Using the New CHI System,” *Plasma Fusion Res.*, vol. 12, pp. 3–5, 2017.

[80] H. M. Mott-Smith and I. Langmuir, “The theory of collectors in gaseous discharges,” *Phys. Rev.*, vol. 28, no. 4, pp. 727–763, 1926.

[81] K. Uchijima, T. Takemoto, J. Morikawa, and Y. Ogawa, “Direct observation of transition to electron Bernstein waves from electromagnetic mode by three mode-conversion scenarios in the dipole confinement torus plasma,” *Plasma Phys. Control. Fusion*, vol. 57, no. 6, 2015.

[82] H. P. Laqua, “Electron Bernstein wave heating and emission via the OXB process at W7-AS,” *Plasma Phys. Control. Fusion*, vol. 41, no. 3A, 1999.

[83] M. Uchida *et al.*, “Generation of initial closed flux surfaces by ECH at a conventional aspect ratio of R/a ~ 3: Experiments on the LATE device and JT-60U tokamak,” *Nucl. Fusion*, vol. 51, no. 6, 2011.

[84] M. A. HERLIN and S. C. BR0WN, “Breakdown of a Gas at Microwave Frequencies,” *Phys. Rev.*, vol. 74, no. 3, 1948.

[85] P. M. Platzman and E. H. Solt, “Microwave breakdown of air in nonuniform electric fields,” *Phys. Rev.*, vol. 119, no. 4, pp. 1143–1149, 1960.

[86] A. D. MacDonald, *Microwave breakdown in gases*. 1966.

[87] G. E. Georghiou, A. P. Papadakis, R. Morrow, and A. C. Metaxas, “Numerical modelling of atmospheric pressure gas discharges leading to plasma production,” *J. Phys. D. Appl. Phys.*, vol. 38, no. 20, 2005.

[88] H. K. Malik and A. K. Aria, “Microwave breakdown for the TE10 mode in a rectangular waveguide,” *Phys. Plasmas*, vol. 20, no. 20, 2013.

[89] H. K. Malik and A. K. Aria, “Microwave and plasma interaction in a rectangular waveguide: Effect of ponderomotive force,” *J. Appl. Phys.*, vol. 108, no. 1, 2010.

[90] S. Kumar and M. Yoon, “Electron acceleration in a warm magnetized plasma-filled cylindrical waveguide,” *J. Appl. Phys.*, vol. 104, no. 7, 2008.

[91] S. K. Tomar and H. K. Malik, “Density modification by two superposing TE10modes in a plasma filled rectangular waveguide,” *Phys. Plasmas*, vol. 20, no. 7, 2013.

[92] K. Frigui *et al.*, “Microwave breakdown in waveguide filters theoretical and

experimental investigations," in *IEEE Transactions on Microwave Theory and Techniques*, 2008, vol. 56, no. 12, pp. 3072–3078.

[93] K. Frigui *et al.*, "Microwave breakdown in waveguide filters, numerical simulation, and comparison to experiments," *J. Appl. Phys.*, vol. 107, no. 4, 2010.

Appendix

1. RF heating in plasmas

An analysis of electromagnetic wave propagation inside the plasma is required before analyzing the effects of RF heating.
Starting from Maxwell's well-known equations:

$$\nabla \times E + \frac{1}{c}\frac{\partial \boldsymbol{B}}{\partial t} = 0 \tag{1.1}$$

$$\nabla \times B - \frac{1}{c}\frac{\partial \boldsymbol{E}}{\partial t} = \frac{4\pi}{c}(J + J_{ext}) \tag{1.2}$$

$$\nabla . \boldsymbol{E} = 4\pi(\rho + \rho_{ext}) \tag{1.3}$$

$$\nabla . \boldsymbol{B} = 0 \tag{1.4}$$

where ρ is induced space-charge with $\boldsymbol{J}$ through the continuity equation:

$$\frac{\partial \rho}{\partial t} + \nabla . J = 0 \tag{1.5}$$

J_{ext} and ρ_{ext} are external source current and charge densities. Defining the complex Fourier amplitude as:

$$E(k,\omega) = \int_v dr \int_{-\infty}^{+\infty} dt E(r,t) e^{-i(k.r-\omega t)} \tag{1.6}$$

and same goes with $J(k,\omega)$ and $B(k,\omega)$ which are calculated from $J(r,t)$ and $B(r,t)$ such that:

$$J(r,t) = \int_v dr' \int_{-\infty}^{t} dt' \sigma(r,r';t,t') . E(r,t) \tag{1.7}$$

$$J(k,\omega) = \sigma(k,\omega) . E(k,\omega) \tag{1.8}$$

where the tensor $\sigma(k,\omega)$ is the medium conductivity tensor. Maxwell's equations can thus be re-written as

$$k \times \boldsymbol{E} - \frac{\omega}{c}\boldsymbol{B} = 0 \tag{1.9}$$

$$k \times \boldsymbol{B} - \frac{\omega}{c}\boldsymbol{E} = -\frac{4\pi i}{c}(\boldsymbol{J} + \boldsymbol{J}_{ext}) \tag{1.10}$$

$$k.\boldsymbol{E} = -4\pi i(\rho + \rho_{ext}) \tag{1.11}$$

$$k.\boldsymbol{B} = 0 \tag{1.12}$$

The medium dielectric tensor is defined as:

$$\epsilon(k,\omega) = \boldsymbol{I} - \frac{4\pi}{i\omega}\sigma(k,\omega) \tag{1.13}$$

where $\boldsymbol{I}$ is the 3×3 unit tensor. A convenient form to write the wave equation would then be

$$k \times (k \times k) + \frac{\omega^2}{c^2}\epsilon.\boldsymbol{E} = 0 \tag{1.14}$$

A dimensionless vector $\boldsymbol{n}$ which has a direction of propagation along $\boldsymbol{k}$ and has magnitude of the refractive index

$$\boldsymbol{n} = \frac{\boldsymbol{k}c}{\omega} \tag{1.15}$$

such that the magnitude of $\boldsymbol{n}$ is the ratio of light velocity c to the wave phase velocity. Re-writing the wave equation in terms of $\boldsymbol{n}$ would give

$$\boldsymbol{n} \times (\boldsymbol{n} \times \boldsymbol{E}) + \epsilon.\boldsymbol{E} = 0 \tag{1.16}$$

which in matrix form would give

$$\begin{pmatrix} \varepsilon_{xx} - \left({n_y}^2 + {n_z}^2\right) & \varepsilon_{xy} + n_x n_y & \varepsilon_{xz} + n_x n_z \\ \varepsilon_{yx} + n_x n_y & \varepsilon_{yy} - ({n_x}^2 + {n_z}^2) & \varepsilon_{yz} + n_y n_{yz} \\ \varepsilon_{zx} + n_x n_z & \varepsilon_{zy} + n_y n_z & \varepsilon_{zz} - \left({n_x}^2 + {n_y}^2\right) \end{pmatrix} \begin{pmatrix} E_x \\ E_y \\ E_z \end{pmatrix} = 0 \qquad 1.17$$

Defining the transverse projection tensor $\boldsymbol{I}_T$ such that

$$\boldsymbol{I}_T = \boldsymbol{I} - \frac{\boldsymbol{kk}}{k^2} \qquad 1.18$$

the wave equation would simply be

$$(\epsilon - n^2 \boldsymbol{I}_T).\boldsymbol{E} = 0 \qquad 1.19$$

Defining a new tensor $\Delta(\boldsymbol{k}, \omega)$ such that

$$\Delta(\boldsymbol{k}, \omega) \equiv \epsilon - n^2 \boldsymbol{I}_T \qquad 1.20$$

would give

$$\Delta.\boldsymbol{E} = 0 \qquad 1.21$$

This final equation possesses nontrivial solution only if the determinant constructed from the elements of the tensor $\Delta(\boldsymbol{k}, \omega)$ vanishes:

$$D(\boldsymbol{k}, \omega) \equiv det|\Delta(\boldsymbol{k}, \omega)| = 0 \qquad 1.22$$

is equation is called the dispersion relation and the function D is called the dispersion function. The dispersion relation is particularly important in describing the state at which an EMW is propagating. Different states are widely known as modes of propagation and each mode is given certain properties.

Cold plasma approximation is assumed for simplicity, where the thermal electron motion is

neglected. The dielectric tensor ϵ is written as

$$\epsilon = \begin{pmatrix} S & -iD & 0 \\ iD & S & 0 \\ 0 & 0 & P \end{pmatrix} \qquad 1.23$$

In which the quantities S (sum), D (difference) and P (plasma, also known as Stix coefficient) are defined as:

$$S = \frac{1}{2}(R + L) \tag{1.24}$$

$$D = \frac{1}{2}(R - L) \tag{1.25}$$

$$R \equiv 1 - \sum_s \frac{{\omega_{ps}}^2}{\omega(\omega + \Omega_s)} \tag{1.26}$$

$$L \equiv 1 - \sum_s \frac{{\omega_{ps}}^2}{\omega(\omega - \Omega_s)} \tag{1.27}$$

$$P \equiv 1 - \sum_s \frac{{\omega_{ps}}^2}{\omega^2} \tag{1.28}$$

In this context, R denotes right-hand circular polarization and L denotes left-hand circular polarization.
Assuming that wave propagation is along the magnetic field lines ($n_x = 0, n_y = 0$), the electric field equation simplifies to

$$\begin{pmatrix} S - n^2 & -iD & 0 \\ iD & S - n^2 & 0 \\ 0 & 0 & P \end{pmatrix} \begin{pmatrix} E_x \\ E_y \\ E_z \end{pmatrix} = 0 \tag{1.29}$$

whereas the dispersion relation is divided into

$$n^2 = S - D = L \tag{1.30}$$

$$n^2 = S + D = R \tag{1.31}$$

$$P = 0 \tag{1.32}$$

corresponding to two electromagnetic solutions (left and right circularly polarized) and one electrostatic solution (plasma oscillations with $\omega = \omega_p$). Fig. 89 shows the left and right circularly polarized wave vector diagram.

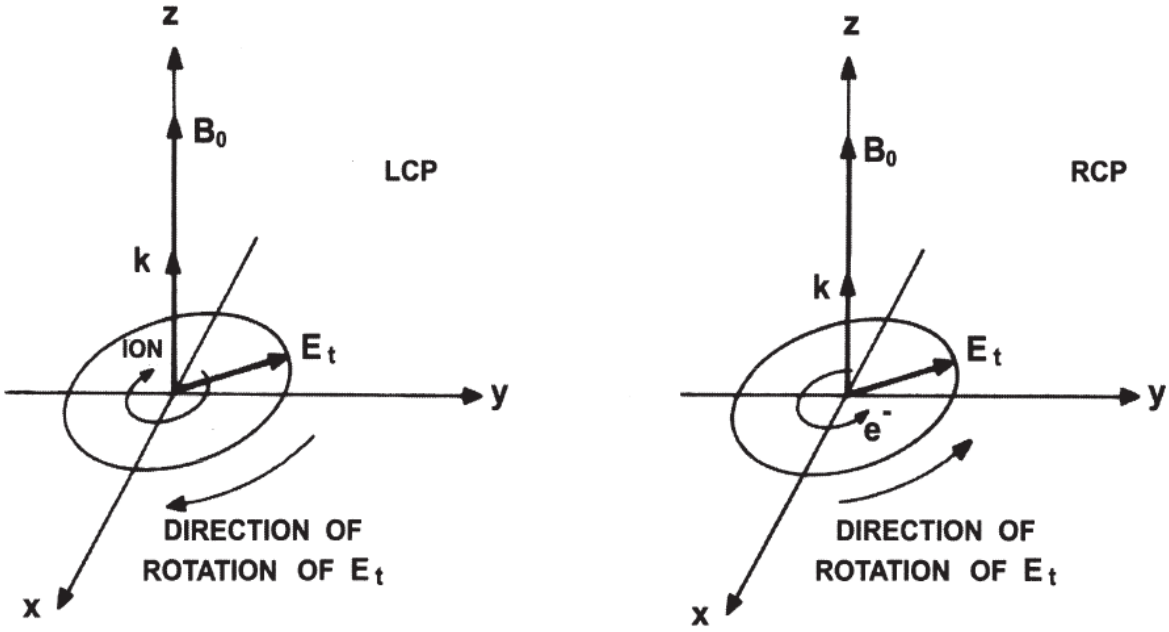

Fig. 89 For propagation along the magnetic field, Left Circularly Polarized (LCP) wave rotates in the counterclockwise direction, while the Right Circularly Polarized (RCP) wave rotates in the clockwise direction, for an observer looking at the outgoing wave. B_0 is the magnetostatic field. E_t is defined as the transverse electric field. This figure is (from ref. [30]*)*

Assuming now that wave propagation is perpendicular to magnetic field lines ($n_z = 0, n_y = 0$),

there is no electrostatic solution, but only two electromagnetic eigenmodes of refractive index:

$$n^2 = P \qquad 1.33$$

$$n^2 = \frac{RL}{S} \qquad 1.34$$

such that the former represents what is known as the ordinary O mode, and the latter represents the extraordinary X mode. It is best to represent the dispersion relation graphically as follows:

From both graphical and mathematical expressions, it can be seen that for O mode, a cutoff frequency exists at $\omega = \omega_p$, and for X mode, two cutoff frequencies exists at $\omega_{R,L} = \left(\sqrt{\frac{{\omega_c}^2}{4} + {\omega_p}^2}\right) \pm \frac{\omega_c}{2}$ such that the phase velocity decides whether fast (FX) or slow (SX) X modes are propagating.

2. Benchtesting of ECRL breakdown inside waveguides

Microwave breakdown has been studied extensively ever since the late 30s [84]–[87] and in waveguides [88]–[93].
An arbitrarily small number of free electrons exist in any gas, which flows in the direction of an electric field if present. At the right electric field conditions, collision-based secondary electron emission will prevail. If the secondary electron emission kept growing, the gas will eventually become conducting, also known as breaking down. Primarily, free electron collisions occur due to neutral particle interaction and waveguide wall surface interaction. An inert gas exists unconditionally inside of the waveguide, which in the presence of an electric field and a small number of charged particles existing as ionization due to natural phenomena such as photoelectric effect takes place, breakdown can occur given the appropriate conditions. In theory, the induced electric field drives the charged particles to collide with the neutral particles, ionizing the neutral particles and thereby creating an avalanche effect that causes the density of charged particles to increase. This, in turn, causes the gas to glow creating an electromagnetic wave reflection layer that can potentially destroy the source. The charged particle density (electron density) n can be expressed using the continuity equation

$$\frac{\delta n}{\delta t} = (\nu_i - \nu_l)n \tag{2.1}$$

where ν_i is the ionization frequency and ν_l is the loss frequency. The ionization frequency is defined as

$$\nu_i = \alpha \mu E_e \tag{2.2}$$

where α is Townsend's ionization coefficient and μ_x is the electron mobility in the presence of the effective electric field E_e such that

$$\mu_x = \frac{e}{(m\nu_c)} \tag{2.3}$$

and ν_c is the collision frequency.
The effective electric field is expressed as

$${E_e}^2 = \frac{{E_{rms}}^2}{\left(1 + \frac{\omega^2}{{\nu_c}^2}\right)} \tag{2.4}$$

In the range of $\omega < \nu_c$, it can be assumed that $E_e \cong E_{rms}$
[22]. The loss frequency is defined as

$$\nu_l = \nu_d + \nu_a + \nu_r \tag{2.5}$$

where ν_d, ν_a and ν_r are the diffusion, attachment and recombination frequencies respectively.

The diffusion frequency is defined as

$$\nu_d = \frac{D}{\Lambda^2} \tag{2.6}$$

where D is the diffusion coefficient and Λ is the characteristic diffusion length. The attachment frequency is defined as

$$\nu_a = \beta_x \mu E_e \tag{2.7}$$

where β_x is the attachment coefficient. Rearranging $\frac{\delta n}{\delta t} = (\nu_i - \nu_l)n$ gives

$$n = n_0 exp(\nu_i - \nu_l)t \tag{2.8}$$

noting that a small shift in $\nu_i - \nu_l$ will cause n to rise exponentially, as the Townsend criterion dictates. Investigation of microwave breakdown inside of a waveguide that is subject to magnetic field is necessary as the only way for LFS to HFS transmission of RF power via waveguide is for the waveguides to traverse the ECRL. In order to investigate the first issue of X-mode RF wave capability of penetrating the ECRL without breakdown, an external experiment was conducted as shown in Fig. 90 emulating QUEST's ECRL and applying it to RG-50 waveguides connected to the klystron K1. The experimental setup is comprised of the wave generation using the fucntion generator, amplifier and klystron, wave propagation inside of a SF_6-filled waveguide, and the application of an external static magnetic field to emulate ECR layer inside of QUEST, being likely to induce breakdown. The function generator outputting +5 dBm at a frequency of 8.2 GHz is then connected to a microwave amplifier with a theoretical gain of 30 dB and then the output signal of the amplifier is then directed towards the klystron. In order for the klystron to operate at optimum performance, the beam voltage of the static magnetic field is set to 21 kV and the beam current 3.38 A. These values, as set by the klystron manufacturer, are dedicated for the klystron's theoretical output of 25 kW. The klystron power output is to be increased ascendingly. In our setup, the maximum external magnetic field density is set to 0.3 T as the designed QUEST ECRL is of 0.25 T. SF_6 gas pressure inside the waveguide was 0.03 MPa. In order to measure the received power from the klystron powered wave propagation in SF_6-filled waveguide, water load was used with thermistors to measure the temperature change in water. Water flow was set at 14.8 lit/min. The waterload is shown in Fig. 91 and the final design is shown in Fig. 92.
Fig. 93 shows the temperature rise of the waterload due to 20kW of injected RF power for various pulse shot durations.
To calculate the RF power that transmitted to the water load, first the energy is calculated as

$$W[J] = \int Q.\rho.C.\Delta T(t)\ dt \tag{2.9}$$

where W is the energy measured in $Joules$, Q is the volumetric flow rate (measured from the flow meter at 14.8 lit/min), ρ is the density of water (1000 kg/m^3), C is the specific heat capacity of water (4184 J/kg/K) and ΔT is the temperature difference between water entering the water load (T1(t)) and water exiting the water load (T2(t)). The ΔT time evolution for different RF pulse durations is shown in Fig. 93. The received power can therefore be calculated as

$$P_{WL}[W] = \frac{W}{T_{pulse}} \tag{2.10}$$

where P_{WL} is the power received by the water load.
The fitted slope to calculate the power is shown in Fig. 94. The results showed that up to 11 kW can penetrate the waveguide without breakdown. Further increase in power was not conducted for safety reasons.

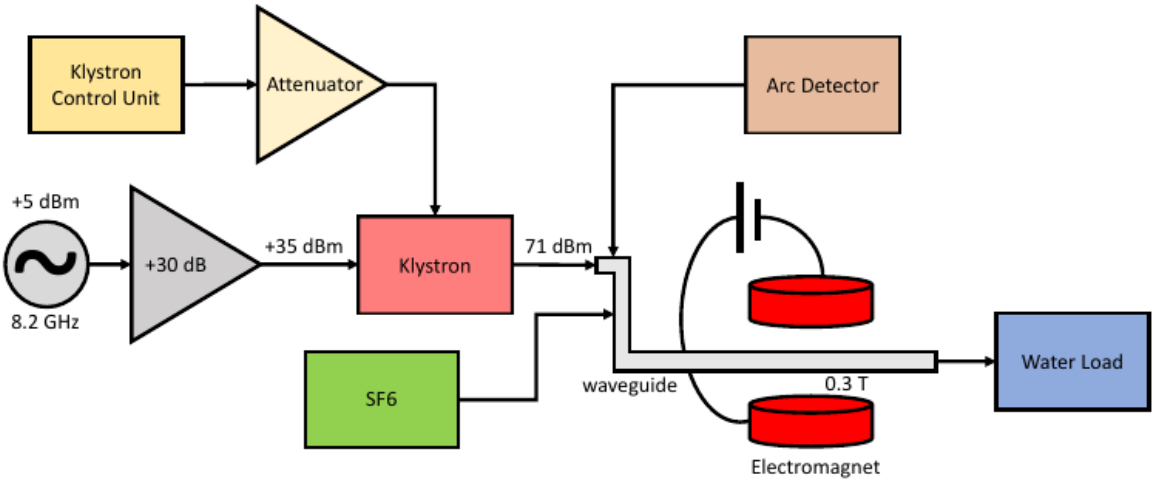

Fig. 90 Schematic for ECRL penetration bench test

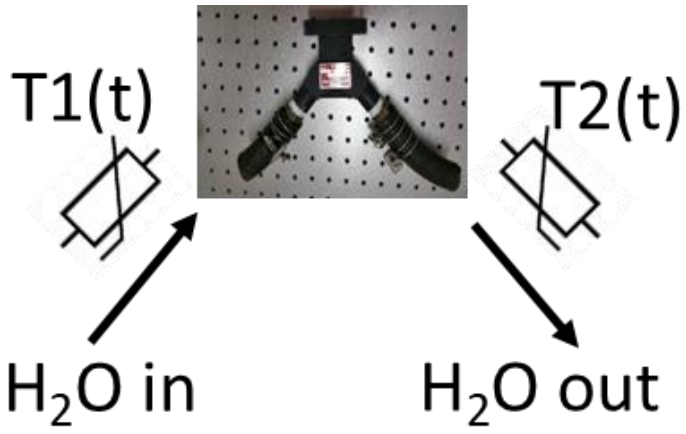

Fig. 91 The water load used to terminate the waveguide while showing the positions of the temperature sensors T1 and T2

Fig. 92 The final design of the water load, waveguide and the electromagnet

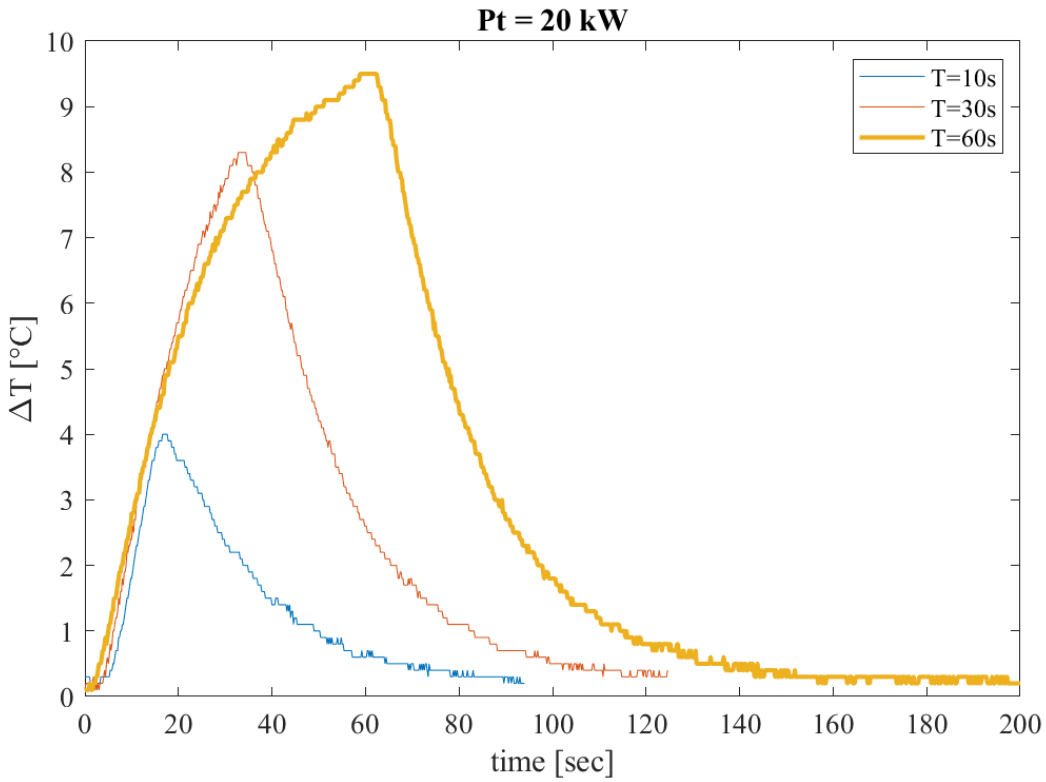

Fig. 93 Temperature difference as a function in time for pulse durations of T=10s, T=30s, and T=60s for a water load terminating a waveguide with input RF power of 20kW that is subject to a magnetic field of 0.3T

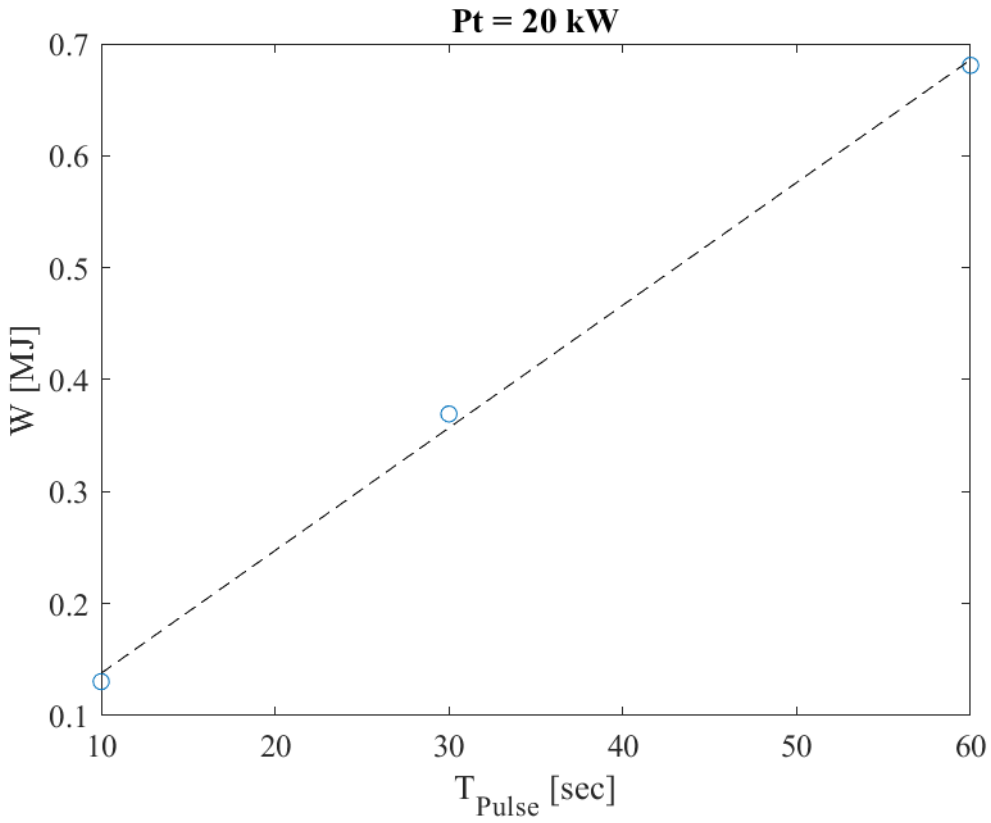

Fig. 94 Energy as a function in pulse duration (blue) with dotted-black line as best fit line for measuring slope and detecting the power